Study of the replacement correction factors for ionization chamber dosimetry by Monte Carlo simulations

by

Lilie Wang

A thesis submitted to the
Faculty of Graduate Studies and Research
in partial fulfillment of the requirements
for the degree of

Doctor of Philosophy

Department of Physics
Carleton University
Ottawa-Carleton Institute of Physics
Ottawa, Canada

April 20, 2009

Dedicated to my daughters,

Janet, who is learning the **replacement** of numbers by alphabetic symbols, and

Katie, who is continuously making **correction**s in imitating speech,

and my wife,

Mingming, who is the greatest supportive **factor** in my family,

during the whole period of my program of study.

I owe them a vacation trip to **Monte Carlo** city!

Abstract

In ionization chamber radiation dosimetry, the introduction of the ion chamber into medium will unavoidably distort the radiation field near the chamber because the chamber cavity material (air) is different from the medium. A replacement correction factor, P_{repl}, was introduced in order to correct the chamber readings to give an accurate radiation dose in the medium without the presence of the chamber. Generally it is very hard to measure the values of P_{repl} since they are intertwined with the chamber wall effect. In addition, the P_{repl} values always come together with the stopping-power ratio of the two media involved. This makes the problem of determining the P_{repl} values even more complicated. Monte Carlo simulation is an ideal method to investigate the replacement correction factors. In this study, four different methods of calculating the values of P_{repl} by Monte Carlo simulation are discussed. Two of the methods are designated as 'direct' methods in the sense that the evaluation of the stopping-power ratio is not necessary. The systematic uncertainties of the two direct methods are estimated to be about 0.1-0.2% which comes from the ambiguous definition of the energy cutoff Δ used in the Spencer-Attix cavity theory. The two direct methods are used to calculate the values of P_{repl} for both plane-parallel chambers and cylindrical thimble chambers in either electron beams or photon beams. The calculation results are compared to measurements. For electron beams, good agreements are obtained. For thimble chambers in photon beams, significant discrepancies are observed between calculations and measurements. The experiments are thus investigated and the procedures are simulated by the Monte Carlo method. It is found that the interpretation of the measured data as the replacement correction factors in dosimetry protocols are not correct. In applying the calculation to the BIPM graphite chamber in a ^{60}Co beam, the calculated values of P_{repl} differ from those used for the chamber by about 1% which leads to 1% change in the W/e value obtained by using this chamber.

Acknowledgements

I wish to express my sincere appreciation to my supervisor, Dr David Rogers, who offered valuable assistance and guidance in this study, and without whose support this research project would not have been possible. I am also indebted to the members of the advisory committee, Dr Paul Johns, who read the thesis with great care and made detailed comments to help make the thesis better, and Dr Kuiying Chen, who made helpful suggestions during the course of the research project.

I would also like to express my gratitude to Dr Karl-Axel Johansson for information on determining the displacement factors, to Dr Pedro Andreo for information and a routine on the calculation of the displacement factors in the IAEA's TRS-398, and to Dr Alan Nahum for insightful, helpful comments on the P_{repl} paper.

I am grateful to Rowan Thomson for drawing my attention to the revision of W/e factor measured with the BIPM chamber and for making helpful comments to most of my manuscripts; and I am also thankful to Dan LaRussa for providing me an input file for the NE2571 chamber model. All members of the Carleton Laboratory for Radiotherapy Physics are appreciated for taking time to read and comment on my manuscripts. All faculty members and staff of the Department of Physics are appreciated for their kindness and help during my program of study.

Being a recipient of the Gary S Duck Graduate Scholarship, the generous support of Mr and Mrs Duck is highly appreciated. I am also partly funded by an Ontario Graduate Scholarship. The computing for this research project was partially done using the WestGrid computing resource.

Finally, I wish to thank my wife, Mingming, and my daughters, Janet and Katie, for their continuous support and understanding during the whole study period.

Statement of Originality

(I) Monte Carlo Study of Si Diode Response in Electron Beams

L. L. W. Wang and D. W. O. Rogers, Medical Physics (34), 1734-1742, (2007)

- Parts of this paper are used in Appendix B.
- The author performed all of the calculations for this paper and drafted and performed edits on the manuscript. A talk detailing some of the results was presented at the 2006 AAPM annual meeting in Orlando, USA.

(II) Calculation of the replacement correction factors for ion chambers in megavoltage beams by Monte Carlo simulation

L. L. W. Wang and D. W. O. Rogers, Medical Physics (35), 1747-1755, (2008)

- Parts of this paper are used in Chapter 2, Chapter 3 and Chapter 4.
- The author performed all of the calculations for this paper and drafted and performed edits on the manuscript. Some of the results were presented as a poster at the 2007 COMP annual meeting in Toronto, and some were orally presented at the 54th COMP meeting in Quebec City in June 2008.

(III) The replacement correction factor for the BIPM flat cavity ion chamber and the value of W/e

L. L. W. Wang and D. W. O. Rogers, Medical Physics (35), 4410-4416, (2008)

- Parts of this paper are used in Chapter 3.
- The author performed all of the calculations for this paper and drafted and performed edits on the manuscript.

(IV) The replacement correction factors for cylindrical chambers in high-energy photon beams

L. L. W. Wang and D. W. O. Rogers, Physics in Medicine and Biology (54), 1609-1620, (2009)

- Parts of this paper are used in Chapter 4.
- The author performed all of the calculations for this paper and drafted and performed edits on the manuscript. Some of the results were orally presented at the 54th COMP meeting in Quebec City in June 2008.

(V) Systematic uncertainties in the Monte Carlo calculation of ion chamber replacement correction factors

L. L. W. Wang, D J La Russa and D. W. O. Rogers, Medical Physics (36), (in press), (2009)

- Parts of this paper are used in Chapter 2.
- The author performed all of the calculations for this paper and drafted and performed edits on the manuscript.

(VI) Study of the effective point of measurement for ion chambers in electron beams by Monte Carlo simulation

L. L. W. Wang and D. W. O. Rogers, Medical Physics (36), (in press), (2009)

- Parts of this paper are used in Appendix A.
- The author performed all of the calculations for this paper and drafted and performed edits on the manuscript.

(VII) The replacement correction factors for cylindrical ion chambers in electron beams

L. L. W. Wang and D. W. O. Rogers, Medical Physics (36), (accepted), (2009)

- Parts of this paper are used in Chapter 4.
- The author performed all of the calculations for this paper and drafted and performed edits on the manuscript. Some of the results were orally presented at the 54th COMP meeting in Quebec City in June 2008.

Contents

List of Tables

List of Figures

Chapter 1

Introduction

The goal of radiation therapy is to deliver radiation dose to the malicious target as prescribed while minimizing the dose to the normal structures. The International Commission on Radiation Units and Measurements (ICRU) recommended an overall accuracy of 5% in delivering radiation dose to the target.[1] While practically many factors influence accurate dose delivery, the most important issue resides in the calibration of the radiation sources used for radiation therapy, i.e. knowing exactly how much radiation dose is delivered to the point of interest. This is the objective of radiation dosimetry. The ionization chamber is the most commonly used dosimeter for ionizing radiation because of its high precision, its real-time readout, and relatively good sensitivity. The theoretical basis of the ionization chamber radiation dosimetry is cavity theory.

1.1 Cavity theory

Generally, the radiation dose, D, delivered by charged particles in a medium is related to the particle fluence spectrum, $\Phi(E)$, and the mass collision stopping power of the

particle in the medium, $\left(\frac{S}{\rho}\right)$, by

$$D = \int \Phi(E) \left(\frac{S(E)}{\rho}\right) dE, \tag{1.1}$$

Suppose there is a cavity of material *cav* located in a phantom of material *med*. The radiation dose in the cavity, D_{cav}, is related to that at the same point in the phantom without the presence of the cavity, D_{med}, by the Bragg-Gray relation[2,3]

$$\frac{D_{med}}{D_{cav}} = \frac{\int \Phi_{med}(E) \left(\frac{S(E)}{\rho}\right)_{med} dE}{\int \Phi_{med}(E) \left(\frac{S(E)}{\rho}\right)_{cav} dE} \equiv \left(\frac{\overline{S}}{\rho}\right)_{cav}^{med}, \tag{1.2}$$

where $\left(\frac{\overline{S}}{\rho}\right)_{cav}^{med}$ is the mean mass collision stopping-power ratio of the two materials and $\Phi_{med}(E)$ is the fluence spectrum of primary charged particles. The conditions for applying the Bragg-Gray relation are: (1) the electron fluence spectrum is not perturbed by the cavity; (2) energy deposited in the cavity is solely from the electrons crossing the cavity. This relationship also requires charged particle equilibrium (CPE) of all secondary electrons. The drawback of the Bragg-Gray theory is that it does not take into account the fact that the secondary electrons may not be in CPE and thus it deviates from experimental measurements. Spencer and Attix[4] improved the Bragg-Gray cavity theory by accounting for secondary electrons above a threshold Δ and this introduced a quantity that characterizes the cavity size. In the Spencer-Attix formalism,[2,4] the dose in a medium is related to the dose in the cavity at the same location in the medium by:

$$\frac{D_{med}}{D_{cav}} = \left(\frac{\overline{L}_{\Delta}}{\rho}\right)_{cav}^{med}, \tag{1.3}$$

where $\left(\frac{\overline{L}_{\Delta}}{\rho}\right)_{cav}^{med}$ is the Spencer-Attix *med*-to-*cav* mean restricted mass collision stopping-power ratio (SPR) with threshold or cutoff energy Δ. The cutoff energy Δ is used to characterize the cavity size. It is not clearly defined in the Spencer-Attix cavity theory but only vaguely described as the energy of electrons that can just cross the cavity. The SPR can be expressed in detail as:

$$\left(\frac{\bar{L}_{\Delta}}{\rho}\right)_{cav}^{med} = \frac{\int_{\Delta}^{E_{\max}} \Phi_{med}(E) \left(\frac{L_{\Delta}(E)}{\rho}\right)_{med} dE + \Phi_{med}(\Delta) \left(\frac{S(\Delta)}{\rho}\right)_{med} \Delta}{\int_{\Delta}^{E_{\max}} \Phi_{med}(E) \left(\frac{L_{\Delta}(E)}{\rho}\right)_{cav} dE + \Phi_{med}(\Delta) \left(\frac{S(\Delta)}{\rho}\right)_{cav} \Delta}, \tag{1.4}$$

where $\Phi_{med}(E)$ is the differential electron fluence spectrum of primaries and secondaries in medium *med* and $E_{\max}$ is the maximum energy in the electron fluence spectrum.

In practice, for a cavity of volume V and surface area S, the cavity size is often specified by the mean chord length which, for a convex cavity and isotropic electron fluence distribution, is given[2] by $L = 4V/S$. Then the cutoff energy Δ may be considered as the energy of electrons that have a CSDA (continuous slowing down approximation) range equal to L. The most commonly used ion chambers in radiation source calibration are plane-parallel chambers and cylindrical thimble chambers. A plane-parallel chamber has a pancake shaped cavity of radius r and thickness h. The mean chord length L is obtained as:

$$L = \frac{2h}{1 + \frac{h}{r}}. \tag{1.5}$$

For the cavity of a thimble chamber of radius r and length l, L is given by:

$$L = \frac{2r}{1 + \frac{r}{l}}. \tag{1.6}$$

1.2 Ionization chambers and the perturbation effects

The ionization chamber or ion chamber is the simplest and the mostly widely used radiation detector for measuring radiation source output in radiation therapy practice. The two common types of ion chamber are shown schematically in Figure 1.1. A few chambers which are modeled in detail in this thesis are shown in scale in Figure 1.2. For a plane-parallel chamber, a guard ring is used to define the collecting volume or sensitive volume of the chamber and to minimize the leakage current. This is accomplished by separating the collecting electrode into two parts by an insulating gap as shown schematically in Figure 1.3. Generally it is suggested[5] that the guard ring width should be at least 1.5 times larger than the cavity thickness, and the ratio of the collecting

volume diameter to the cavity thickness should be in the order of 10. The geometrical information for some plane-parallel chambers are listed in Table 1.1.

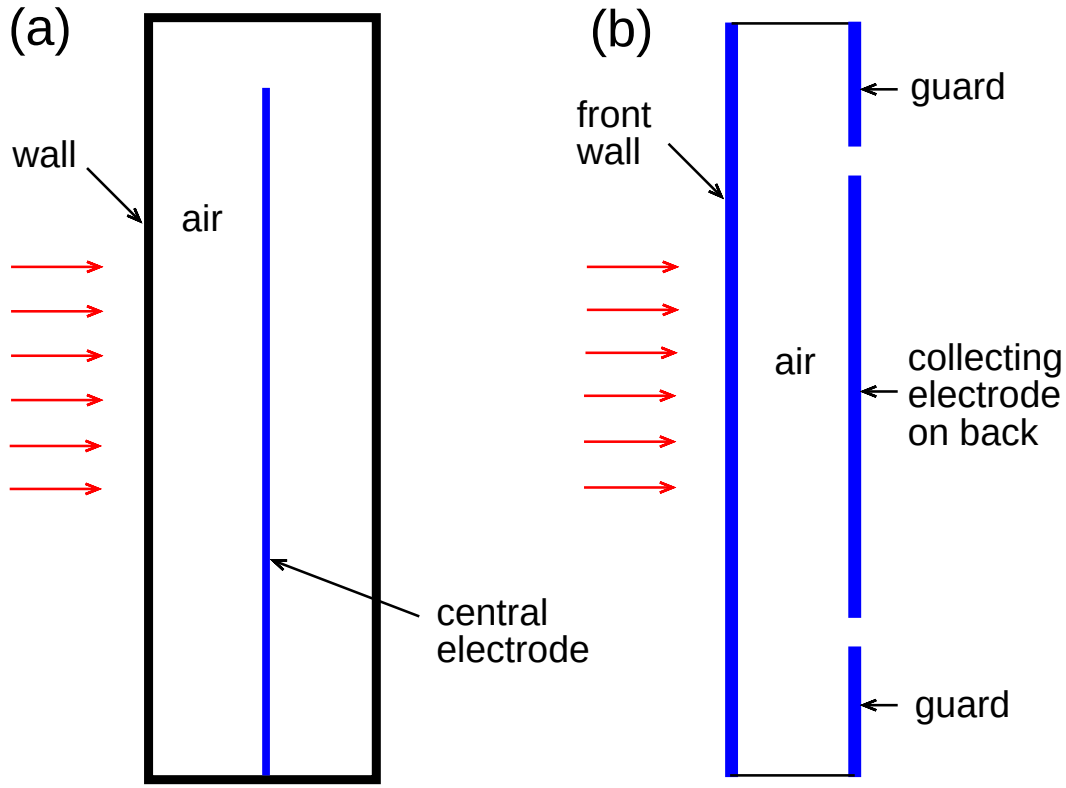

Figure 1.1: Schematic diagram of (a) a cylindrical chamber with a vertical axis of symmetry and (b) a plane-parallel chamber with a horizontal axis of symmetry. The top end of the cylindrical chamber may be hemispherical or cone-tipped.

If the chamber's sensitive cavity is filled with air of mass m_{air}, then the dose in the air cavity is related to the ionization charge released in the cavity, Q, by

$$D_{air} = \frac{Q}{m_{air}} \left(\frac{W}{e} \right), \tag{1.7}$$

where W/e, which has an accepted value[6] of 33.97 J/C, is the average energy deposited by electrons slowing down in dry air per unit charge released. The value of W/e is of fundamental importance to the study of ionizing radiations and radiation dosimetry and

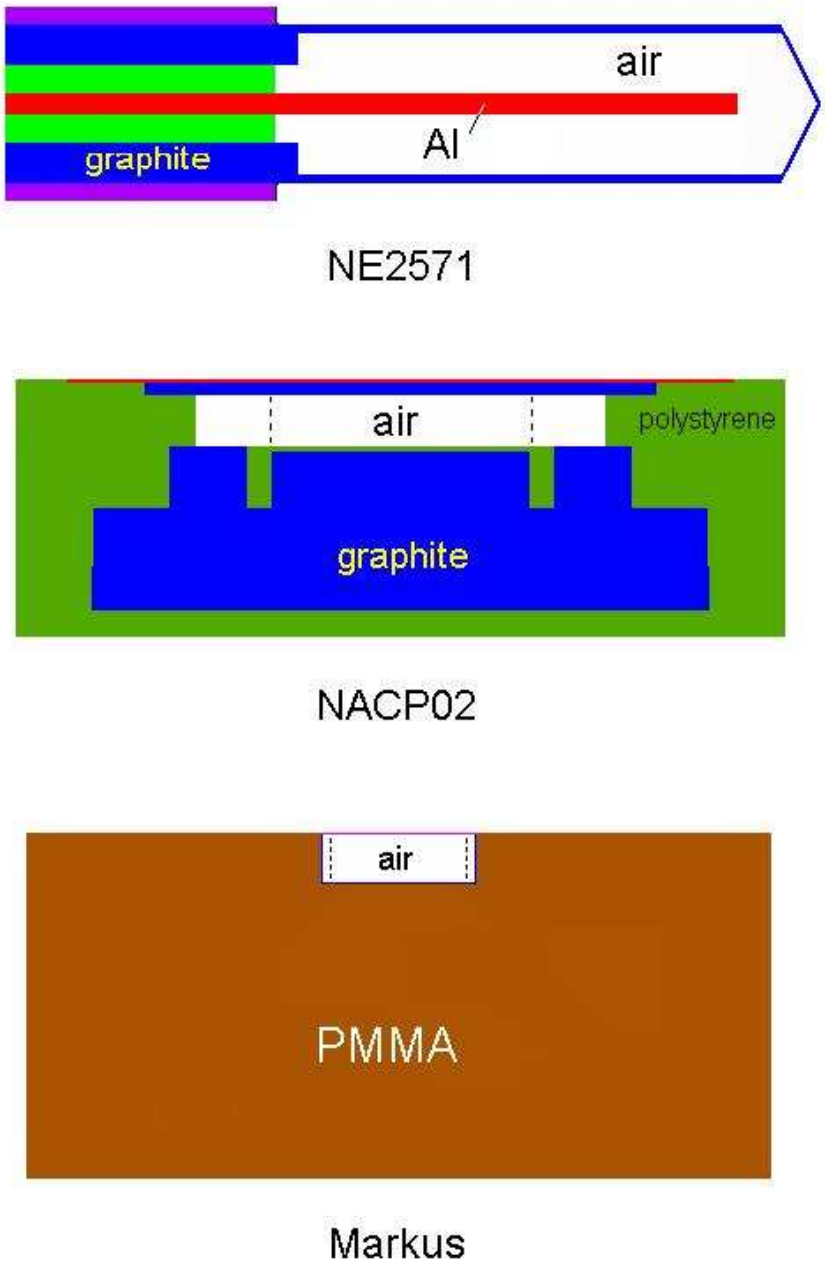

Figure 1.2: Computational models of an NE2571 Farmer-type chamber, an NACP02 plane-parallel chamber, and a Markus plane-parallel chamber. For the two plane-parallel chambers, the region between the two vertical dashed lines is the sensitive or collecting volume.

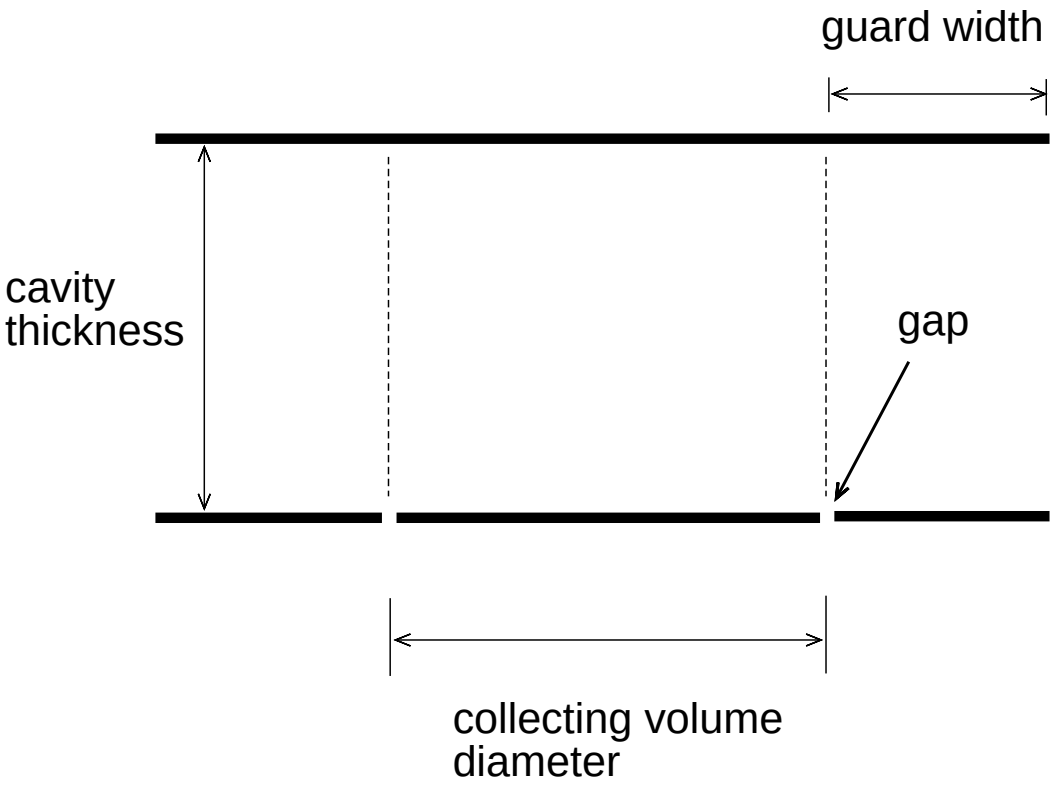

Figure 1.3: Collecting volume and guard-ring for plane-parallel chambers. The collecting volume is defined by the two vertical dashed lines.

Table 1.1: The air cavities of several plane-parallel chambers with different guard ring widths.

units: mm	Markus	Adv Markus	NACP	Roos	Attix
guard width	0.2	2	3	4	13.5
collecting volume diameter	5.3	5	10	16	12.7
cavity thickness	2	1	2	2	1

it will be discussed further in Section 3.2.

Equation 1.3 is only valid for an ideal Spencer-Attix cavity, i.e. assuming no electron fluence perturbation exists. For a real ion chamber, some corrections must be applied. Since water is the standard medium in radiation measurement, for ion chambers used in a water phantom, from Equation 1.3, the dose in the water phantom, D_{water}, is related to the dose in the air cavity with the point of measurement at the same location in the water phantom by:

$$\frac{D_{water}}{D_{air}} = \left(\frac{\overline{L}_{\Delta}}{\rho}\right)_a^w P_{\text{cel}} P_{\text{wall}} P_{\text{repl}}, \tag{1.8}$$

where $\left(\frac{\overline{L}_{\Delta}}{\rho}\right)_a^w$ (or in IAEA's notation $s_{w,a}$) is the water/air mean restricted mass collision stopping-power ratio. A series of correction factors are applied to account for any possible non-ideal conditions for the Spencer-Attix cavity theory. P_{cel} corrects for the central electrode being different from the cavity medium for a cylindrical chamber; P_{wall} corrects for the chamber wall material being different from the medium; and P_{repl} accounts for the effects of the medium being replaced by the air cavity of the chamber, or in other words, P_{repl} corrects for the disturbance of the electron fluence spectrum after introducing the air cavity. Figure 1.4 shows how P_{wall} and P_{repl} are calculated by Monte Carlo simulation. Strictly speaking, it is impossible to separate the replacement correction factor P_{repl} from the water/air stopping-power ratio $\left(\frac{\overline{L}_{\Delta}}{\rho}\right)_a^w$. However, it may

be approximately separated if a certain amount of calculation uncertainty is allowed (see Chapter 2).

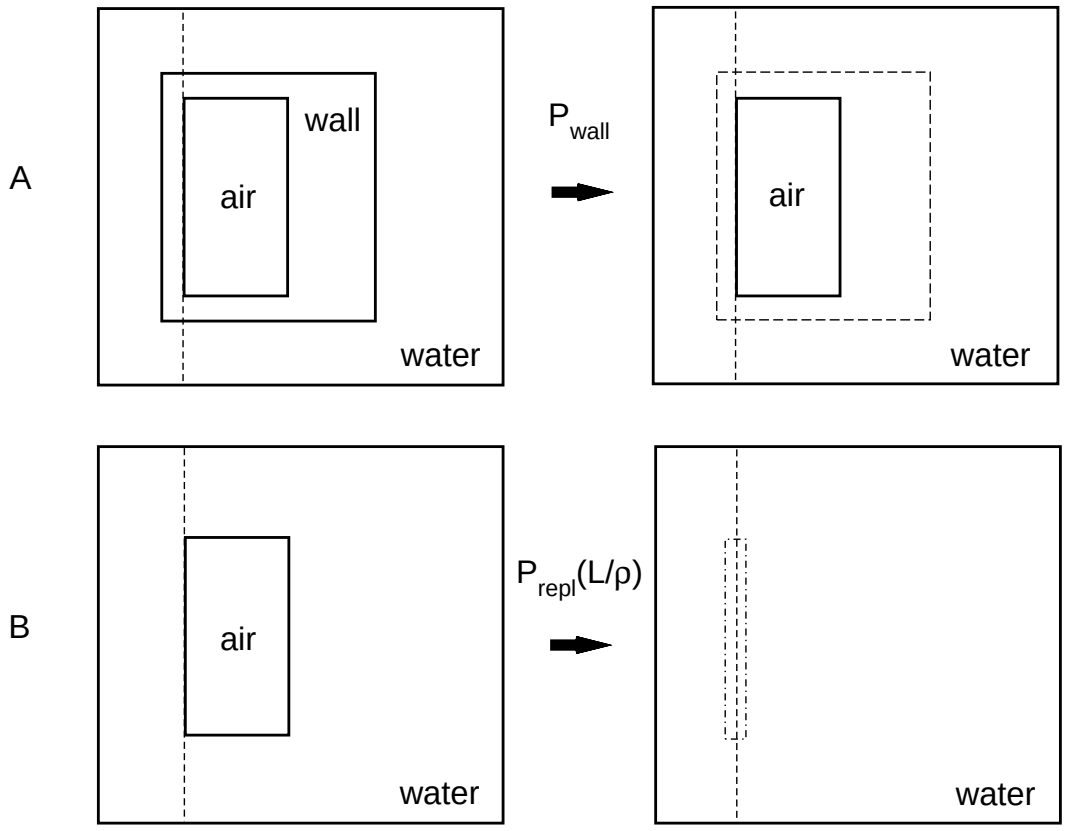

Figure 1.4: Schematic diagram of showing how P_{wall} and P_{repl} are defined for a plane-parallel chamber in a water phantom with beam entering from the left. In step A, P_{wall} is calculated as the ratio of the dose in the water-walled air cavity to that in the modeled chamber cavity. In step B, the product of P_{repl} and $\left(\frac{\overline{L}_{\Delta}}{\rho}\right)_a^w$ is calculated as the ratio of the dose in the water phantom to that in the water-walled air cavity. The vertical dashed line indicates the depth of measurement in water.

1.3 Radiation dosimetry protocols

To ensure a radiation source, either electron or photon beam, delivers the correct amount of radiation dose to a target, first of all, the radiation source output must be known; that

is, the procedures of calibrating the radiation source are needed. Hence radiation dosimetry protocols were developed. The calibration of the radiation source output is carried out using radiation dosimeters. The ion chamber was adopted as the most common radiation dosimeter for calibrating the radiation source due to its high reliability, stability, reproducibility, simplicity, and real-time readout. There are two kinds of dosimetry protocols: one is based on air kerma calibration coefficients and the other is based on absorbed dose to water calibration coefficients, but both determine the absorbed dose to water in a phantom.

1.3.1 Air kerma based protocols

Air kerma based protocols[7,8] use the air kerma calibration coefficient N_K obtained for a chamber calibrated free-in-air in a ^{60}Co beam at a standards laboratory. N_K is used to determine the cavity gas calibration coefficient N_{gas} which is used to determine dose in a water phantom by

$$D_{water} = M\ N_{gas}\ \left(\frac{\overline{L}_{\Delta}}{\rho}\right)_a^w P_{\text{cel}} P_{\text{wall}} P_{\text{repl}}, \tag{1.9}$$

where M is the chamber reading corrected for influence quantities like temperature, pressure, etc. The relationship between N_{gas} and N_K can be found elsewhere.[9]

1.3.2 Absorbed dose based protocols

Since the absorbed dose is considered the relevant quantity related to the biological effects of ionizing radiations, it is more reasonable to provide ion chambers with a calibration coefficient in terms of the absorbed dose to water. Both of the two current major dosimetry protocols, the AAPM's TG-51 dosimetry protocol[10] and the IAEA's TRS-398 Code of Practice,[11] are this kind of dosimetry protocol. The absorbed dose based protocol usually starts from an absorbed dose calibration coefficient in a ^{60}Co beam, $N_{D,w}^{^{60}Co}$,

obtained at a standards laboratory. The dose in a water phantom is determined by

$$D_{water} = M\ k_Q\ N_{D,w}^{^{60}Co}, \tag{1.10}$$

where k_Q is the quality conversion factor that converts the absorbed dose calibration coefficient in a ^{60}Co beam to that in an arbitrary beam (either photon or electron) of quality Q. By comparing Equation 1.9 and 1.10, and assuming N_{gas} is the same for different beam qualities, one may get an expression for k_Q as

$$k_Q = \frac{\left[(\overline{L}_\Delta/\rho)_a^w\ P_{cel}\ P_{\text{wall}}\ P_{\text{repl}}\right]_Q}{\left[(\overline{L}_\Delta/\rho)_a^w\ P_{cel}\ P_{\text{wall}}\ P_{\text{repl}}\right]_{^{60}Co}}. \tag{1.11}$$

For photon beams, the k_Q values for most chambers are provided in the protocols.[10,11] For electron beams, k_Q is written in TG-51 as the product of three factors:[10]

$$k_Q = P_{gr}^Q k'_{R_{50}} k_{ecal}, \tag{1.12}$$

where P_{gr}^Q is the gradient correction factor for cylindrical chambers, $k'_{R_{50}}$ is the electron beam quality conversion factor, and k_{ecal} is the photon-electron conversion factor. P_{gr}^Q can be determined experimentally as the ratio of the chamber readings M with the central axis of the chamber at depth $z + 0.5r$ and z,[10]

$$P_{gr}^Q(z) = \frac{M(z + 0.5r)}{M(z)}, \tag{1.13}$$

where r is the radius of the cylindrical chamber.

In photon beams, cylindrical chambers are preferred for source calibration as the plane-parallel chambers had unknown wall effects in photon beams when the protocols were developed. In electron beams, on the other hand, plane-parallel chambers are preferred for source calibration, especially in low-energy (<10 MeV) electron beams where cylindrical chambers have shown very large perturbation effect. Cylindrical chambers are recommended for use only in high-energy electron beams.[10,11]

1.3.3 Beam quality and reference depth

Photon beams

In AAPM's TG-51 dosimetry protocol,[10] the photon beam quality is specified by the percent depth dose at 10 cm depth, excluding the dose contribution from contaminant electrons, denoted by $\%dd(10)_x$. In IAEA's TRS-398 Code of Practice,[11] the ratio of the tissue phantom radio (TPR) at 20 cm depth to that at 10 cm depth is used as the photon beam quality specifier, denoted as TPR^{20}_{10}. The reference depth or the calibration depth is usually at 10 cm in a water phantom.

Electron beams

For electron beams, both the AAPM's TG-51 dosimetry protocol[10] and the IAEA's TRS-398 Code of Practice[11] use the depth at which the dose falls to 50% of maximum dose, R_{50}, as the electron beam quality specifier. The reference depth or the calibration depth is

$$d_{ref} \;=\; 0.6\; R_{50} \;-\; 0.1 \text{ (cm)}. \tag{1.14}$$

In the AAPM's TG-21 dosimetry protocol,[7] the mean electron energy at the surface $\overline{E}_0$ was used as the electron beam quality specifier and the reference depth is at the depth of maximum dose d_{max}. Using Harder's relation,[7] the mean electron energy at depth z, $\overline{E}_z$, may be determined:

$$\overline{E}_z = \overline{E}_0(1 - \frac{z}{R_p}) \tag{1.15}$$

where R_p is the practical range. $\overline{E}_0$ is related to R_{50} by $\overline{E}_0 = 2.33R_{50}$.

1.4 The values of P_{repl} in dosimetry protocols

The replacement correction factor P_{repl} can be expressed as[7]

$$P_{\text{repl}} = P_{gr} P_{fl} \tag{1.16}$$

where P_{fl} is the fluence correction factor (or the fluence perturbation p_{cav} in the IAEA's notation[11]) which accounts for the change of the shape of the electron fluence spectrum; and P_{gr} is the gradient correction factor (or the displacement perturbation p_{dis} in the IAEA's notation[11]) which accounts for the change of the amplitude of the electron fluence spectrum. P_{gr} can be dealt with by either a multiplicative factor as in Equation 1.12 or by the concept of the effective point of measurement (EPOM) as discussed in Appendix A.

For plane-parallel chambers in electron beams, the effective point of measurement is taken at the center of the inner surface of the front wall and thus P_{gr}=1; so P_{repl} is the same as P_{fl}. In the AAPM's TG-21[7] and the IAEA's TRS-277[8] dosimetry protocols, the values of both P_{repl} and the wall correction, P_{wall}, are taken to be 1 for all plane-parallel chambers at all beam qualities. In TG-39[12] and IAEA TRS-381[5] protocols, non-unity values of P_{repl} for some plane-parallel chambers (e.g. Markus chamber) are adopted, though P_{wall} is still unity. Currently, both the TG-51[10] and IAEA TRS-398[11] dosimetry protocols have assumed unity P_{repl} values for all well-guarded plane-parallel chambers.

For plane-parallel chambers in mega-voltage photon beams, dosimetry protocols assume a unity value of P_{repl} for all plane-parallel chambers in ^{60}Co photon beams and this is generally assumed true of all mega-voltage photon beams, when the inner front face of the cavity is taken as the point of measurement.

For cylindrical chambers in electron beams, although they are not recommended for use in low-energy electron beams, the values of P_{repl} (or P_{fl}) at the depth of maximum dose, d_{max} (where $P_{gr} = 1$), are tabulated in the TG-21[7] dosimetry protocol for a variety of chamber radii for electron beams as a function of mean energy at the point

of measurement from 2 to 20 MeV. These values are mainly based on the experiments performed by Johansson et al[13] who measured the electron fluence perturbation factor P_{fl} at d_{max} by comparing ionization readings of various cylindrical chambers to those from a plane-parallel chamber which was assumed to be perturbation free. In TG-51,[10] the calibration depth for electron beams is at the reference depth, d_{ref} (Equation 1.14), where no P_{fl} values are available for high-energy electron beams and it is assumed that one may use values determined at d_{max}, with the same mean electron energy at depth. The value of P_{gr} at d_{ref} is determined experimentally by using Equation 1.13.

For cylindrical chambers in photon beams, P_{fl} is taken to be unity for depths beyond d_{max} due to the transient charged particle equilibrium, so P_{repl} is P_{gr}. In photon beams, P_{repl} represents a significant uncertainty in dosimetry protocols.[14] For example, the AAPM's TG-51[10] and TG-21[7] dosimetry protocols use a value of $P_{\text{repl}} = 0.992$ for a cylindrical chamber of inner diameter of 6 mm in a ^{60}Co beam. This value is from the work of Cunningham and Sontag[15] who derived P_{repl} based on analytical calculations and experiments. For the same quantity the IAEA's TRS-398[11] Codes of Practice use a value of 0.988 which is based on the measured data of Johansson et al.[13] This one half percent difference in the values used by the IAEA and the AAPM protocols may be the largest single difference between them, although in TG-51 and TRS-398, the differences have a reduced effect because only ratios of P_{repl} values are used.

1.5 The EGSnrc Monte Carlo code system

The Monte Carlo simulation code used in this study is the EGSnrc code system.[16] EGSnrc is a major upgrade from the EGS (Electron-Gamma-Shower) code system, which was a general purpose software package originally developed at Stanford by Ford and Nelson[17] in the 1970s for the Monte Carlo simulation of electron, positron, and photon transport in any geometrical structures. The programming language is FORTRAN. The

EGSnrc code system was released in February 2000. Although based on the EGS4[18] system, it includes many improvements, such as a new multiple scattering theory, a better electron-step algorithm, and a better boundary crossing algorithm.[19] Thus the calculation accuracy of ion chamber response is dramatically improved, with a systematic accuracy of about 0.1% relative to its own cross sections.[20]

1.5.1 EGSnrc user-codes used in this study

The fundamental particle transport mechanism is included in the EGSnrc code itself. In order to perform a simulation of any significance or produce a practical application, the user must use an existing user-code or write a new user-code for specific calculations. Several EGSnrc user-codes[21] are used in this study for various purposes. They are CAVRZnrc (for cavity dose in cylindrically symmetric geometry or RZ geometry), SPRRZnrc (for stopping-power ratios), DOSRZnrc (for depth-dose curves), FLURZnrc (for electron fluence and fluence spectra in RZ geometry), BEAMnrc[22,23] (for realistic linac head modeling), and the new C++-based user-code Cavity[24,25] (for dose calculations in non-RZ geometries such as thimble chambers).

1.5.2 Improvement of the user-codes

CSnrc

CSnrc[26] is a more recent EGSnrc user-code built on CAVRZnrc and it implements a correlated sampling technique (not available in the EGSnrc distribution package). CSnrc is very efficient in calculating dose ratios for similar geometries which are commonly encountered in radiation dosimetry. It has been extensively used for the wall correction calculation in ion chamber dosimetry,[27,28] and can be applied to many other applications as well. CSnrc is used to calculate the energy and beam quality dependence of the

response of LiF TLD chips in mega-voltage photon and electron beams. The results agree within the calculation uncertainty of <1% with those calculated by Mobit et al.[29,30] using EGS4/PRESTA.[18,31] CSnrc is mainly used in this study for the calculation of the response of a Scanditronix-Wellhöfer EFD electron diode in a water phantom irradiated by electron beams. These results are presented in Appendix B. Some new capabilities of the code were developed and implemented in these investigations, aside from minor bug fixes. They include (1) using a phase-space file generated by a BEAMnrc simulation as the radiation source, and (2) using a dynamic linac model by BEAMnrc code as the radiation source. These new features have been employed in the study for the diode dosimeter.

Cavity

The FLURZnrc user-code can be used for the calculation of the differential electron fluence spectrum. One limitation is that it only deals with cylindrical (or RZ) geometry, so it can not be applied to the study of the electron fluence spectrum in, e.g. a thimble chamber in a phantom. On the other hand, the C++-based Cavity code can be used essentially for any kind of geometrical structure, but the current version does not have the capability of calculating the electron fluence spectrum. In order to study the electron fluence spectrum in a thimble chamber, a feature to calculate the electron fluence spectrum and the total electron fluence was developed and implemented in the Cavity code. Figure 1.5 shows that it gives identical results to those calculated by the extensively used FLURZnrc user-code in either photon or electron beams when RZ geometries are modeled.

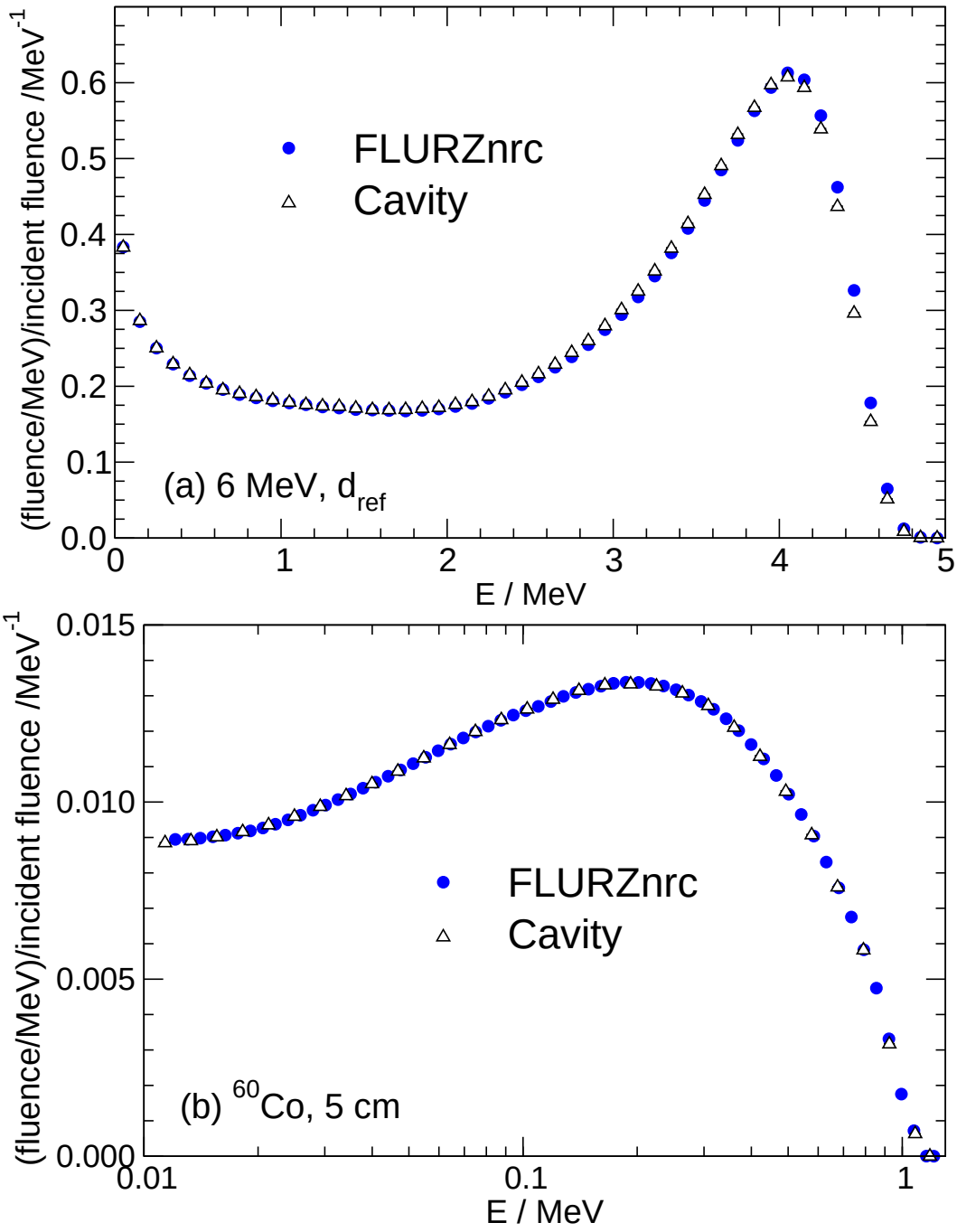

Figure 1.5: Comparison of the electron fluence spectra calculated by the FLURZnrc code and the improved Cavity code (a) at d_{ref} in a 6 MeV electron beam, and (b) at 5 cm in a ^{60}Co beam.

Chapter 2

Calculation of the replacement correction factors P_{repl}

2.1 Introduction

Using the Spencer-Attix formalism, for a water-walled chamber with no central electrode, Equation 1.8 can be simplified to give:

$$\frac{D_{water}}{D_{air}} = \left(\frac{\overline{L}_{\Delta}}{\rho}\right)_a^w P_{\mathrm{repl}}. \tag{2.1}$$

Equation 2.1 can be considered as the definition of the replacement correction factor P_{repl}. Experimental determination of P_{repl} values is not an easy task since it is hard to separate the chamber wall effect from the medium replacement or displacement effect. It will be very useful in clinical radiation dosimetry if one can calculate P_{repl} with high accuracy. Analytical methods of calculating P_{repl} in electron beams have been tried before as reviewed by Nahum,[32] but the results are not very satisfactory, especially for cylindrical chambers. The first trial of Monte Carlo calculation of P_{repl} was made by Ma and Nahum[33] who used the EGS4 code. They studied P_{repl} values at d_{max} for plane-parallel chambers in electron beams. However, their results appear to have a systematic

error of at least 0.5% due to reasons discussed later. Recently, many researchers[28,34–37] used Monte Carlo method with EGSnrc to calculate P_{repl} values for various chambers. They all used an indirect method (the method labelled SPR below) to calculate the values of P_{repl}. In this chapter, four different ways of calculating P_{repl} using Monte Carlo simulations are proposed and their relative merits are discussed.

For all the calculations in this work, unless otherwise specified, the radiation sources, the phantom geometries, and the Monte Carlo simulation parameters are as follows. For a ^{60}Co beam, the spectrum source is from Mora et al.[38] For linac photon beams, the spectra are from Monte Carlo simulations of a Varian linac[39] with nominal energies from 6 MV to 18 MV. For electron beams, the spectra are from Monte Carlo simulations of a Varian Clinac 2100C linac[40] with nominal energies from 6 MeV to 18 MeV. A spectrum source from a 22 MeV Elekta SL25 electron beam is also used. All the radiation sources are at 100 cm source-surface-distance (SSD), except the ^{60}Co beam which has an SSD of 80 cm, and all the field sizes are 10×10 cm^2 equivalent. For the RZ geometry, or FORTRAN-based EGSnrc user-codes, a cylindrically symmetric water phantom of radius 20 cm and depth 30 cm is used. For the C++-based Cavity code, e.g. thimble chamber calculations, the water phantom is a cube of 30 cm sides. The point of measurement is at the proximal face of the cavity for a plane-parallel chamber and is at the center of the cylindrical cavity for a cylindrical thimble chamber. The air cavity of a Farmer chamber is usually of length 2 cm and radius 3 mm. An NACP02 plane-parallel chamber has an air cavity 2 mm in thickness, 8 mm in overall radius and 5 mm in collecting volume radius. The cavity dose is only scored in the collecting volume of the chamber cavity and the water phantom dose is scored in a voxel of thickness 0.2 mm. The electron and photon energy thresholds for production and tracking (AE, ECUT and AP, PCUT) are 521 keV and 10 keV, respectively, except for the calculations using the HDA method (see later) where AE=ECUT=512 keV with an HDA slab thickness of 3 μm. In most situations, the number of histories is such that the calculated value of

P_{repl} has a statistical uncertainty of less than 0.1%.

2.2 Stopping-power ratio method (SPR)

Making the depth dependences explicit, Equation 2.1 can be rearranged to give:

$$P_{\text{repl}}^{SPR}(z) = \frac{D_{water}(z)}{D_{air}(z)} \Big/ \left(\frac{\bar{L}_{\Delta}(z)}{\rho} \right)_a^w \tag{2.2}$$

Equation 2.2 gives an indirect method of calculating P_{repl} at depth z as the quotient of the ratio of the dose in the water phantom at z to that in the air cavity positioned at z and the water/air stopping-power ratio (SPR) at depth z. Hence this method is called the SPR method. This method is used by most researchers in calculating the values of P_{repl}. The shortcoming of the SPR method is that one always needs to do a separate stopping-power ratio calculation.

2.3 Electron fluence method (FLU)

P_{repl} can be expressed in an integral form,[33] if the track-end terms are ignored, as

$$P_{\text{repl}} = \frac{\int_{\Delta}^{E_{\max}} \Phi_w(E) \left(\frac{L_{\Delta}(E)}{\rho} \right)_{cav} dE}{\int_{\Delta}^{E_{\max}} \Phi_{cav}(E) \left(\frac{L_{\Delta}(E)}{\rho} \right)_{cav} dE}. \tag{2.3}$$

If the electron fluence spectrum in an air cavity, $\Phi_{cav}(E)$, differs from that in water, $\Phi_w(E)$, at the point of measurement by only a constant scale factor, i.e. $\Phi_w(E) = const \times \Phi_{cav}(E)$, then Equation 2.3 is reduced to the ratio of the total electron fluences in the phantom and in the cavity

$$P_{\text{repl}} = \frac{\Phi_w}{\Phi_{cav}}. \tag{2.4}$$

Originally, Ma and Nahum[33] mentioned this approach but did not actually calculate it. The shortcoming of this FLU method is the requirement of the proportionality of the differential spectra.

2.4 Direct methods of calculating P_{repl}

There are ways of directly calculating the values of P_{repl}. Here the word 'direct' means the stopping-power ratio evaluation is not necessary. Figure 2.1 depicts the transition from the dose in an air cavity (first box) to the dose in a water phantom (third box), taking a plane-parallel chamber as an example (it is the same for a cylindrical chamber except the point of measurement is at the center of the cavity). Conceptually, the transition can be considered in two ways, either route A or route B as shown in Figure 2.1.

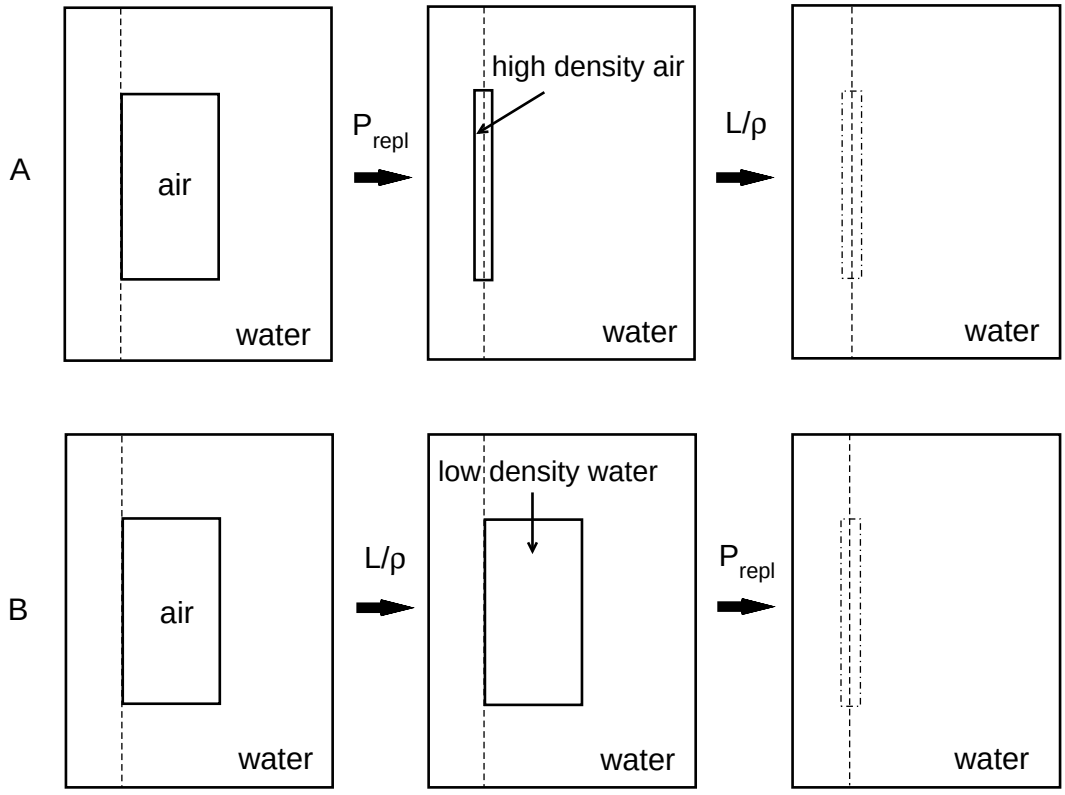

Figure 2.1: Schematic diagram of two routes for calculating P_{repl} for a water-walled plane-parallel chamber in a water phantom. In route A, P_{repl} is calculated as the ratio of the dose in the HDA slab to that in air cavity. In route B, P_{repl} is calculated as the ratio of the dose in the water phantom to that in the LDW cavity. The dashed line indicates the depth of measurement in water. From paper II.

2.4.1 High-density-air (HDA) method

In route A, a thin slab of 'high density air' (HDA) material is centered at the point of measurement z. Initially, it is assumed that the HDA slab is thin enough so it does not affect the electron fluence spectrum compared to that in a pure water phantom. HDA is an artificial material that has all the dosimetric properties of normal air except its density is equal to that of water. In preparing the HDA data set, the density correction data for normal-density air are used. When using this method, the value of $P_{\rm repl}$ at the depth z is

$$P_{\rm repl}^{HDA}(z) = \frac{D_{HDA}(z)}{D_{air}(z)}, \tag{2.5}$$

where D_{HDA} and D_{air} are the doses in the HDA slab and in the air cavity of the wall-less chamber, respectively. The superscript HDA is used to indicate the calculation method is HDA. As the HDA and air are the same material, the stopping-power ratio is unity.

2.4.2 Low-density-water (LDW) method

In route B in Figure 2.1, the air in the cavity is replaced by a 'low density water' (LDW) material, which is water but with a density of normal air, and a density correction corresponding to normal-density water. The assumption here is that the electron fluence spectrum is the same in both cavities. For $P_{\rm repl}$ value at depth z calculated by this LDW method, one has:

$$P_{\rm repl}^{LDW}(z) = \frac{D_{water}(z)}{D_{LDW}(z)}, \tag{2.6}$$

where D_{water} and D_{LDW} are the doses in water and in the cavity of the wall-less chamber filled with LDW, respectively. The superscript LDW is used to indicate the calculation method is LDW. As the LDW and water are the same material, the stopping-power ratio is unity.

Originally, the HDA method was used by Ma and Nahum[33] in their calculation

of P_{repl} for plane-parallel chambers. Ma and Nahum[41] also used a method similar to the LDW method to calculate the displacement correction factor for cylindrical chambers in medium energy photon beams but it differs from our LDW method as they calculated the water kerma ratio as opposed to dose ratio and the kerma was averaged over the whole chamber volume.

2.5 Systematic uncertainties of calculating P_{repl}

2.5.1 Uncertainty of the HDA method

As mentioned earlier, the HDA method assumes the electron fluence spectrum is the same in the HDA and in the water. This is the basic assumption the Bragg-Gray or Spencer-Attix cavity theory requires for its applicability. To check the validity of this assumption, the dose is calculated in the HDA slab and in the same slab with HDA being replaced by water, at a variety of slab thicknesses with the radius fixed at 1 cm, in both a 6 MeV electron beam (at d_{ref} and R_{50}) and a ^{60}Co beam (at depth of 5 cm). The energy cutoff for electrons is set at 512 keV in these calculations due to the very thin slab used. Figure 2.2 shows that the dose to the water slab in a water phantom is independent of the slab thickness used (from 0.1 μm to 0.4 mm). However, for the HDA slab in the water phantom the dose varies significantly, indicating a non-negligible perturbation effect for thicker slabs, especially for the ^{60}Co beam and for the electron beam at R_{50}. One concludes that the HDA slab has to be thin enough to make the perturbation effect negligible when using the HDA method. A direct calculation of the electron fluence spectrum in the HDA slab and in the water phantom gives the results shown in Figure 2.3. For HDA slab thickness of 0.2 mm, there is a difference in the spectrum in the water phantom and HDA slab for energies below 100 keV. However, when the HDA slab thickness decreases to 4 μm, the spectrum in the HDA matches that

for water as illustrated in the figure, indicating a negligible perturbation effect. Now the question is, starting from which HDA slab thickness does the fluence perturbation become negligible?

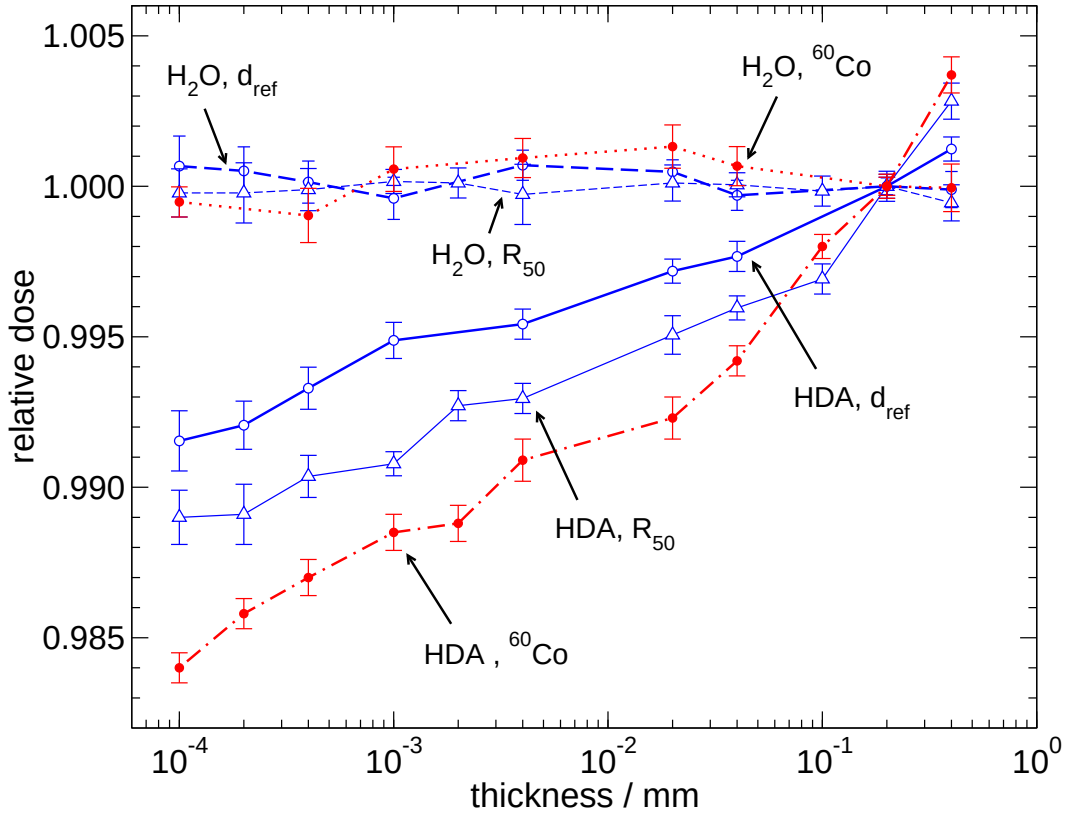

Figure 2.2: Dose in a water slab and an HDA slab as a function of the slab thickness. The calculation is at d_{ref} and R_{50} in the 6 MeV electron beam and at depth 5 cm in the ^{60}Co beam. The doses are normalized at a slab thickness of 0.2 mm. From papers II and V.

For the HDA slab, using the Spencer-Attix relationship in Equation 1.3, taking water and HDA as the phantom and cavity materials, one has,

$$\frac{D_{water}}{D_{HDA}} = \left(\frac{\overline{L}_{\Delta}}{\rho}\right)_a^w . \tag{2.7}$$

As Δ is a monotonic function of cavity size, if an HDA slab is used as the cavity, Δ will be a monotonic function of the slab thickness. Figure 2.4 shows as a function of

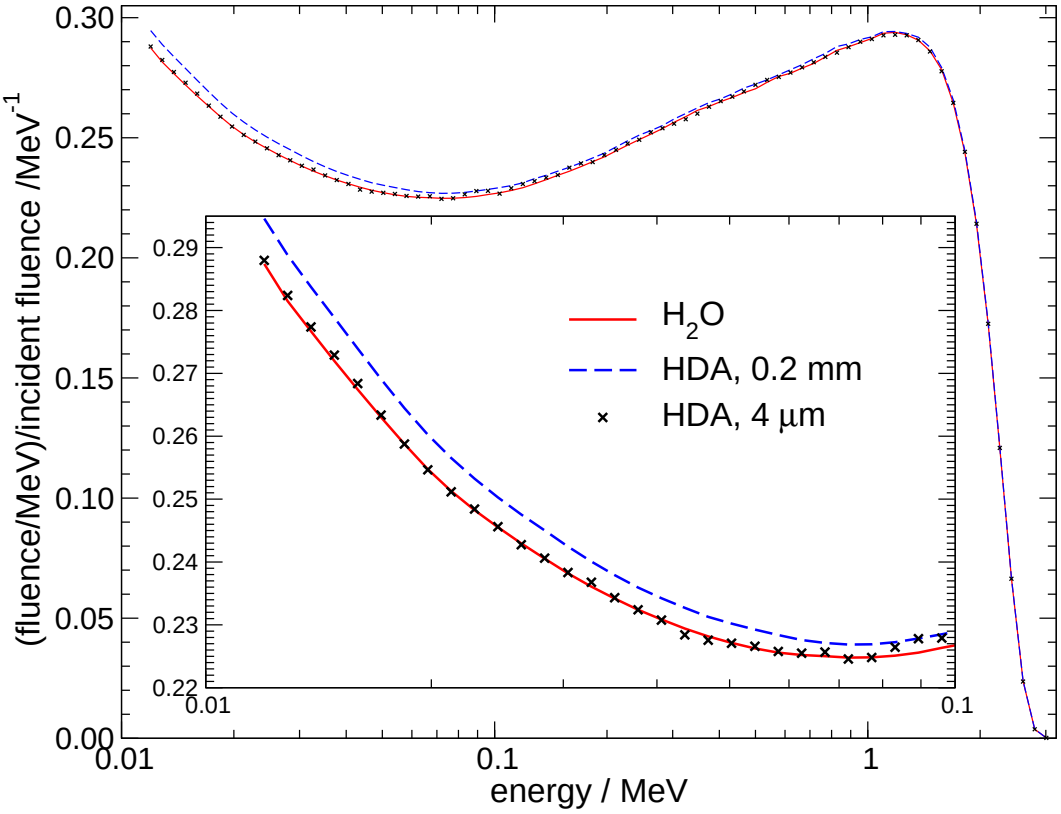

Figure 2.3: Electron fluence spectra in a water slab (0.2 mm thick) and in HDA slabs of thicknesses of 0.2 mm and 4 μm. The calculation is at R_{50} in the 6 MeV electron beam. The inset shows the magnified portion of the curves from 10 keV to 100 keV. The spectra calculation uncertainty is about 0.2% or less. From paper II.

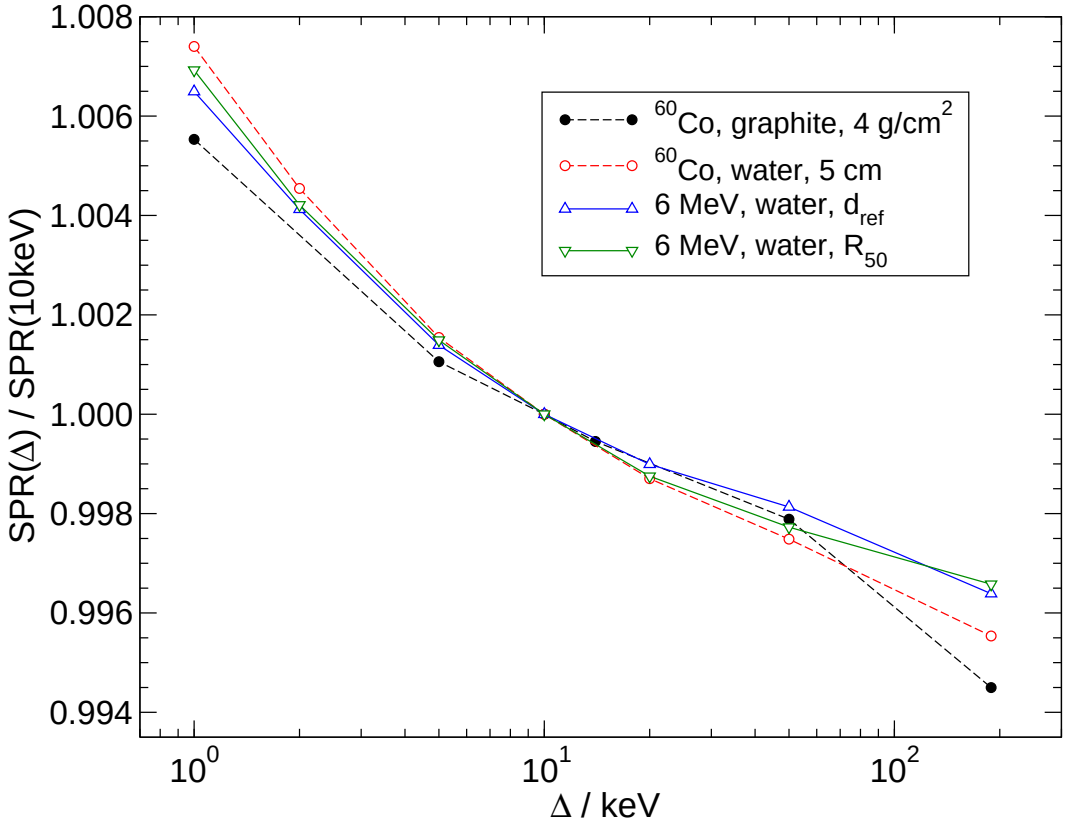

Figure 2.4: Variation of the water/air or graphite/air restricted mass collision stopping-power ratios at different depths in water or graphite phantoms as a function of the energy cutoff Δ. Data are normalized at Δ=10 keV. The radiation source is either a ^{60}Co beam (100 cm source-detector distance for the graphite phantom) or a 6 MeV electron beam. From paper V.

Δ for the graphite/air SPR in a ^{60}Co beam and water/air SPR in either a ^{60}Co beam or a 6 MeV electron beam. The SPRs are normalized at Δ=10 keV so that only the variation with Δ is emphasized. Since D_{water} is constant at a specific position in a phantom, Equation 2.7, together with Figure 2.4, suggests that the dose in an HDA slab can not be a constant while one is reducing the HDA slab thickness thus decreasing Δ. This is true even if there exists no electron fluence perturbation. The dose in the HDA slab is in fact determined by both the water/air SPR and a possible electron fluence perturbation. To eliminate the influence of the water/air SPR on the dose in the HDA slab, from Equation 2.7, the quotient $(D_{water}/D_{HDA})/(\frac{\overline{L}_{\Delta}}{\rho})$ is evaluated and is expected to be unity for an unperturbed cavity. Before proceeding, one still needs to find out how the cutoff energy Δ is related to the HDA slab thickness. By "definition", Δ is the energy of electrons that can just cross the cavity. A series of broad, parallel, mono-energetic electron beams are incident on a semi-infinite HDA slab and the depth-dose curves are calculated, from which the practical ranges of the electrons are found by extending the maximum tangent line on the dose fall-off area to the abscissa. Figure 2.5 shows the results of the practical ranges which are slightly less than the corresponding CSDA ranges. The HDA slab thickness corresponding to a given cutoff Δ can be taken as the slab thickness equal to the practical range from this figure.

Based on this assumption, the quantity $(D_{water}/D_{HDA})/(\frac{\overline{L}_{\Delta}}{\rho})$ is calculated as a function of HDA slab thickness as shown in dashed lines in Figure 2.6 for the 6 MeV electron beam and the ^{60}Co beam. It is seen that in both cases this quantity stabilizes and is close to 1 as the thickness becomes smaller than 20 μm (for electron beam, it is close to 1 just below 0.1 mm thickness), meaning the electron fluence perturbation is negligible for the HDA thickness less than 20 μm for either electron or photon beams. The Δ value selected here is based on the practical range being equal to the HDA slab thickness. If the Δ value is taken as the mean chord length as defined in Equation 1.5,

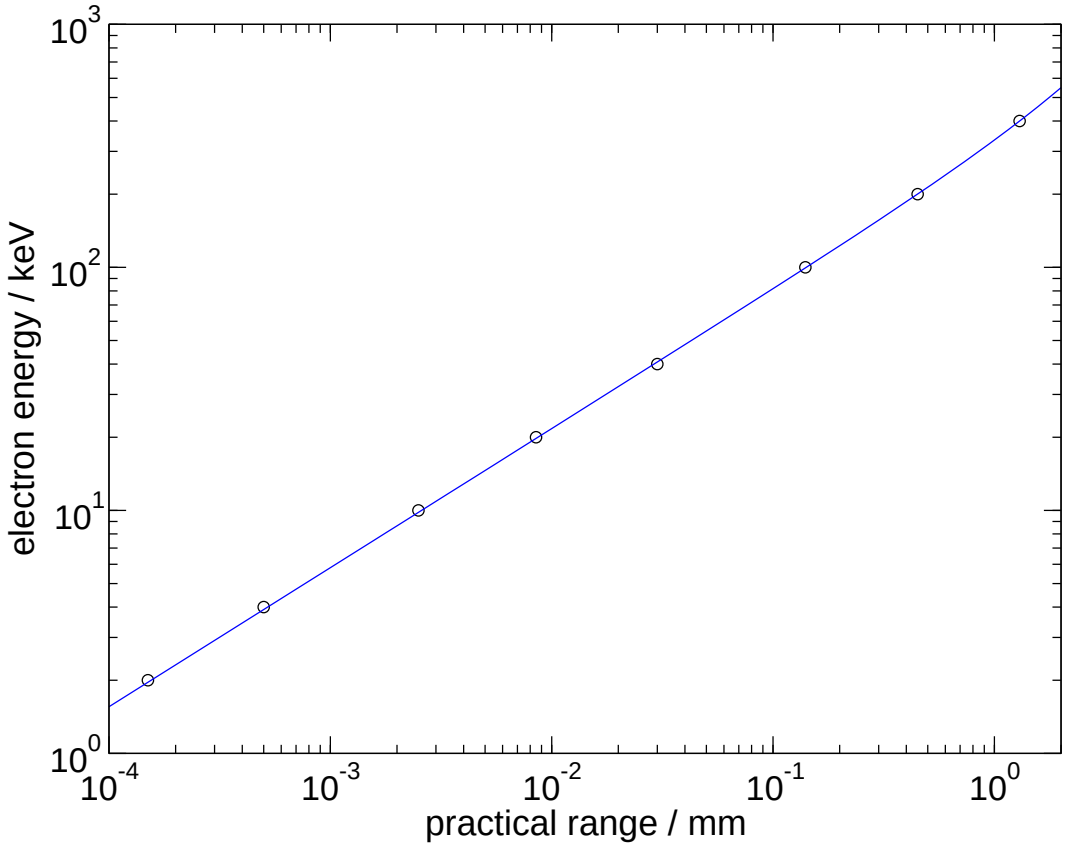

Figure 2.5: Relationship between the practical range of electrons in high-density air (HDA) and the energy of the mono-energetic, parallel-incident broad electron beams. The solid line is calculated from an empirical fitted formula between the electron energy and the practical range. From paper V.

which is 2 times the HDA thickness (since $h \ll r$), then the results are represented by the solid lines in Figure 2.6. The difference between these two is at most 0.1-0.2%. The solid lines are even closer to 1, suggesting the mean chord length L is a reasonbly good cavity size specifier, in agreement with other studies.[42]

Since D_{HDA} is not a constant as the HDA thickness is decreasing, it appears that P_{repl}^{HDA} will not have a unique value. That means a particular thickness of the HDA slab must be chosen. The reasonable choice is such that the cutoff energy Δ used in the water/air SPR evaluation must be the same for both the HDA slab and the air cavity of a particular chamber. Current dosimetry protocols[10,11] adopted a single value of $\Delta = 10$ keV for all kinds of commonly used chambers. This is strictly not correct, but practically it is acceptable since the water/air SPR only varies by 0.1% when Δ varies from 10 to 20 keV (see Figure 2.4), corresponding to an air cavity size from 2 to 7 mm. With $\Delta = 10$ keV, the appropriate HDA slab thickness is 2.5 μm, and if the mean chord length is used to specify the cavity size, the real HDA slab thickness would have to be 1.25 μm. Either way, the thickness is well below the value of 20 μm where the electron fluence perturbation is diminishing. The difference between the dose in the HDA slab of 2.5 μm and of 1.25 μm is only 0.1-0.2%. This means that the systematic uncertainty of P_{repl} values resulting from the uncertainty of selecting an appropriate HDA slab thickness is 0.1-0.2%. The uncertainty related to the selection of an appropriate HDA slab thickness is inherent in the Spencer-Attix cavity theory. It introduces a systematic uncertainty in the calculation of P_{repl}, in addition to the statistical uncertainty of Monte Carlo calculation method. For high atomic number or high-Z materials like lead, the stopping-power ratio changes very rapidly with cutoff energy Δ (about 1% from 10 keV to 20 keV for lead) and the electron fluence perturbation is also expected to be very large for an HDA slab in the high-Z material. This will make it impossible to calculate the P_{repl} values by the HDA method for high-Z materials.

2.5. SYSTEMATIC UNCERTAINTIES OF CALCULATING P_{REPL}

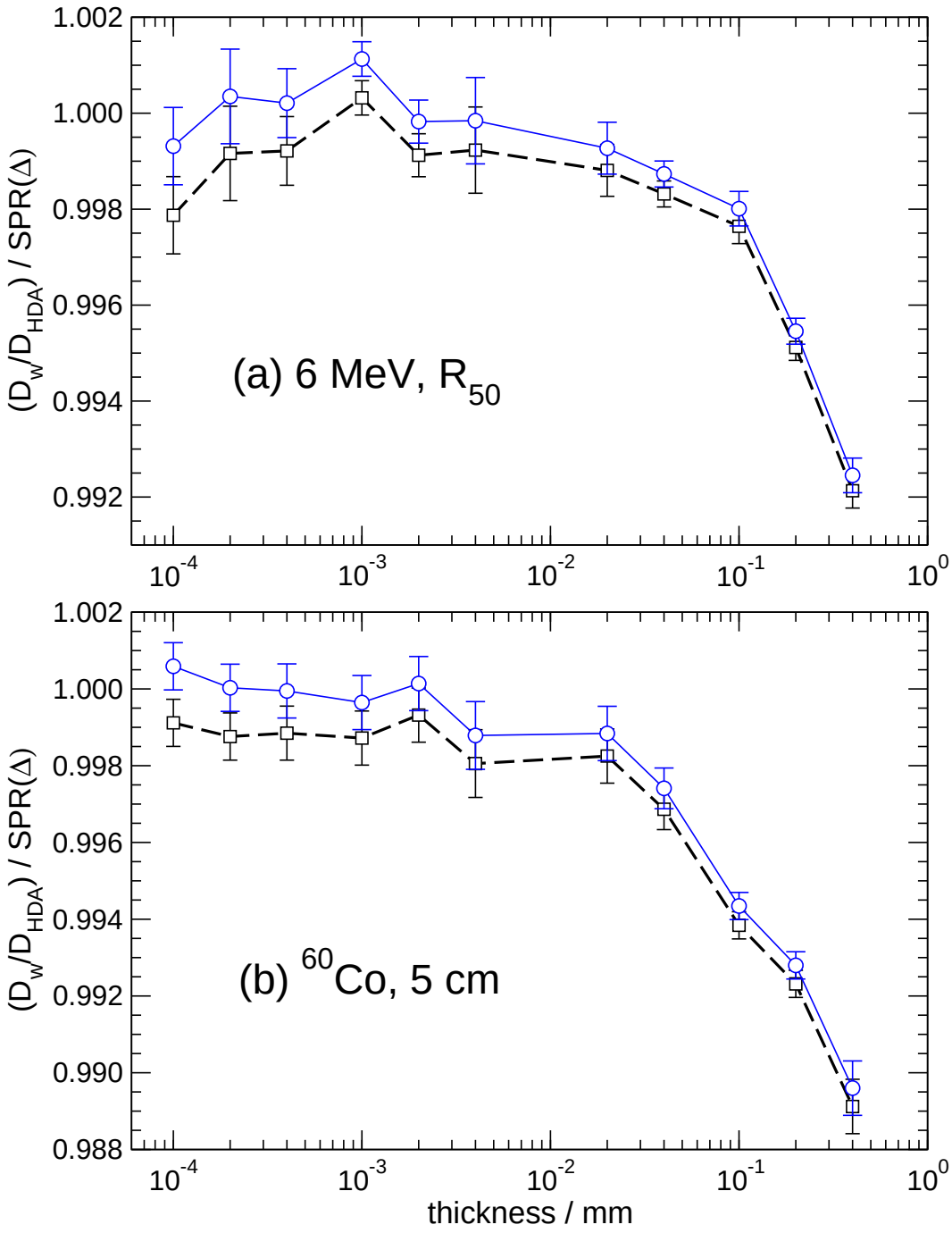

Figure 2.6: The dose ratio (water to HDA) divided by the restricted water/air stopping power ratio as a function of the HDA slab thickness at (a) R_{50} in a 6 MeV electron beam, and (b) 5 cm depth in a ^{60}Co beam. The cutoff energy Δ for the stopping-power ratio evaluation is equal to the energy of electrons that have a practical range either equal to the HDA thickness (dashed lines) or 2 times the thickness (solid lines). From paper V.

2.5.2 Uncertainty of the LDW method

If one assumes P_{repl} calculated by Equation 2.1 or 2.2 is the 'true' replacement correction and P_{repl}^{LDW} is the replacement correction calculated by the LDW method, then one may get from Equation 2.2 and 2.6

$$\frac{P_{\text{repl}}^{SPR}}{P_{\text{repl}}^{LDW}} = \frac{D_{LDW}}{D_{air}} \Big/ \left(\frac{\bar{L}_{\Delta}}{\rho}\right)_a^w. \tag{2.8}$$

For an ideal Spencer-Attix cavity, the right-hand side of Equation 2.8 should be very close to unity. Thus one may find the uncertainty of the LDW method by calculating the quotient on the right-hand side of Equation 2.8. A few typical scenarios will be discussed below.

Plane-parallel chambers in electron beams

For an NACP02 chamber cavity at various depths in a 6 MeV electron beam, the quotient is shown in Figure 2.7 for three different Δ values. Figure 2.7 shows that: (1) there is only a small fluence perturbation due to material difference; for a given value of Δ, the ratio varies less than 0.2% ($1\sigma < 0.04\%$) from the surface to R_{50}; (2) the ratio varies with Δ but is not very sensitive to the value, varying less than 0.3% at a given depth for Δ ranging from 5 to 20 keV; (3) for $\Delta = 10$ keV, near d_{ref}, the ratio is very close to unity, i.e. the 10 keV value of Δ commonly used in ion chamber dosimetry is a good choice at this depth. The slight decrease in the ratio with depth is consistent with the required value of Δ increasing with depth since the average path of an electron in the cavity increases with depth because of the increasing spread in angle of the electrons. Figure 2.8 shows the electron fluence spectra in the collecting volume of the chamber cavity, together with that in the water phantom. The curves for air and LDW match everywhere except at energies lower than 30 keV where there might be a 0.5-1% difference. This may explain point (1) listed above, i.e. a small fluence perturbation due to the difference in materials

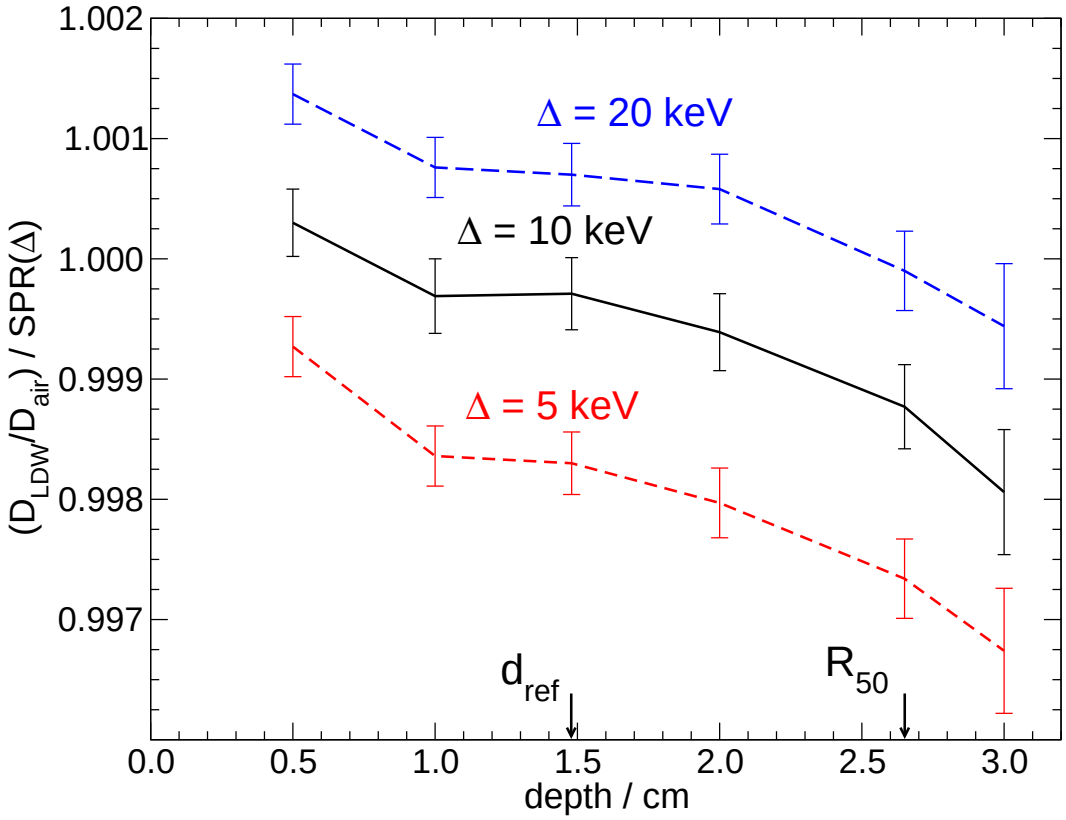

Figure 2.7: Ratio of the dose ratio (LDW to air) in the NACP02 chamber cavity to the restricted water/air SPR for different Δ's as a function of depth in the 6 MeV electron beam. From paper II.

leads to the slight decrease of the ratio with depth. Another notable thing in Figure 2.8 is that the spectrum in water differs from that in the cavity by approximately a constant ratio over almost the entire energy range.

Uncertainty of P_{repl} for the BIPM chamber in a ^{60}Co beam

At the "Bureau International des Poids et Mesures" (BIPM) in France, a graphite flat cavity ionization chamber is used to determine the absorbed dose to graphite in a ^{60}Co beam. This chamber (hereafter referred to as the 'BIPM chamber') is similar to a normal plane-parallel chamber except there is a circular collecting electrode made of graphite at the center of the cavity as shown in Figure 2.9. In the study of P_{repl} values for

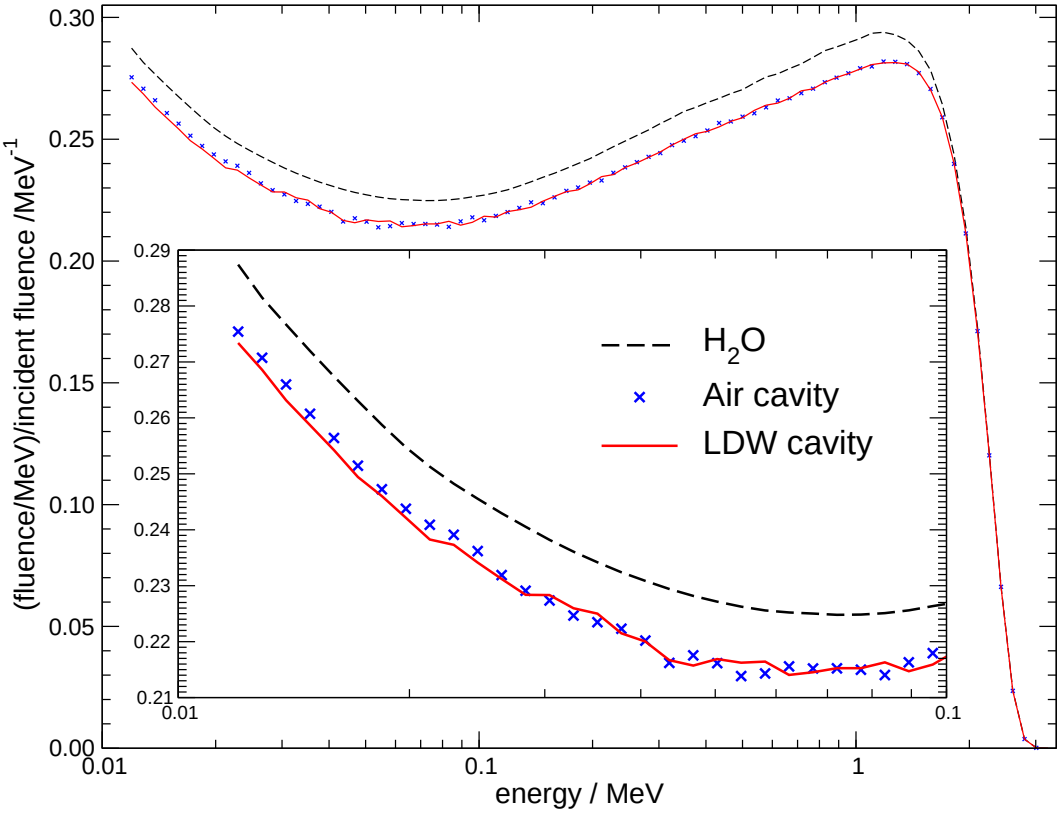

Figure 2.8: Electron fluence spectra in a water phantom and in the collecting volume of the NACP02 chamber cavity filled with either air or LDW. The calculation is at R_{50} in the 6 MeV electron beam. The inset shows the details of the curves from 10 keV to 100 keV. The calculation uncertainty is less than 0.4%. From paper II.

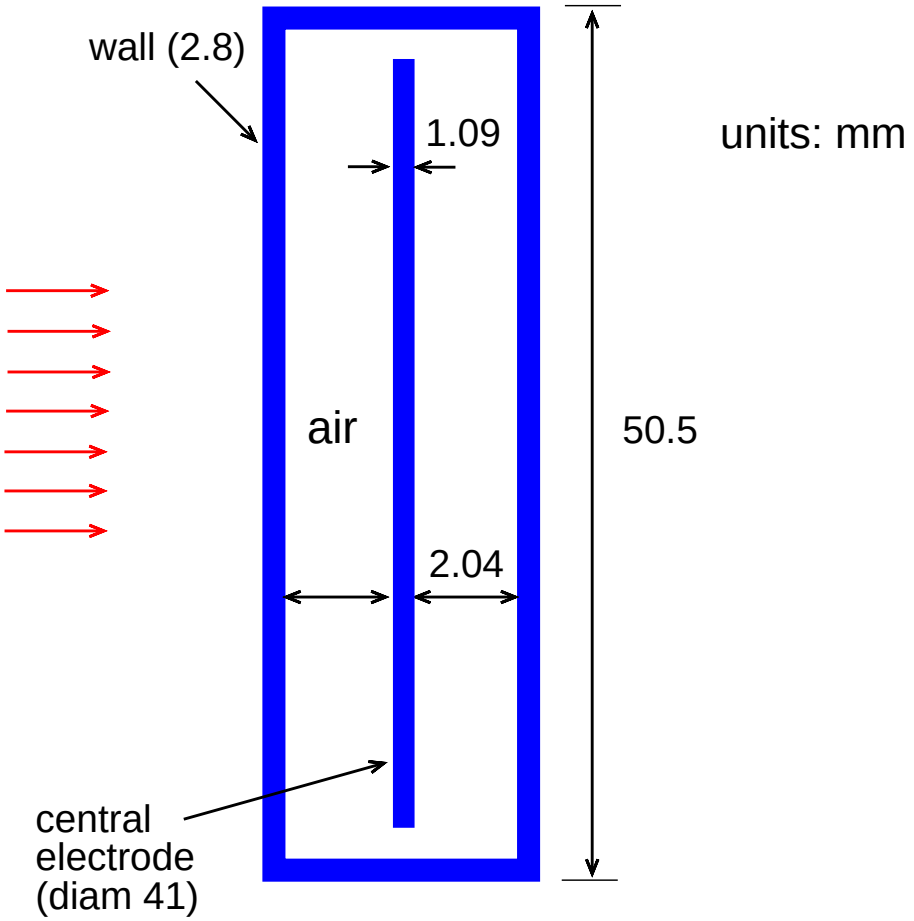

Figure 2.9: Schematic diagram of the BIPM chamber with a horizontal axis of symmetry. Geometrical data are from Boutillon.[43]

the BIPM chamber in a graphite phantom irradiated by a ^{60}Co beam (Section 3.2), the LDW method is used for all the P_{repl} calculations. The ratio of doses in the BIPM chamber cavity filled with low-density graphite (i.e. same density as air) to that filled with air at different depths is calculated and compared to the graphite/air SPR. All calculations are done here at AE = ECUT = 512 keV. Table 2.1 shows the results. The dose ratio is at most 0.2% different from the SPR which is evaluated at a cutoff energy of $\Delta = 14$ keV taken by Niatel et al.[44] Sin ce there is transient charged particle equilibrium in photon beams, it is unlikely the 0.1-0.2% discrepancy is coming from the electron fluence perturbation induced by replacing air with low-density graphite in the cavity. Rather, it is more likely an issue of selecting an appropriate Δ for the BIPM

chamber cavity. For instance, if one takes $\Delta = 30$ keV which is not unreasonable due to the large cavity size of the chamber, the dose ratio would be essentially the same as the SPR. The results in Table 2.1 suggest that the systematic uncertainty of calculating the $P_{\rm repl}$ values for the BIPM chamber is at most 0.2%.

Table 2.1: The ratio of dose in the BIPM chamber cavity filled with low-density graphite (LDG) to that filled with air at two depths in a graphite phantom in a ^{60}Co beam. The source-chamber distance is kept at 100 cm, and the field size at chamber is 10×10 cm^2. The graphite/air SPR $\left(\frac{\overline{L}_\Delta}{\rho}\right)_a^g$ is evaluated at $\Delta = 14$ keV. From paper V.

depth (g/cm^2)	$\frac{D_{LDG}}{D_{air}}$	$\left(\frac{\overline{L}_\Delta}{\rho}\right)_a^g$	$\frac{D_{LDG}}{D_{air}} / \left(\frac{\overline{L}_\Delta}{\rho}\right)_a^g$
4.0	1.0014±0.0008	1.00275±0.00007	0.9986±0.0008
15.0	1.0016±0.0008	1.00365±0.00008	0.9980±0.0008

Uncertainty of $P_{\rm repl}$ for thimble chambers in photon beams

A similar study is performed for cylindrical thimble chambers of length 2 cm with different radii at 5 cm depth in a water phantom irradiated by a ^{60}Co beam. Table 2.2 lists the quotients of the dose ratio and the water/air stopping-power ratio. When the cutoff energy $\Delta = 10$ keV is used for the stopping-power ratio evaluation for all the chambers, the quotient varies by 0.16% from 1 mm to 10 mm chamber. However, if the value of Δ characterizing each cavity size is used in the SPR evaluation, the quotients are essentially equal to unity for all chamber sizes. This demonstrates that the 0.16% variation when using a single Δ value for all chambers comes from the SPR variation with Δ, and there is in fact no change in the electron fluence perturbation for these chambers in photon beams when air is replaced by LDW. Thus the calculated values of $P_{\rm repl}^{LDW}$ are correct but must be used with SPRs using the correct value of Δ. As current dosimetry protocols use a single value of $\Delta = 10$ keV for all chambers used for

calibration, one way to account for this is to assume the calculation of P_{repl} values by the LDW method for commonly used thimble chambers has a systematic uncertainty of something less than 0.2%.

Table 2.2: The quotient of the dose ratio and the water/air SPR for cylindrical chambers of different radii at 5 cm depth in a water phantom in a ^{60}Co beam. The dose ratio is the ratio of dose in the chamber cavity filled with LDW to that filled with air. The mean chord length is calculated by Equation 1.6. Δ is found from Figure 2.5, after scaling density from air to HDA. In the first row, $\Delta = 10$ keV is used for the SPR evaluation for all the chambers. In the last row, the value of Δ characterizing each cavity size is used in the SPR evaluation. From paper V.

radius	1 mm	3 mm	10 mm
$\frac{D_{LDW}}{D_{air}} / \left(\frac{\overline{L}(\Delta=10\ keV)}{\rho}\right)_a^w$	0.9998±0.0008	0.9988±0.0009	0.9982±0.0008
mean chord length (mm)	1.9	5.2	13.3
Δ (keV)	9.6	16.2	28.1
$\frac{D_{LDW}}{D_{air}} / \left(\frac{\overline{L}_\Delta}{\rho}\right)_a^w$	0.9997±0.0008	0.9997±0.0009	1.0000±0.0008

From these results, the systematic uncertainty of calculating P_{repl} values by the LDW method is around 0.1-0.2%. For high-Z materials, it is expected the electron fluence perturbation is not negligible when replacing air by the low-density high-Z material. In addition, the rapid change of the stopping-power ratios with the cutoff energy Δ makes the uncertainty of calculating P_{repl} by the LDW method very large.

2.6 Influence of electron energy threshold and cutoff

EGSnrc is a class II Monte Carlo code for electron and photon transport[45] in which a secondary electron is explicitly simulated if the production energy is larger than a

threshold (AE). An electron's history is terminated if its energy falls below a cutoff energy (ECUT). The lower AE and ECUT are, the more accurate and also much longer the simulation is. As a 0.1% accuracy level is pursued, how AE and ECUT affect the calculation results should be investigated. To study this, the radiation dose in the cavity of the NACP02 chamber is calculated, for varying ECUT for both AE = 512 keV and AE = 521 keV, at a depth of R_{50} in a 6 MeV electron beam. Dose is also calculated at the respective points of measurement in the water phantom. Figure 2.10 shows the calculated relative doses in the cavity and in the phantom at depth R_{50}, in a 6 MeV beam for different AEs and ECUTs. This figure shows that: (1) for a given AE and with a statistical uncertainty of 0.1% or less, the cavity and the phantom doses are almost independent of ECUT, ranging from 1 keV to 100 keV; (2) for either case, the dose calculated with AE = 512 keV is about 0.5% lower than with AE = 521 keV. This difference in the calculated dose is due to the difference in energy-loss straggling for different production thresholds for creating secondary electrons. In the fall-off region of electron beam depth-dose curves the effect of energy-loss straggling is more pronounced because the electrons are nearing the end of their ranges. Calculated doses do not show much variation near the depth of maximum dose in the 6 MeV electron beam nor at a depth of 5 cm in a ^{60}Co photon beam. However, this energy-loss straggling effect is significant only if one is interested in absolute dose calculation. For a dose ratio calculation, such as P_{repl} in this work, the effect cancels as shown in Figure 2.11.

Similar results are obtained for both plane-parallel chambers and thimble chambers in either electron or photon beams, i.e. the calculated dose ratio is insensitive to the energy cutoff. Thus AE = ECUT = 521 keV is used throughout this work unless otherwise specified.

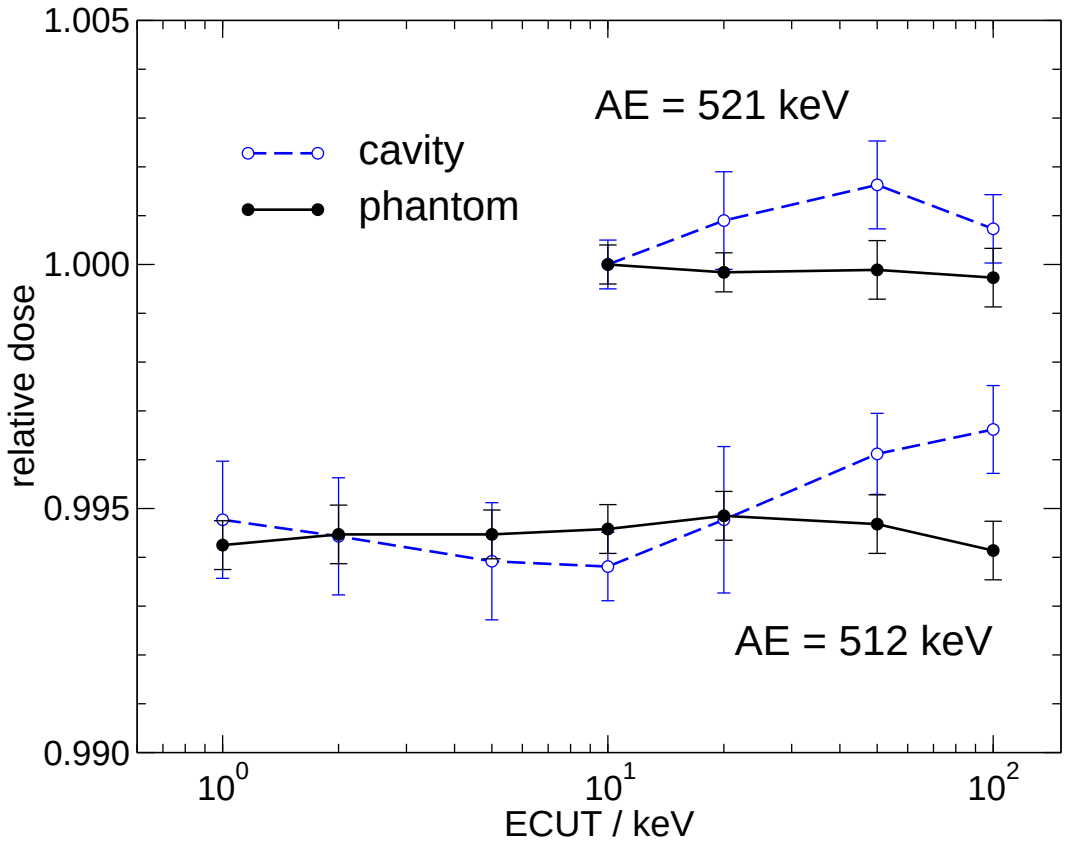

Figure 2.10: Relative doses as a function of ECUT in the NACP02 cavity and in the phantom at depth R_{50} in the 6 MeV electron beam, for two different AE values. The doses are separately normalized in the cavity and the phantom at AE=ECUT= 521 keV. From paper II.

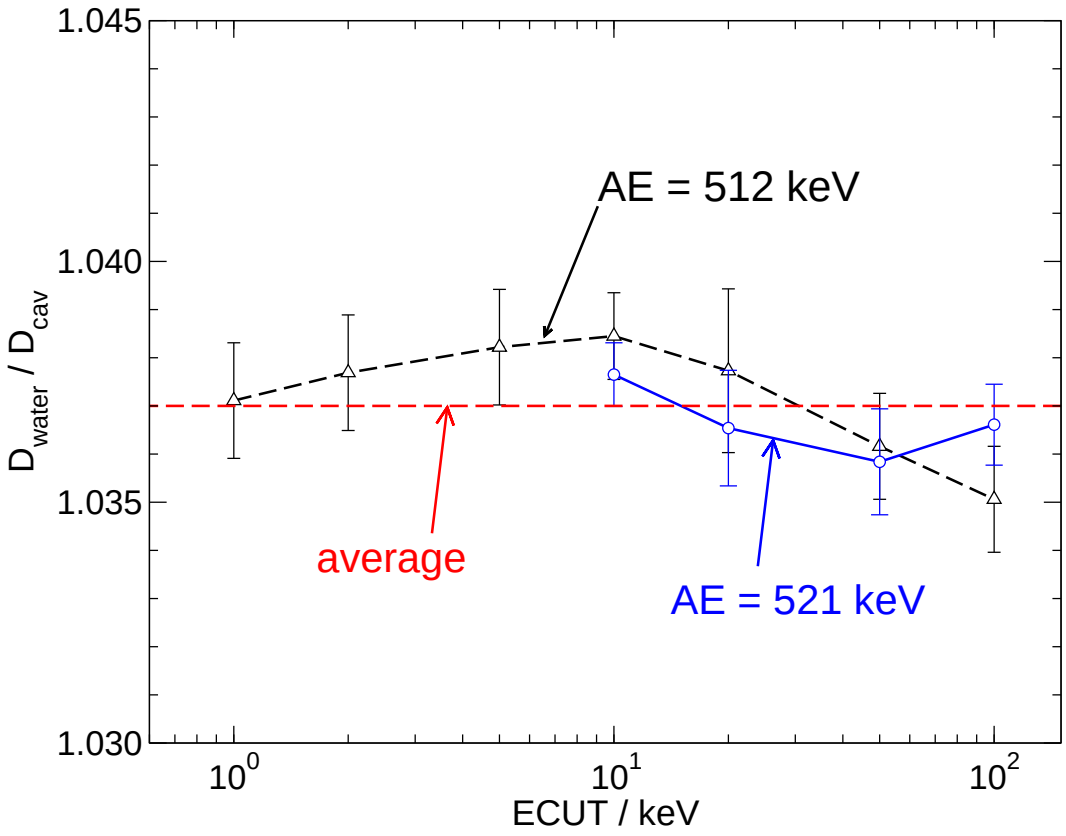

Figure 2.11: The ratio of the phantom dose to the cavity dose vs ECUT for two AE values for the same case as Figure 2.10. From paper II.

Table 2.3: Comparison of P_{repl} values by the four calculation methods for both the NACP02 and the Farmer chamber cavity at 5 cm depth in a ^{60}Co beam. From paper II.

	SPR	FLU	HDA	LDW
NACP02	1.0059±0.1%	1.0063±0.1%	1.0062±0.08%	1.0065±0.1%
Farmer	0.9963±0.08%	0.9952±0.08%	0.9969±0.09%	0.9974±0.07%

2.7 Comparison of the four methods

2.7.1 Calculated P_{repl} values in photon beams

The P_{repl} values calculated by the four methods for an NACP02 plane-parallel chamber and a Farmer-type cylindrical chamber at depth of 5 cm in a ^{60}Co beam are listed in Table 2.3. For the NACP02 chamber, all methods give the same result within calculation uncertainty and the results disagree with the assumption in dosimetry protocols by 0.6%. A calculation of the PDD curve for a ^{60}Co beam (SSD 80 cm, field size 10×10 cm^2) gives a dose gradient of about 0.6%/mm at 5 cm depth. Since the thickness of the air cavity is 2 mm, this suggests that the point of measurement for the NACP02 chamber in a ^{60}Co beam should be taken as the center of the air cavity of the chamber, as is done for these chambers in low and medium energy X-ray beams.[46] For the Farmer chamber, all methods give the same result within 0.2% although the values are significantly different from those used in dosimetry protocols. This issue is addressed in Section 4.2.

Table 2.4: Comparison of calculated P_{repl} values using four methods for the NACP02 chamber cavity at d_{ref} (close to d_{max}) in a 6 MeV, and at both d_{ref} and d_{max} in an 18 MeV electron beam. From paper II.

	SPR	FLU	HDA	LDW
6 MeV ($d_{ref} \approx d_{max}$)	0.9956±0.06%	0.9977±0.1%	0.9976±0.08%	0.9959±0.06%
18 MeV (d_{ref})	1.0001±0.06%	1.0007±0.06%	1.0011±0.07%	1.0005±0.05%
18 MeV (d_{max})	1.0004±0.07%	1.0015±0.06%	1.0012±0.06%	1.0010±0.07%

2.7.2 Calculated P_{repl} values in electron beams

NACP02 plane-parallel chamber

Table 2.4 lists P_{repl} values calculated by the four methods at d_{ref} and/or d_{max} in both a 6 MeV and an 18 MeV electron beam. The four methods all agree with the average within about 0.1%.

Farmer-type thimble chamber

Table 2.5 lists P_{repl} values calculated by the four methods at d_{ref} in both the 6 MeV and the 18 MeV electron beams. The most notable thing is that the LDW method, a direct method of calculating P_{repl}, gives a value which is 0.6% higher in the 6 MeV beam and 0.3% higher in the 18 MeV beam, than the other direct method (HDA). This seems to be inconsistent with the previous results in which all methods give the same values for cylindrical chambers in photon beams or for plane-parallel chambers in either type of beams. This apparent discrepancy is further investigated in Section 4.1.

Table 2.5: Comparison of calculated P_{repl} values using four methods for a Farmer chamber cavity centered at d_{ref} in a 6 MeV and in an 18 MeV electron beam. The uncertainties are statistical only. From paper VII.

	SPR	FLU	HDA	LDW
6 MeV	0.9604±0.04%	0.9627±0.04%	0.9618±0.07%	0.9674±0.04%
18 MeV	0.9832±0.07%	0.9841±0.12%	0.9829±0.07%	0.9858±0.07%

2.7.3 Computation time

All the calculations for this work were performed on a cluster with 48 nodes and each node has four 3 GHz Intel Woodcrest cores. Table 2.6 lists the approximate time in hours to calculate P_{repl} by different methods for an 18 MeV electron beam for both a spectrum source and a BEAMnrc simulation source. The time listed is the total CPU time needed to calculate P_{repl} to a precision of 0.1%. There is a big difference between using a spectrum source and a simulation source. This is because a linac simulation takes a lot of time to generate a useful particle and most of these particles are photons (about 78%) which do not contribute much dose in the cavity. The other option is to generate and use a phase-space file. However, to get a cavity dose with a precision of 0.1% for the 18 MeV simulation source, one needs at least 8 billion particles which corresponds to a phase-space size of about 240 GB. This is beyond the available capacity. The time listed for the simulation source is the longest possible time needed for the calculation since there is no particle re-use or recycling capability in the current implementation of the linac simulation source (SOURCE 23 in the code); so there is still room for efficiency improvement in the future. Other points that can be noted from Table 2.6 are that the CPU time using energy cutoff of 1 keV is much longer than using 10 keV, and the LDW method takes the least amount of time compared to other methods.

Table 2.6: Comparison of the CPU time on an Intel Woodcrest 3 GHz core needed to calculate P_{repl} with a statistical uncertainty of 0.1% by the four methods for the NACP02 chamber cavity at d_{max} in an 18 MeV electron beam when using a spectrum source or a beam simulation source. For the HDA method, both 10 keV and 1 keV energy cutoffs are used with HDA thickness of 1 μm and 3 μm, respectively. From paper II.

	CPU time required (hour)				
	SPR	FLU	HDA (10 keV, 1 μm)	HDA (1 keV, 3 μm)	LDW
spectrum source	50	90	50	240	36
simulation source	1600	-	4000	-	1500

Chapter 3

P_{repl} for plane-parallel ion chambers

3.1 P_{repl} values in electron beams

There were many experiments[47–52] done in the past to measure P_{repl} for some plane-parallel chambers in electron beams; but the results fluctuated as all the measurements had large (1∼2%) uncertainties. In current dosimetry protocols the P_{repl} values are assumed unity for all well-guarded plane-parallel chambers in electron beams. Verhaegen et al[34] and Buckley and Rogers[28] showed that this might not be true at least for the NACP02 chambers, although another study[35] suggested that the P_{repl} values are very close to 1 for Roos chambers at the reference depth for all electron beam energies. In this section, the values of P_{repl} for plane-parallel chambers in electron beams are calculated with the methods described in Chapter 2.

3.1.1 P_{repl} as a function of depth

Figure 3.1 shows P_{repl} values calculated by the four methods for the NACP02 chamber as a function of depth in the 6 MeV electron beam. It is seen that all the methods (except HDA with 0.6 mm slab thickness) give the same values within the statistical uncertainty.

Ma and Nahum[33] calculated the P_{repl} values with the EGS4 code using a monoenergetic 6 MeV electron beam and an HDA thickness of 0.6 mm, with a calculation uncertainty of 0.3%. The results for the 0.6 mm HDA calculation in this study agree with theirs within statistics. This figure makes clear that using an HDA thickness of 0.6 mm causes a systematic error of more than 0.5%, consistent with what is expected from the results of Figure 2.2.

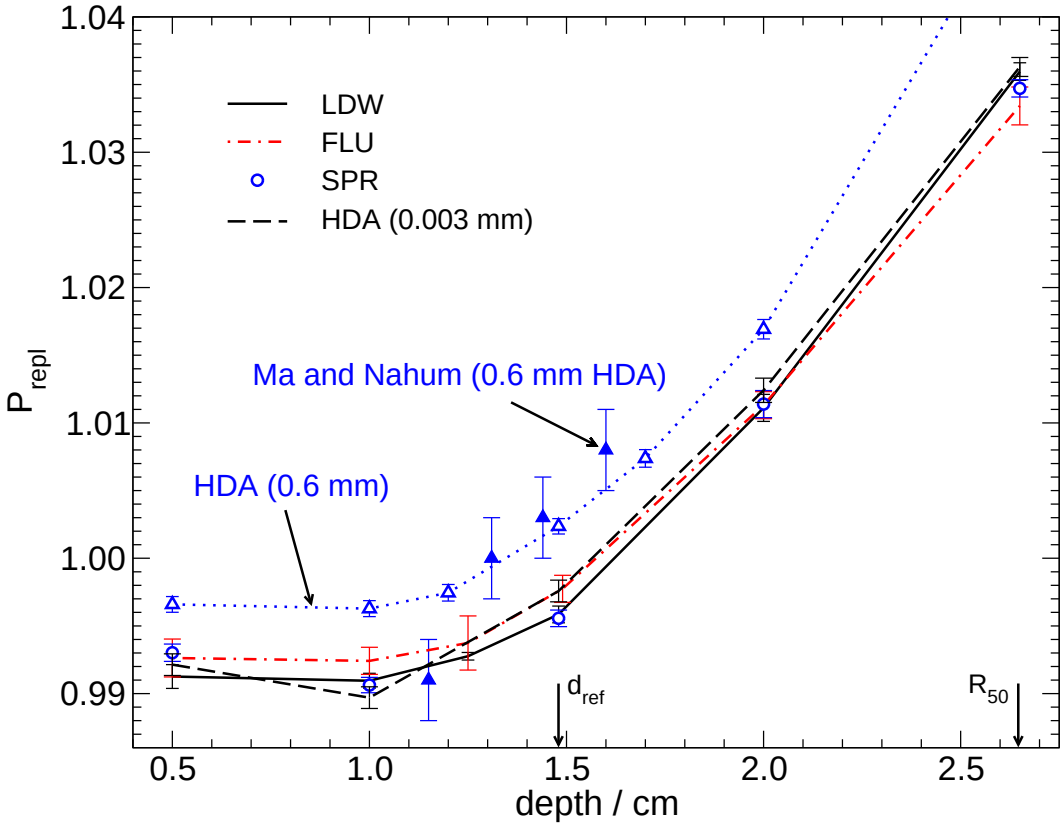

Figure 3.1: P_{repl} values calculated by the four methods for the cavity of an NACP02 chamber as a function of depth in the 6 MeV electron beam. For the HDA method, the calculation is done for two HDA slab thicknesses, 0.6 mm (open triangle) and 3 μm (dashed line). Solid triangles were calculated with EGS4 by Ma and Nahum,[33] for an HDA thickness of 0.6 mm. From paper II.

Figure 3.1 shows that at d_{ref} (which is basically d_{max} for this beam) P_{repl} is close, but not exactly equal, to unity for the well-guarded NACP02 chamber. The

deviation is about 0.4%. At depths closer to the phantom surface, P_{repl} is even farther away from unity. The less-than-unity value of P_{repl} at depths less than just past d_{ref} partly compensates the greater-than-unity wall correction P_{wall} found for this chamber,[28] although past this depth both P_{wall} and P_{repl} are greater than unity. Figure 3.2 shows three sets of calculated P_{repl} values for the NACP02 chamber in an 18 MeV electron beam. Again, good agreement between the LDW method and the SPR method at different depths is obtained. It is notable that for this higher energy electron beam P_{repl} is essentially unity from the phantom's surface to a depth beyond d_{ref}. Also shown are the results calculated by Verhaegen *et al.*[34] with the SPR method for a Clinac 2300 (digitized from Figure 6 in their paper). There is a significant discrepancy at some depths, especially at d_{ref}. Verhaegen *et al.* used a phase-space file as the radiation source as opposed to the spectrum source in this work. To find out if this causes any differences, a BEAMnrc linac simulation of the 18 MeV electron beam is used as the radiation source, as well as a spectrum source extracted from the 18 MeV electron beam modeling. The values of P_{repl} at d_{ref} and d_{max} are calculated by the SPR, the HDA, and the LDW methods. The results show that the P_{repl} value calculated using the linac model agrees with that for a spectrum source within the calculation uncertainty of 0.1%. A similar calculation with a 22 MeV electron beam gives the same result. These results show that the high level of photon contamination, which is the major difference between a spectrum source and a simulation source, has little effect on the P_{repl} calculation.

Figure 3.3 shows P_{repl} values calculated for several typical plane-parallel chambers (all are well-guarded except Markus) in the 6 MeV electron beam. The Markus chamber shows a larger perturbation effect than others due to its small guard width (see Table 1.1).

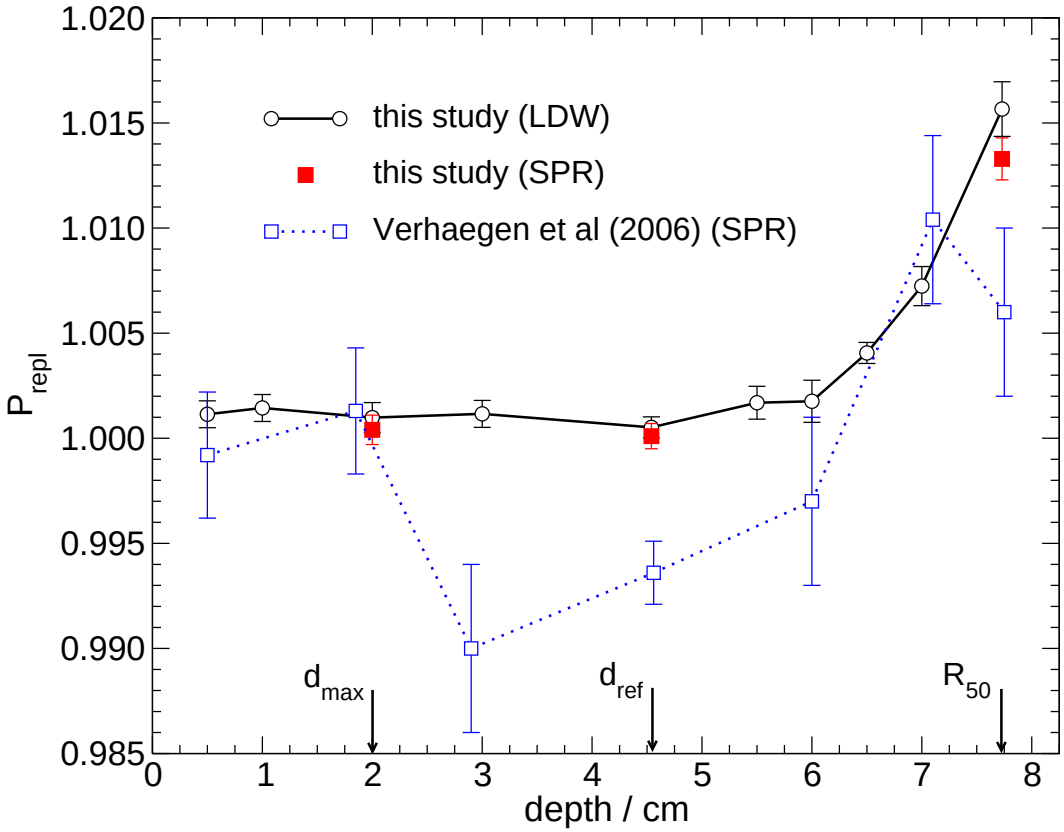

Figure 3.2: P_{repl} values for the NACP02 chamber cavity as a function of depth in an 18 MeV electron beam. Open circles are the results for the LDW method and solid squares for the SPR method. Open squares are the results calculated by Verhaegen *et al.*[34] with the SPR method for a Clinac 2300 beam with the same energy and the same R_{50} = 7.73 cm as the Clinac 2100 model in this study. From paper II.

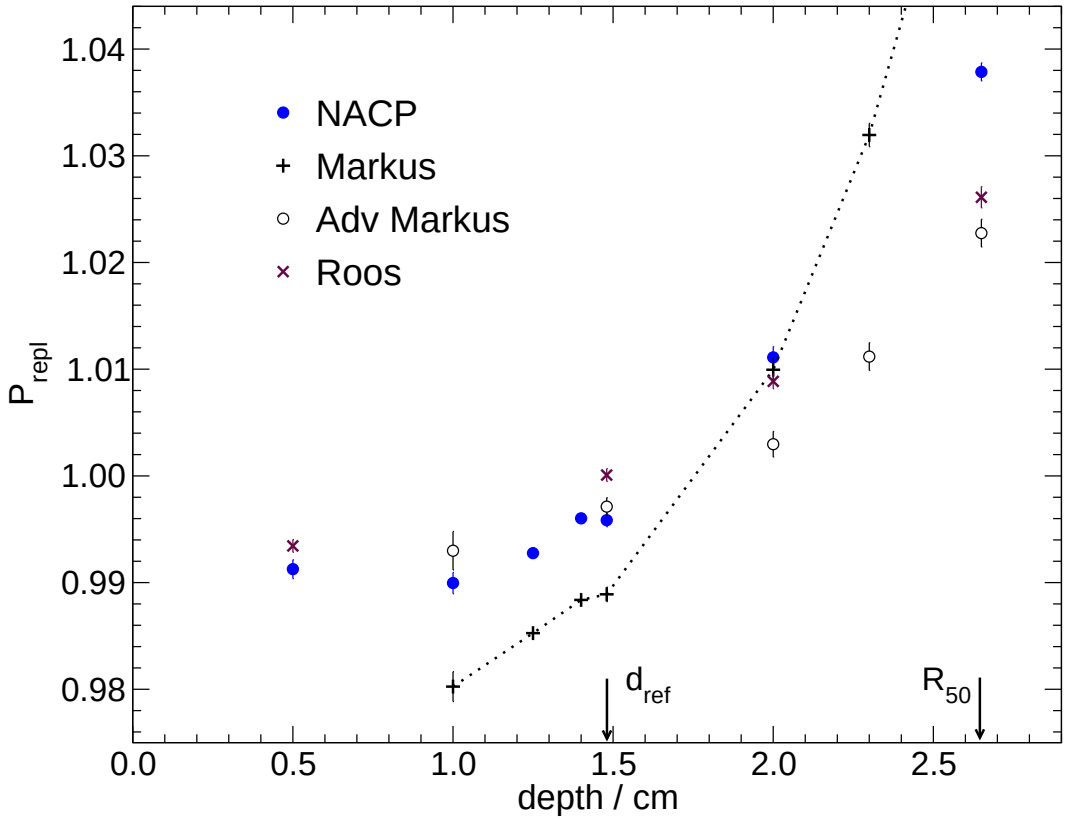

Figure 3.3: P_{repl} values of plane-parallel chambers as a function of depth in a 6 MeV electron beam. The calculations are done by the LDW method.

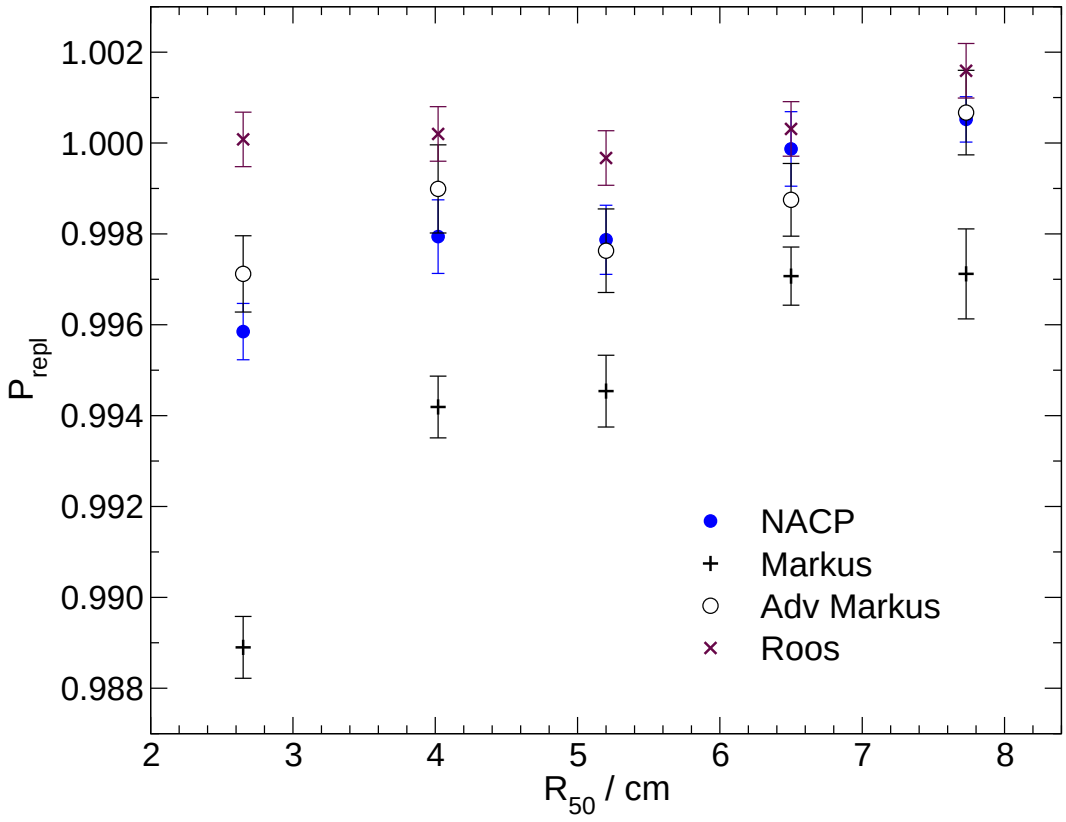

Figure 3.4: Beam quality dependence of P_{repl} values at d_{ref} for a few plane-parallel chambers in electron beams.

3.1.2 Beam quality dependence of P_{repl}

Figure 3.4 shows the beam quality dependence of the P_{repl} values for the plane-parallel chambers in electron beams. The Markus chamber shows a larger variation of the P_{repl} values than well-guarded chambers. The Roos chamber has values of P_{repl} very close to 1 for all electron beams, which is consistent with another study.[35]

3.1.3 Comparison to measurements

Experimentally it is hard to separate P_{repl} from P_{wall}, so usually their product, or the perturbation factor, $P = P_{\text{wall}}P_{\text{repl}}$, is measured. Ding and Cygler[51] did experiments to determine the perturbation factor of a Markus chamber at d_{ref} in a water phantom in various electron beams by comparing its readings to an NACP02 chamber. Both the Markus chamber and the NACP02 chamber were cross-calibrated to a cylindrical chamber at d_{max} in a 20 MeV high-energy electron beam. To compare to the experimental data, the perturbation factors for both the Markus and the NACP02 chambers are calculated at d_{ref} in various electron beams from 6 MeV to 22 MeV, and at d_{max} in a 22 MeV high-energy electron beam. Assuming $P_N(Q,z) = [P_{\text{wall}}(Q,z)P_{\text{repl}}(Q,z)]^{\text{NACP}}$ is the perturbation factor for the NACP02 chamber at depth z in a beam of quality Q, and $P_M(Q,z) = [P_{\text{wall}}(Q,z)P_{\text{repl}}(Q,z)]^{\text{Markus}}$ is the perturbation factor for the Markus chamber, and using a derivation similar to that of Ding and Cygler[51] which starts from Equation 1.9, the following relationship between the perturbation factors and the chamber readings M can be obtained

$$\frac{P_M(Q,d_{ref})P_N(22,d_{max})}{P_N(Q,d_{ref})P_M(22,d_{max})} = \frac{M_N(Q,d_{ref})M_M(22,d_{max})}{M_M(Q,d_{ref})M_N(22,d_{max})}, \tag{3.1}$$

where M_N and M_M are chamber readings for the NACP02 and the Markus chambers, respectively. In the experiment, P_N was assumed to be 1 in all the electron beams, and P_M was assumed to be 1 at d_{max} in the 20 MeV beam (in the calculation it is 22 MeV).

Thus Equation 3.1 can be used to determine $P_M(Q, d_{ref})$ from chamber readings and their measured value of $P_M(Q, d_{ref})$ is the right-hand side of Equation 3.1. Figure 3.5

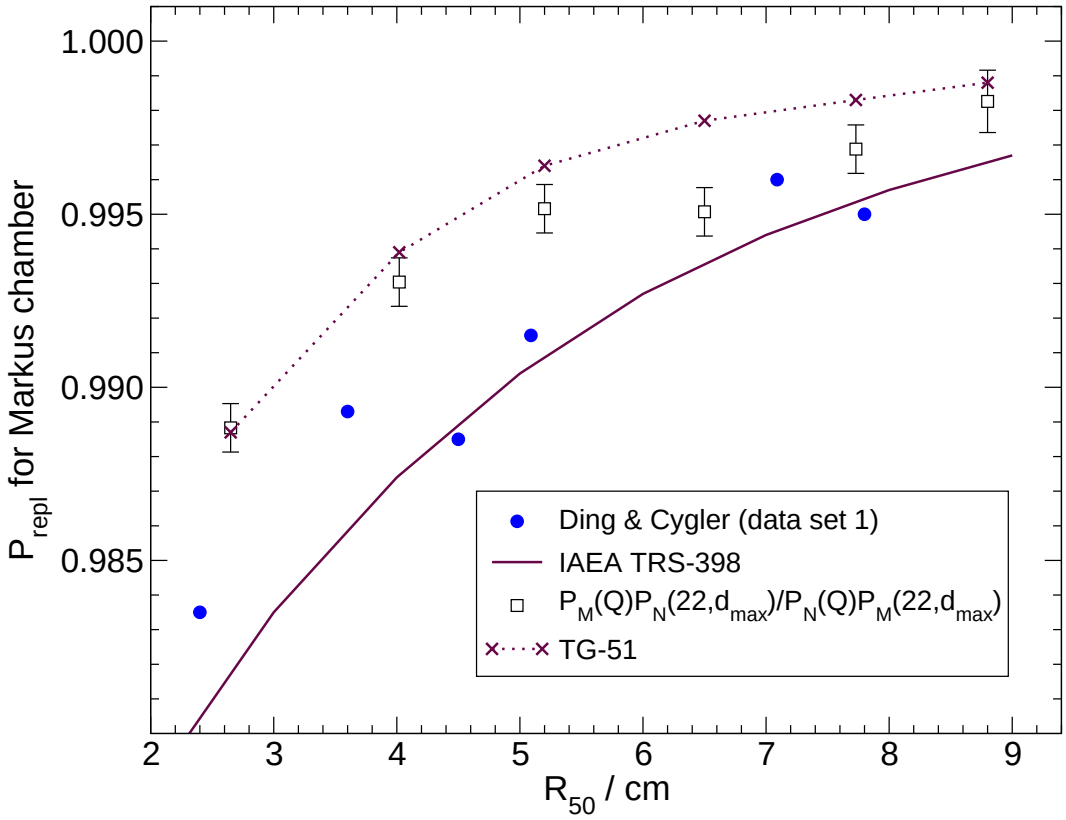

Figure 3.5: The calculated ratio of the perturbation factors at d_{ref} for a Markus chamber in electron beams compared to an experimental determination of the P_{repl} values for the Markus chamber by Ding and Cygler.[51] The IAEA and TG-51 data are recast from many experimental determinations of the P_{repl} value of the Markus chamber.

compares the measurements to the calculated quantity on the left-hand side of Equation 3.1. The calculations are done by the LDW method. It is seen the agreement is very good (within 0.5%), keeping in mind that the systematic uncertainty of the LDW method is around 0.1-0.2% and the measurement reproducibility is up to 0.5%.[51]

3.2 P_{repl} values for the BIPM chamber in ^{60}Co beam

3.2.1 The BIPM chamber and the value of W/e

The BIPM chamber (Figure 2.9) played a central role in the determination of the value of the product of W/e, which is introduced in Equation 1.7, and $\left(\frac{\overline{L}_{\Delta}}{\rho}\right)_a^C$, the mean restricted mass collision stopping-power ratio for graphite to air in a ^{60}Co beam. Many experiments[6,53] have been performed in the past to determine W/e. For low-energy electrons (up to 7 keV), W/e can be measured directly.[53] For high-energy photon beams, e.g. ^{60}Co and linac beams, direct measurement of W/e becomes impossible as the range of electrons is too large. Instead, cavity theory has to be employed in determining W/e, and in fact, only the product $(W/e)\left(\frac{\overline{L}_{\Delta}}{\rho}\right)_a^C$ can be directly measured. The value of W/e can then be derived if one knows the value of $\left(\frac{\overline{L}_{\Delta}}{\rho}\right)_a^C$. Two important experiments measuring the product $(W/e)\left(\frac{\overline{L}_{\Delta}}{\rho}\right)_a^C$ were performed by Niatel et al,[44] and the W/e value obtained from the measurements carries a significant weight in determining the standard value of 33.97±0.05 J/C recommended by Boutillon and Perroche-Roux[6] and adopted by convention by all primary standard labs. Niatel et al used two independent ways[44] to determine $(W/e)\left(\frac{\overline{L}_{\Delta}}{\rho}\right)_a^C$. In the first method, they compared the ionometric readings from the BIPM chamber to the calorimetric standards from four national laboratories for the absorbed dose in graphite irradiated by a ^{60}Co beam. The W/e value thus determined is 33.96±0.08 J/C when using ICRU Report 37[54] stopping powers to evaluate $\left(\frac{\overline{L}_{\Delta}}{\rho}\right)_a^C$. This value was later revised to 33.99±0.08 J/C by Boutillon,[55] after taking into account the radial non-uniformity effect[56] for the ^{60}Co beam and the gap correction[57] for the calorimeters (both of which were ignored in the original four comparisons), and also after considering the measurements with three more absorbed dose calorimeters. In the second method, they measured the exposure rate for a ^{60}Co source of known activity

and compared this to the calculated exposure rate to obtain a value of 33.81±0.42% J/C for W/e. Again, the ICRU Report 37 stopping powers were used to evaluate $\left(\frac{\overline{L}_\Delta}{\rho}\right)_a^C$. As the electron stopping power in a medium depends on the mean excitation energy (or I-value) of the medium, so does the stopping-power ratio $\left(\frac{\overline{L}_\Delta}{\rho}\right)_a^C$ and hence the value of W/e. Currently ICRU Report 37 uses an I-value of 78±7 eV (2σ) for graphite.[54] A newer experiment[58] has given an I-value of 86.8±1.2 eV for graphite with a much reduced uncertainty. If this new I-value is used in evaluating the stopping power, the stopping-power ratio $\left(\frac{\overline{L}_\Delta}{\rho}\right)_a^C$ in a ^{60}Co beam would be decreased by 1.6%. Consequently, the value of W/e obtained above should be increased by the same amount. However this is an extreme case since the original ICRU value was based on 4 previous experiments, several with much smaller uncertainties than the evaluated value of 78±7 eV. Taking a weighted average of all 5 experiments gives I = 84.5±5 eV (2σ) although the two extreme cases (78 and 86.8 eV) are used in this work.

In order to use the BIPM chamber to determine accurately the absorbed dose to graphite in a ^{60}Co beam, among other things, the perturbation effect caused by the chamber must be reliably determined. Since the chamber is used in a graphite phantom, the only perturbation correction factor related to this chamber is $P_{\rm repl}$ (or $K_{\rm p}$ as denoted by Niatel et al). The equation Niatel et al used in their determination of the value of $(W/e)\left(\frac{\overline{L}_\Delta}{\rho}\right)_a^C$ is:[44]

$$(W/e)\left(\frac{\overline{L}_\Delta}{\rho}\right)_a^C = \frac{\dot{D}_{cal}}{J \times P_{\rm repl}}, \tag{3.2}$$

where J is the ionization current collected per unit mass of air in the cavity. $\dot{D}_{cal}$ is the dose rate measured by calorimetry. As the $P_{\rm repl}$ value for the BIPM chamber is directly related to the determination of W/e, accurate knowledge of the value becomes very important. Boutillon[43] used an analytical approach to calculate the $P_{\rm repl}$ value for the BIPM chamber at different depths in a graphite phantom irradiated by a ^{60}Co beam. For situations in which either the front face or the center of the cavity was taken as the point of measurement (POM), the values of $P_{\rm repl}$ were found to be 1.007 and

0.989, respectively, at a depth of 5 g/cm^2. Ferreira et al[59] used the EGS4 Monte Carlo code to calculate the P_{repl} value for the same chamber and found the same results as Boutillon. Niatel's experimental results[60] were consistent with Boutillon's calculations, although only the ratio of P_{repl} values as a function of depth for the two POMs was verified. However, Boutillon stated that the P_{repl} values for the BIPM chamber were calculated "by applying the same type of analysis as that used ... for the determination of exposure",[43] by which she meant as used for the calculation of the correction for axial non-uniformity needed for the exposure standard. It was pointed out in the early 90s that this method was incorrect[61] and, in a recent paper, Burns[62] showed that this particular correction factor was incorrect by 0.63%, and the new value is used in the BIPM primary standard for air kerma (exposure).[63] This suggests that a re-evaluation of the P_{repl} values for the BIPM chamber is appropriate.

In Chapter 2, systematic and reliable ways of calculating P_{repl} in photon beams by Monte Carlo methods have been established. One of the conclusions from that study is that, for plane-parallel chambers in photon beams, P_{repl} is unity if the mid-plane of the chamber cavity is taken as the point of measurement. This seems to contradict the P_{repl} value (0.989) given above for the BIPM chamber when the center of the cavity is taken as the point of measurement. Additionally, the limitations of the EGS4 code with the PRESTA[31] algorithm in calculating ion chamber responses in a ^{60}Co beam were pointed out years ago[64] when it was shown that there is about a 1 percent systematic error in the calculation results for a graphite ion chamber. With the techniques described in Chapter 2, the P_{repl} values for the BIPM chamber are calculated in a graphite phantom irradiated by a ^{60}Co beam.

3.2.2 Default EGSnrc calculation of P_{repl}

The chamber and the ^{60}Co source geometries are the same as those described by Ferreira et al[59] and Boutillon.[43] A mono-energetic photon beam of energy 1.25 MeV was also used in the calculation to study the sensitivity of the calculated P_{repl} values to the radiation spectrum. The graphite phantom and the BIPM chamber wall have a density of 1.80 g/cm^3. Since the density of graphite varies, a graphite phantom of density 1.70 g/cm^3 is also used in the calculations to study if there is any dependence on the phantom density. The electron stopping-power density correction for the bulk graphite density (1.70 g/cm^3) is used in most of the calculations with standard ICRU Report 37 stopping powers. The density correction for the grain (or crystallite) density (2.26 g/cm^3) together with a graphite stopping power calculated from the extreme I-value of 86.8 eV is also used in the calculation for a sensitivity test. The boundary crossing and electron transport algorithm are EXACT and PRESTA-II, respectively. Electron energy thresholds (AE) and cut-offs (ECUT) of both 10 and 1 keV (kinetic energy) are used (i.e. either AE = ECUT = 10 keV or AE = ECUT = 1 keV), and the same values are used for the corresponding photon thresholds (AP and PCUT). The graphite/air stopping-power ratio is calculated with a cutoff energy of 14 keV for the BIPM chamber. This cutoff energy is the minimum energy needed on average for an electron to cross the cavity as determined by Niatel et al.[44] A low-density graphite material (1.2048×10^{-3} g/cm^3) is created in order to use the LDW method described in Chapter 2.

Tables 3.1 and 3.2 list P_{repl} values for the BIPM chamber calculated by different methods and for different scenarios in order to assess the sensitivity of the calculated values to these parameters. Both the SPR and the LDW methods give the same result within calculation statistical uncertainties ($\sim$0.1%), except for the mono-energetic photon beam. In this extreme case the value is about 0.3% lower, though barely of statis-

tical significance. It is assumed therefore that the possible difference between the Mora spectrum and the BIPM spectrum has a negligible effect on the calculated P_{repl} values. These results also demonstrate that using 10 keV as the energy cutoff is sufficient for this chamber. However, as discussed below, the results are significantly different (about 1%) from the Ferreira et al[59] values calculated using EGS4/PRESTA.

Table 3.1: Comparison of P_{repl} values calculated by different methods for the BIPM chamber at depth of 4 g/cm^2 in a graphite phantom when the front face of the cavity is taken as the point of measurement. Two methods, SPR and LDW are used with different particle energy thresholds and cut-offs. ECUT (PCUT) is the same as AE (AP) in all cases. AE is expressed as kinetic energy. From paper III.

	SPR (Δ = 14 keV)	LDW
AE = AP = 1 keV	1.0171±0.0012	1.0176±0.0012
AE = AP = 10 keV	1.0165±0.0009	1.0181±0.0008

Table 3.2: Comparison of P_{repl} values calculated for different scenarios for the same geometry as described in Table 3.1. Electron and photon cut-offs are AE = AP = 10 keV. AE is expressed as kinetic energy. The LDW method is used in the calculations. From paper III.

	1.80 g/cm^3 phantom, spectrum source	1.70 g/cm^3 phantom, spectrum source	1.80 g/cm^3 phantom, 1.25 MeV photons
P_{repl}	1.0181±0.0008	1.0169±0.0012	1.0148±0.0012

3.2.3 EGS4 calculation mimicked by EGSnrc code

In order to investigate the cause of this discrepancy with the EGS4 results, the CAVRZnrc code was used to mimic the old EGS4/PRESTA calculations.[16] In doing so, the boundary crossing and electron transport algorithm are both set to PRESTA-I. The maximum step size (SMAX) is 5 cm. The maximum energy loss per step (ESTEPE) is 0.04, corresponding to the value used by Ferreira et al.[59] Electron and photon energy thresholds/cut-offs are 512 keV (or 1 keV in kinetic energy) and 1 keV, respectively. The skin-depth for boundary crossing, which was not reported by Ferreira et al,[59] is set to a variety of values to check the dependence of the calculated chamber response. Figure 3.6 shows the values of $P_{\rm repl}$ for this 'EGS4-mimic' calculation as a function of the value of the skin-depth parameter. The variation of the calculated $P_{\rm repl}$ values can be as large as 3%; and it covers both the result by Ferreira et al and the result in this work by the default EGSnrc calculation. The default EGS4 skin-depth is about 7.7. At this point, $P_{\rm repl}$ is about 1.012, half a percent higher than the value given by Ferreira et al. This difference is probably because the 'EGS4-mimic' calculation is not a true EGS4 calculation and there are still other variable parameters. The results in Figure 3.6 demonstrate that EGS4/PRESTA is not reliable in calculating the ion chamber responses. In EGSnrc, the calculation of ion chamber response is essentially independent of either skin-depth or ESTEPE.[20]

3.2.4 $P_{\rm repl}$ for BIPM chamber

Figure 3.7 compares $P_{\rm repl}$ values for the BIPM chamber calculated in this study to those calculated by Boutillon[43] and by Ferreira et al[59] at various depths in a graphite phantom irradiated by a ^{60}Co beam. The values of $P_{\rm repl}$ are obtained for two cases: $P_{\rm repl,f}$ for the front face as the point of measurement (POM), and $P_{\rm repl,m}$ for the mid-plane as the

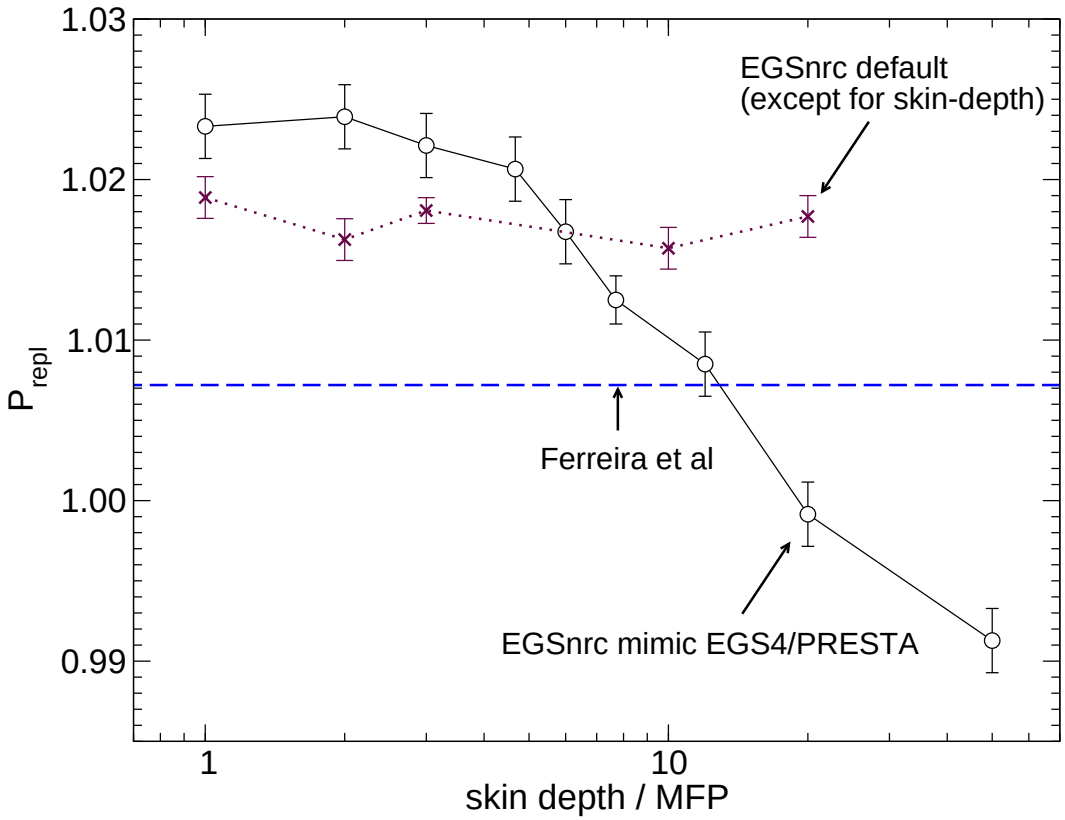

Figure 3.6: Calculated P_{repl} for the BIPM chamber by the default EGSnrc calculation and by using EGSnrc to mimic the EGS4/PRESTA algorithm. P_{repl} is calculated by the SPR method and is shown as a function of the skin-depth in mean free paths for boundary crossing. The horizontal dashed line indicates the EGS4 calculation by Ferreira et al,[59] with an unknown skin-depth parameter. The default EGS4 skin-depth is indicated by an arrow to the dashed line. The calculation is done at a depth of 4 g/cm^2 in a graphite phantom when the front face of the cavity is taken as the point of measurement. From paper III.

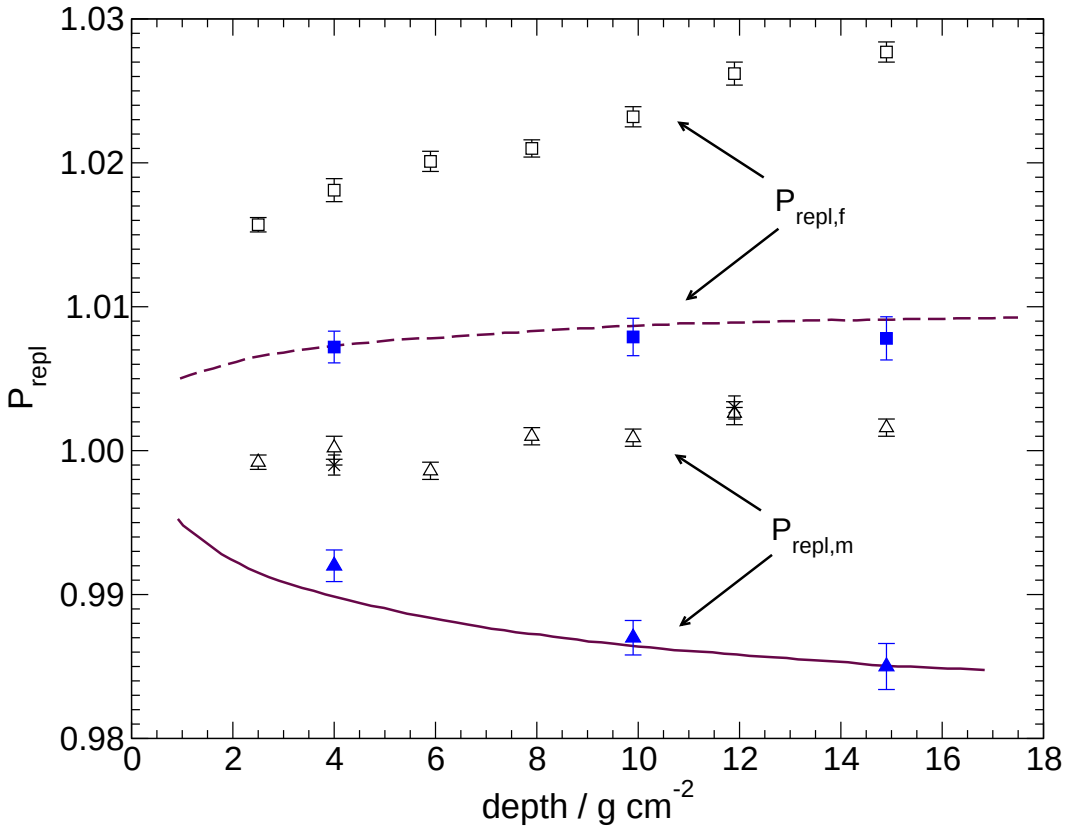

Figure 3.7: Calculated P_{repl} values (open symbols) for the BIPM chamber at various depths in a graphite phantom with either the front face ($P_{\mathrm{repl,f}}$) or the mid-plane ($P_{\mathrm{repl,m}}$) of the cavity taken as the point of measurement. The values from Boutillon[43] and from Ferreira et al[59] are shown as lines and solid symbols, respectively. The star symbols represent the $P_{\mathrm{repl,m}}$ values for a graphite phantom using grain density correction (2.26 g/cm^3) and an I-value of 86.8 eV for the stopping power. From paper III.

POM. In both cases the calculated P_{repl} values in this study are about 1% larger than the corresponding values by Boutillon and Ferreira et al, irrespective of the depth. The other distinction is that the $P_{\text{repl,f}}$ values in this study increase slightly with depth while $P_{\text{repl,m}}$ values remain close to unity, in contrast to the results of Boutillon and of Ferreira et al in which $P_{\text{repl,f}}$ does not depend much upon the depth but $P_{\text{repl,m}}$ decreases slightly with depth. Note that the results here for $P_{\text{repl,m}}$ are consistent with the result for another plane-parallel chamber (NACP02) in a ^{60}Co beam (see Section 2.7), where it was found that the POM should be at the center of the cavity instead of the front face in order to have $P_{\text{repl}} = 1$.

To investigate the sensitivity of the calculated P_{repl} values to the stopping powers used, the values of $P_{\text{repl,m}}$ are also calculated for a graphite phantom of density 1.80 g/cm^3 but with the density correction for the grain density (2.26 g/cm^3), together with the graphite stopping power calculated from the I-value of 86.8 eV. Figure 3.7 shows that the values of $P_{\text{repl,m}}$ for this graphite phantom are the same as $P_{\text{repl,m}}$ for the normal graphite phantom which uses the bulk density correction (1.70 g/cm^3) and the ICRU Report 37 stopping powers. These results demonstrate that the $P_{\text{repl,m}}$ value is not sensitive to the density correction or the I-value used.

Although there is about a 1% difference in the values of P_{repl} calculated in this work compared to the old values for the two POMs, the ratio of the two factors, $P_{\text{repl,f}}/P_{\text{repl,m}}$, is almost the same as before, as shown in Figure 3.8. The measurement made by Niatel[60] was considered to be experimental support of Boutillon's[43] calculations. However, as mentioned earlier, the experiment measured only the ratio of $P_{\text{repl,f}}$ to $P_{\text{repl,m}}$. In this sense, the P_{repl} values calculated in this work are also supported by the experiment.

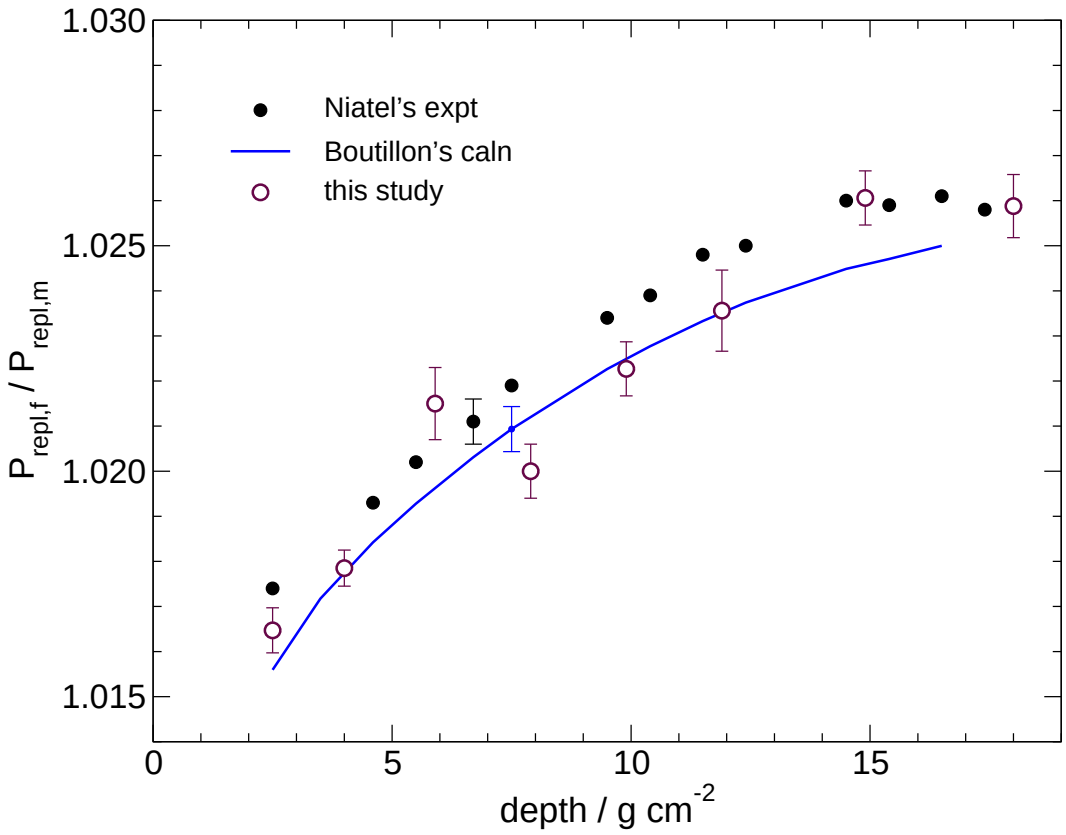

Figure 3.8: Calculated ratio $P_{\mathrm{repl,f}}/P_{\mathrm{repl,m}}$ (open circles) for the BIPM chamber at various depths compared with the experimental values (filled circles) and the analytical calculation by Boutillon (solid line). Both the measurement and the analytical calculation have an uncertainty of about 0.05% (1σ).[60] From paper III.

3.2.5 Values of $(W/e)\left(\frac{\overline{L}_\Delta}{\rho}\right)_a^C$ and W/e

The first method Niatel et al[44] used to determine the value of $(W/e)\left(\frac{\overline{L}_\Delta}{\rho}\right)_a^C$ was to compare the measured absorbed dose to graphite at various depths irradiated in a ^{60}Co beam by the BIPM chamber to that measured from the calorimetric standards of four national standards laboratories. The value of $(W/e)\left(\frac{\overline{L}_\Delta}{\rho}\right)_a^C$ is inversely proportional to the perturbation correction factor, P_{repl}, of the BIPM chamber[44] as given in Equation 3.2 (page 52). Thus the measured product $(W/e)\left(\frac{\overline{L}_\Delta}{\rho}\right)_a^C$ depends upon the accuracy of the P_{repl} values used for the BIPM chamber. As stated earlier, there is about a 1% difference between the P_{repl} values used previously for the BIPM chamber and those calculated in this study. The values of P_{repl} for the BIPM chamber were later revised by Boutillon,[55] but the change was not more than 0.07% and thus is insignificant. Hence this 1% difference would lead to a different value of the measured product $(W/e)\left(\frac{\overline{L}_\Delta}{\rho}\right)_a^C$ determined using the BIPM chamber. As shown earlier, the values of P_{repl} in this study for the BIPM chamber, when the mid-plane is taken as the POM, are very close to unity at different depths (see Figure 3.7), so it is a good approximation to assume it is 1.000. Thus the quantity $(W/e)\left(\frac{\overline{L}_\Delta}{\rho}\right)_a^C$ associated with the new P_{repl} values from this study can be obtained by multiplying the old $(W/e)\left(\frac{\overline{L}_\Delta}{\rho}\right)_a^C$ value at each depth by the correction factor P_{repl} calculated by Boutillon[55] at that depth. The value of W/e can be obtained by dividing the measured product $(W/e)\left(\frac{\overline{L}_\Delta}{\rho}\right)_a^C$ by $\left(\frac{\overline{L}_\Delta}{\rho}\right)_a^C$. Niatel et al evaluated the values of $\left(\frac{\overline{L}_\Delta}{\rho}\right)_a^C$ as a function of depth in the graphite phantom. They used stopping powers from ICRU Report 37[54] with an energy threshold $\Delta = 14$ keV. Their results are shown in Figure 3.9 along with the values obtained in this study for the same quantity. There is excellent agreement between the values calculated by Niatel et al and the values calculated by SPRRZnrc in this work. Figure 3.10 shows the revised values of W/e by Boutillon[55] for the original four comparisons (30 points) by Niatel et al,[44] taking into account the adjustments of the gap correction, the radial non-uniformity correction,

and P_{repl}. The stopping-power ratios in Figure 3.9 have been used to evaluate $\left(\frac{\overline{L}_{\Delta}}{\rho}\right)_a^C$ in order to obtain W/e. The average value of W/e from Boutillon's revision (dashed line) of the original four comparisons is 34.01 J/C, very close to the value of 33.99 J/C obtained[55] when additional three comparisons were taken into account. Figure 3.10 also presents the values of W/e determined in this study based on Boutillon's revision of the original data but assuming $P_{\text{repl}} = 1$. The dotted-dash line illustrates the average value, 33.61 J/C, for the new determination in this work. The new W/e value in this study is about 1.2% lower than that determined by applying Boutillon's corrections to the earlier results by Niatel et al. (actually, it is the new $(W/e)\left(\frac{\overline{L}_{\Delta}}{\rho}\right)_a^C$ value that is lower than the earlier one). Figure 3.10 also shows a small variation over depth in the graphite phantom for the W/e values determined by Boutillon. But the trend is diminished when the P_{repl} values in this work are applied. This is consistent with the general belief that the W/e value should not change with depth. In this study, the statistical uncertainties of the calculated P_{repl} values for the BIPM chamber are around 0.05-0.08%, which is about the same as the uncertainty (0.06%) used by Niatel et al[44] for their P_{repl} values used to determine the value of W/e. If the 0.1-0.2% systematic uncertainty of calculating P_{repl} values by the LDW method is taken into account (Section 2.5), then the overall uncertainty of the value of W/e in this study is about 0.3%(1σ).

As mentioned earlier, the W/e value obtained by Niatel et al[44] with the second method was 33.81±0.42% J/C. This value is inversely proportional to the BIPM's ^{60}Co exposure standard (or air kerma standard) which has recently been increased by 0.54%.[63] That means the W/e value determined by the second method of Niatel et al should be decreased by 0.54% to a value of 33.63±0.42% J/C which is basically the same as the value of 33.61±0.23% J/C for the calorimetry-based method.

The W/e value determined in Figure 3.10 depends on the selection of the value of

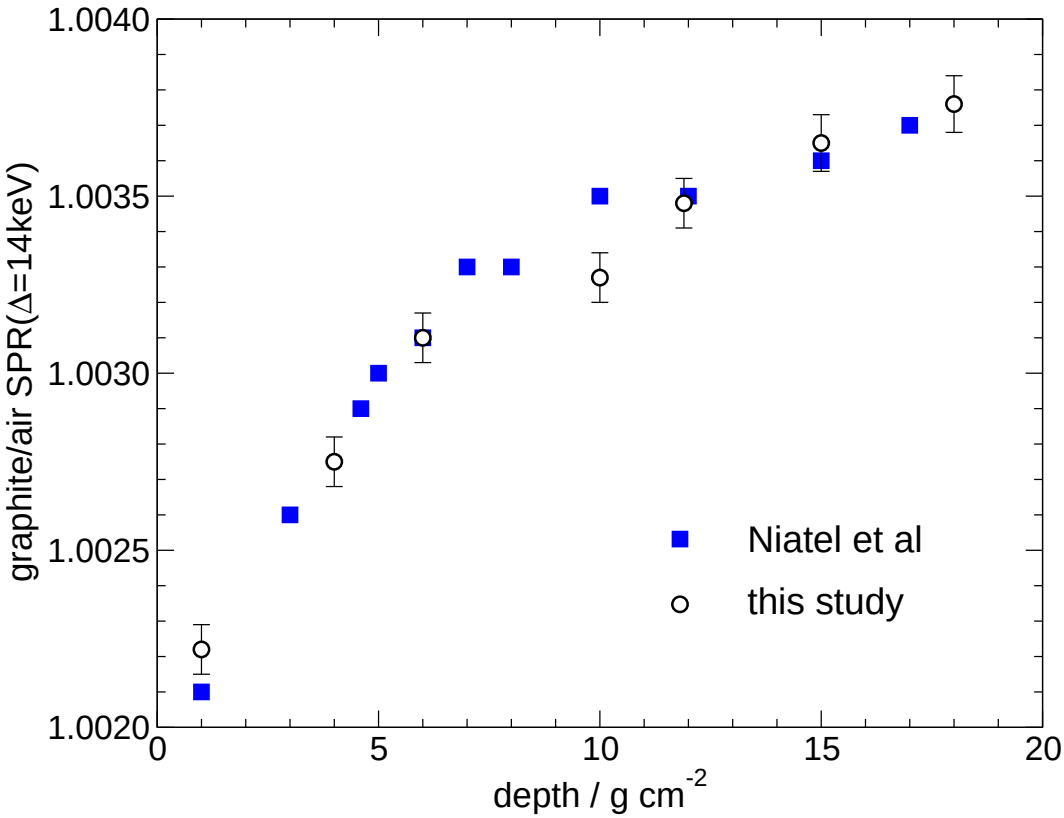

Figure 3.9: The Spencer-Attix graphite/air mean restricted mass collision stopping-power ratio for use with the BIPM chamber as a function of depth in a graphite phantom. Filled squares are the values calculated by Niatel et al.[44] Open circles are the values calculated by SPRRZnrc in this study. The energy threshold for the stopping-power ratio calculation is $\Delta = 14$ keV. From paper III.

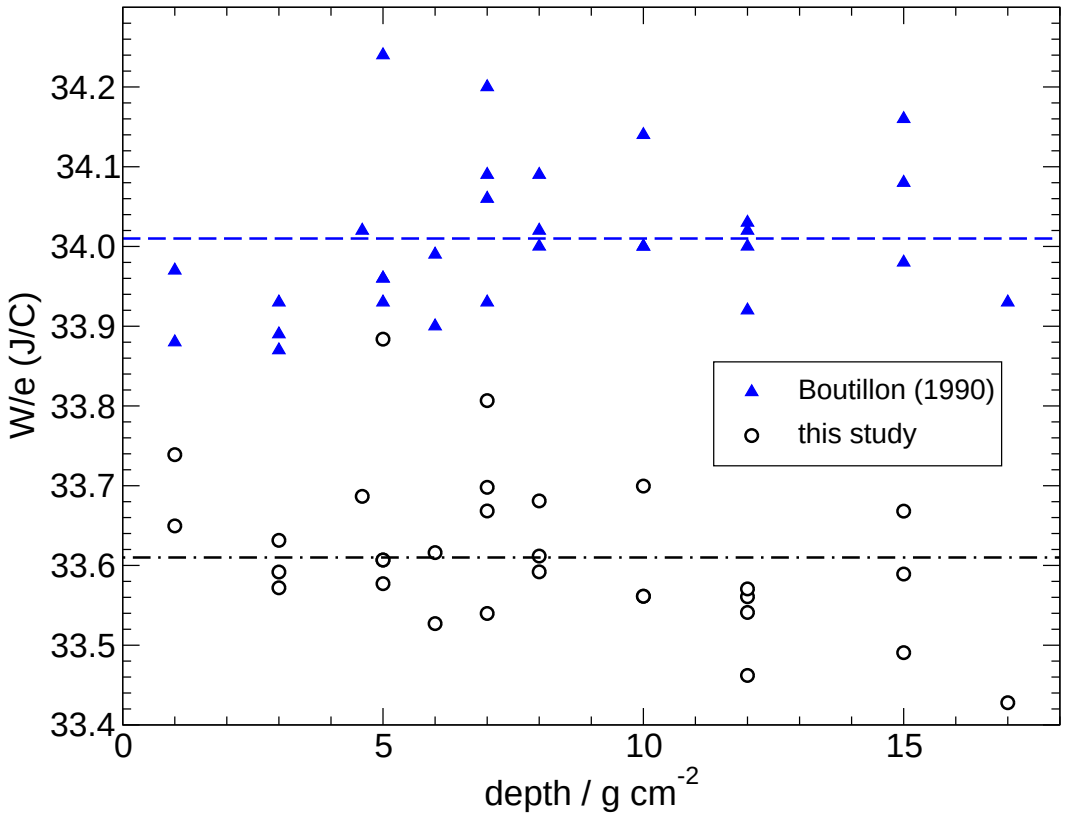

Figure 3.10: Values of W/e obtained from absorbed dose comparisons between the BIPM chamber measurement and the calorimetric measurements of four national standards. The experiments actually measured $(W/e)\left(\frac{\overline{L}_{\Delta}}{\rho}\right)_a^C$ and the W/e values are obtained by dividing $(W/e)\left(\frac{\overline{L}_{\Delta}}{\rho}\right)_a^C$ by the values of $\left(\frac{\overline{L}_{\Delta}}{\rho}\right)_a^C$, which are evaluated based on the ICRU Report 37 stopping powers. Triangle symbols are the values revised by Boutillon[55] from the original values obtained by Niatel et al[44] for the four comparisons. Open circles are the values obtained by assuming unity for the values of P_{repl} for the BIPM chamber. From paper III.

$\left(\frac{\overline{L}_{\Delta}}{\rho}\right)_a^C$, which in turn depends on the mean excitation energy (I-value) of graphite. If an I-value of 86.8 eV and grain density are used to evaluate the graphite stopping power, a calculation by SPRRZnrc for the values of $\left(\frac{\overline{L}_{\Delta}}{\rho}\right)_a^C$ at various depths in a graphite phantom in a ^{60}Co beam gives values of $\left(\frac{\overline{L}_{\Delta}}{\rho}\right)_a^C$ which are 1.6% lower at all depths, than those shown in Figure 3.9. On the other hand, the value of P_{repl} remains unchanged as shown in Figure 3.7. Therefore, in this situation, the W/e value would increase by 1.6%, from 33.61 to 34.15 J/C.

Büermann et al[65] recently did experiments comparing the ionometric and calorimetric determination of absorbed dose to water in a ^{60}Co beam. The ionometric absorbed dose is directly proportional to the $(W/e)\left(\frac{\overline{L}_{\Delta}}{\rho}\right)_a^C$ value. They found that the absorbed dose obtained from the ionometric method, with the standard W/e value of 33.97 J/C and the value of $\left(\frac{\overline{L}_{\Delta}}{\rho}\right)_a^C$ from ICRU Report 37,[54] is about 1.4% higher (with relative uncertainty of 0.36%) than that measured with the water calorimeter. Thus if the proposed 1.2% lower value of W/e is used, their measurements become consistent at the 0.2% level. In their study they also did an analysis in which they used stopping powers based on a graphite I-value of 86.8 eV instead of 78 eV used in ICRU Report 37. This reduces the value of $\left(\frac{\overline{L}_{\Delta}}{\rho}\right)_a^C$ in a ^{60}Co beam by roughly 1.5%.[42] But this change in stopping-power ratio also implies a change in W/e value as described above. If one takes into account both the change in the stopping-power ratio and the change in the measured product of $(W/e)\left(\frac{\overline{L}_{\Delta}}{\rho}\right)_a^C$ then their analysis of their measured data is still consistent. Thus their measurements do not present any information on the preferred value of the I-value for graphite since, in essence, their experiment was sensitive to the product of $(W/e)\left(\frac{\overline{L}_{\Delta}}{\rho}\right)_a^C$ rather than either component separately. In fact their experiment could be considered a measurement of this product.

A direct measurement of W/e value[53] for low-energy electrons has shown that the W/e value approaches a constant value very close to 34 J/C, for electron energy above about 4 keV. As the value of W/e is generally believed to remain constant for higher

energies, referring to the discussions above, this suggests that a higher I-value (e.g. 86.8 eV, or the mean value of 84.5±5 eV mentioned earlier) may be more appropriate than that used in ICRU Report 37. A higher I-value for graphite is also indicated by a recent experiment[66] comparing the air kerma rate measured with a free air chamber to that with a cavity ion chamber. However, this experiment is also subject to uncertainties due to what density effect to use and the possibility of significant fluence perturbation factors at the low photon energies involved.

Chapter 4

P_{repl} for cylindrical thimble ion chambers

4.1 P_{repl} values in electron beams

For cylindrical chambers in electron beams, P_{repl} can be expressed by Equation 1.16, with non-unity values for both P_{gr} and P_{fl}. In Appendix A, the issue of the effective point of measurement (EPOM) for cylindrical chambers in electron beams is studied. The EPOM concept is actually a different approach of accounting for the gradient correction P_{gr}. In this section, the calculations of the fluence correction P_{fl} are studied as well as the calculations of P_{repl} for cylindrical chambers in various electron beams at both d_{max} and d_{ref}. In Table 2.5, it is shown that the P_{repl} values calculated by the two direct methods (HDA and LDW) do not agree with each other. This problem will be resolved in this section and the relationships among P_{repl} values calculated by different methods will be derived.

4.1.1 Relationships between P_{repl} values calculated by different methods

In Appendix A, it is demonstrated that for a cylindrical chamber of radius r to be considered as a Spencer-Attix cavity, the following equation must hold approximately based on Figure A.9

$$\frac{D_{LDW}(z)}{D_{air}(z)} = \left(\frac{\overline{L}_{\Delta}(z-s)}{\rho}\right)_a^w, \tag{4.1}$$

where z is the depth at which the center of the chamber is located and $s = 0.8\,r$ is the shift for matching the primary electron fluence spectrum as derived in Appendix A.1.2. This equation recognizes that the spectrum in the cavity corresponds to that at the effective point of measurement and hence the water/air stopping-power ratio $\overline{L}_{\Delta}/\rho$ is evaluated at depth $z-s$. From the results in Section 2.5.1, the electron fluence spectrum in a thin enough (<20 μm) HDA slab is very similar to that at the same point of measurement in a water phantom. This means the ratio of the dose to water (D_{water}) to the dose to the HDA slab (D_{HDA}) is very close to the water/air stopping-power ratio at the point of measurement at z, i.e.

$$\frac{D_{water}(z)}{D_{HDA}(z)} = \left(\frac{\overline{L}_{\Delta}(z)}{\rho}\right)_a^w. \tag{4.2}$$

Based on these equations, relations among P_{repl} values calculated by different methods can be derived. Dividing Equation 2.6 by Equation 2.5, and using Equations 4.1 and 4.2, one arrives at:

$$P_{\text{repl}}^{LDW}(z) = P_{\text{repl}}^{HDA}(z)\frac{\left(\frac{\overline{L}_{\Delta}(z)}{\rho}\right)_a^w}{\left(\frac{\overline{L}_{\Delta}(z-s)}{\rho}\right)_a^w}. \tag{4.3}$$

Equation 4.3 suggests that the two direct methods of calculating P_{repl} for cylindrical chambers in electron beams no longer give the same values because s is not zero and $\left(\frac{\overline{L}_{\Delta}}{\rho}\right)_a^w$ varies with depth. Equation 4.3 is generally applicable to both cylindrical chambers and plane-parallel chambers in either electron or photon beams. In photon beams, $\left(\frac{\overline{L}_{\Delta}}{\rho}\right)_a^w$ does not vary with depth z, and for plane-parallel chambers in electron beams

$s = 0$, so that in those two cases the two direct methods give the same P_{repl} values as shown in Section 2.7. For cylindrical chambers in electron beams, the LDW method generally gives a higher value of P_{repl} than the HDA method as the water/air stopping-power ratio is smaller at shallower depth as shown in Figure A.8, and hence the ratio of the stopping-power ratios in Equation 4.3 is greater than one. This explains the discrepancy in Table 2.5 between the P_{repl} values calculated by the two direct methods.

The selection of which P_{repl} value to use depends upon the depth at which the water/air stopping-power ratio is evaluated and upon the relative position of the point of measurement and the chamber center. Assuming the chamber center is taken as the point of measurement, if one chooses the water/air stopping-power ratio at the effective point of measurement, i.e. a point upstream from the chamber center, then based on Equations 4.1 and 2.6 the P_{repl} values calculated by the LDW method should be used; but if one chooses the water/air stopping-power ratio at the same depth as the chamber center (this is the method used in the AAPM dosimetry protocols), based on Equations 4.2 and 2.5 the value calculated by the HDA method should be used. In other words, as long as the water/air stopping-power ratio is evaluated at the depth of the center of the chamber in the phantom, the HDA method should be used.

From Equation 2.2, and using Equations 4.2 and 2.5, one has:

$$P_{\text{repl}}^{SPR}(z) = \frac{D_{HDA}(z)}{D_{air}(z)} \frac{D_{water}(z)}{D_{HDA}(z)} \Bigg/ \left(\frac{\bar{L}_{\Delta}(z)}{\rho} \right)_a^w = P_{\text{repl}}^{HDA}(z), \tag{4.4}$$

that is, in principle, the SPR method gives the same P_{repl} values as the HDA method. The results in Table 2.5 support this derivation. The FLU method relies on the similarity of the electron fluence spectrum in the cavity to that in the phantom at the point of measurement, which is obviously not correct as shown in Section A.1.2, thus this method should not be used for cylindrical chambers in electron beams even though it may give approximately the same value as other methods.

4.1.2 Calculation of the fluence correction factor

As the electron fluence spectrum in the cavity is similar to that at a depth shifted 0.8 r upstream from the center of the cavity (see Appendix A.1.2), strictly speaking, Equation 2.1 for D_{water}/D_{air} (page 17) should not be used. Rather, one may write the Spencer-Attix equation using an effective point of measurement approach, to eliminate the gradient effect P_{gr}, as:

$$\frac{D_{water}(z-0.8r)}{D_{air}(z)} = \left(\frac{\overline{L}_{\Delta}(z-0.8r)}{\rho}\right)_a^w P_{fl,0}(z), \tag{4.5}$$

where the water/air stopping-power ratio is now evaluated at a depth $z-0.8r$, since this is where the electron spectrum in phantom resembles that in the cavity centered at z. $P_{fl,0}$ (rather than P_{repl}) is the 'true' fluence perturbation factor which only accounts for the difference in the shape of the electron fluence spectrum in the cavity at depth z compared to that at depth $z-0.8r$ in the phantom without the cavity. One may write Equation 4.5 in a more general form for any shift s as

$$\frac{D_{water}(z-s)}{D_{air}(z)} = \left(\frac{\overline{L}_{\Delta}(z-s)}{\rho}\right)_a^w P_{fl}(z). \tag{4.6}$$

The symbol P_{fl} is used instead of $P_{fl,0}$ to indicate that there are still at least partial gradient corrections involved in the value of P_{fl} if $s \neq 0.8r$. Equation 4.6 reduces to Equation 2.1 when the effective point of measurement is not used, i.e. $s = 0$ and then $P_{fl} = P_{\mathrm{repl}}$. As was done before in calculating P_{repl}, all four methods can be applied to calculate the fluence correction factor, P_{fl}, the only difference is that the phantom dose is calculated at a depth $z-s$. Specifically, for LDW and HDA methods, the following equations are used to calculate the values of P_{fl}:

$$P_{fl}^{LDW}(z) = \frac{D_{water}(z-s)}{D_{LDW}(z)} \tag{4.7}$$

$$P_{fl}^{HDA}(z) = \frac{D_{HDA}(z-s)}{D_{air}(z)} \tag{4.8}$$

Table 4.1: Comparison of the calculated fluence correction factors $P_{fl,0}$ (i.e. P_{fl} when $s = 0.8\ r$) using the four methods for a Farmer chamber cavity centered at d_{ref} in a 6 MeV and in an 18 MeV electron beam. The depth for phantom calculation is shifted upstream by 0.8 r to match the spectra of the primary electrons. From paper VII.

	SPR	FLU	HDA	LDW
6 MeV	0.9645±0.04%	0.9666±0.07%	0.9651±0.05%	0.9647±0.04%
18 MeV	0.9947±0.07%	0.9944±0.12%	0.9946±0.07%	0.9939±0.07%

Table 4.1 lists the $P_{fl,0}$ values calculated by the four methods for a Farmer chamber. All methods give excellent agreement on the values of $P_{fl,0}$ at d_{ref} for the two electron beams.

In the AAPM dosimetry protocols,[7,10] cylindrical chambers are positioned such that the point of measurement or the reference depth z_{ref} is at the center of the chamber cavity and the water/air stopping-power ratio is also evaluated at this point, thus the P_{repl} value calculated by the HDA method should be used according to the results in the previous subsection. In TG-51, a gradient correction factor P_{gr}, defined by Equation 1.13, is explicitly used in the formula (see Equation 1.12), so actually only the values of P_{fl} at the depth z_{ref} are needed in the protocol. In the IAEA's TRS-398,[11] the point of measurement is at what is called the reference point at which the dose is measured by shifting the chamber downstream by an amount $s = 0.5\ r$, i.e. at a depth $z_{ref} + 0.5\ r$, thus the gradient correction is accounted for by the chamber shift. Hence only the values of P_{fl} at depth $z_{ref} + 0.5\ r$ are needed.

4.1.3 The gradient correction factors P_{gr}

In Equation 1.16 (page 12), P_{repl} was written as the product of a gradient correction and a fluence correction. In TG-51,[10] the gradient correction factor at d_{ref} is determined by taking the ratio of the chamber reading at depth $d_{ref} + 0.5r$ to that at d_{ref}, i.e.

$P_{gr}(d_{ref}) = M(d_{ref}+0.5r)/M(d_{ref})$, where $M(z)$ is the chamber reading by a cylindrical chamber with its center at depth z. This is based on the assumption that the chamber reading represents approximately the dose from a point in the phantom upstream by a distance $0.5r$, that is, $M(z) \propto D_{water}(z-0.5r)$, where $D_{water}(z-0.5r)$ is the actual phantom dose at depth $z-0.5r$. Then one may write approximately:

$$P_{gr}(z) = \frac{M(z+0.5r)}{M(z)} \approx \frac{D_{water}(z)}{D_{water}(z-0.5r)} \tag{4.9}$$

Now the question is how accurately the dose ratio in Equation 4.9 can be represented by the chamber-reading ratio. Using an NE2571 chamber model (3.14 mm radius) as an example, the ratios of the chamber reading (i.e. the cavity dose) at $d_{ref}+0.5r$ to that at d_{ref} are calculated for various electron beams from 6 MeV to 22 MeV. The gradient correction factor is in fact not well defined, e.g. there is no special reason to choose $P_{gr}(z)$ as $D_{water}(z)/D_{water}(z-0.5r)$ or as $D_{water}(z+0.5r)/D_{water}(z)$. Using Equation 1.16, the value of P_{gr} may also be expressed as $P_{\rm repl}/P_{fl}$, where $P_{\rm repl}$ and P_{fl} can be calculated separately. The values of P_{gr} for all of these definitions are calculated and compared to the ratios of the chamber reading for the NE2571 chamber at depths close to d_{ref} for both a 6 MeV beam and an 18 MeV beam.

The calculation results for the verification of Equation 4.9 for various electron beams are shown in Figure 4.1. The chamber-reading ratio is systematically lower than the corresponding dose ratio. For high-energy beams, the discrepancy is 0.3%; and for low-energy beams, the discrepancy is more than 1%. The calculation results for the NE2571 air cavity (no wall and central electrode) suggest that the discrepancy is mainly from the replacement effect but partly from the wall effect. These results demonstrate that the gradient correction factor P_{gr} as defined in Equation 4.9 (also in TG-51) for the NE2571 chamber has an uncertainty of 0.3% for high-energy beams and more than 1% for low-energy beams. Figure 4.2 compares the P_{gr} values at d_{ref} for different definitions of P_{gr} in (a) a 6 MeV electron beam, and (b) an 18 MeV electron beam. The figure shows that the P_{gr} values vary among different calculation methods by more than 1%

for the 6 MeV beam and by 0.4% for the 18 MeV beam. The large uncertainty in low-energy beams is due to the steep dose gradient of the depth-dose curve and finite size of the Farmer-type chamber. The amount of shift of 0.5 r, adopted in current dosimetry protocols for all electron beams, also contributes to the uncertainty of the P_{gr} values since it is demonstrated that for electron beams of different energies the amount of shift should also be different (see Appendix A or Johansson et al[13]).

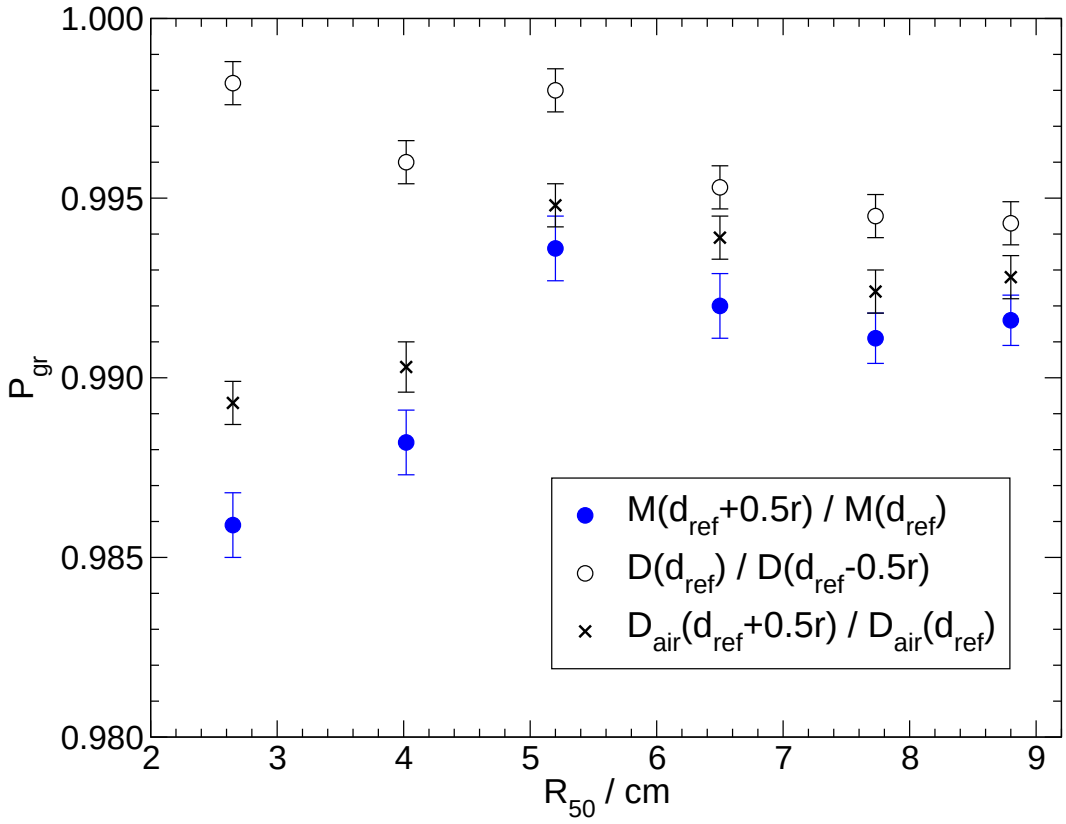

Figure 4.1: The calculated gradient correction P_{gr} as defined in TG-51 dosimetry protocol[10] for NE2571 chamber (3.14 mm cavity radius) in various electron beams (filled circles). The ratio of phantom doses (open circles) is presumed to be represented by the ratio of the chamber readings according to Equation 4.9. Cross symbols are the results for the air cavity only, i.e. the NE2571 chamber without wall and central electrode. From paper VII.

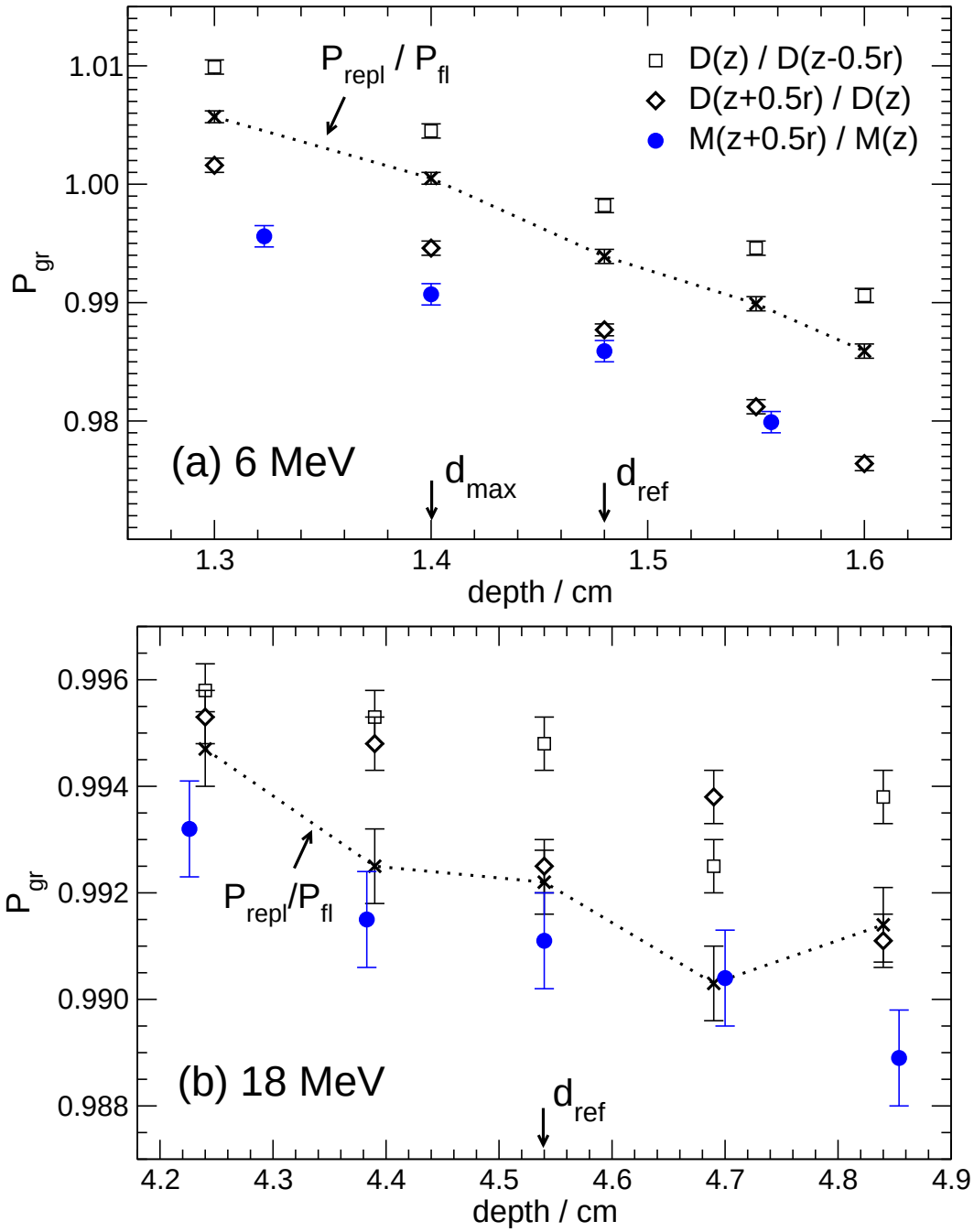

Figure 4.2: Comparison of the values of P_{gr} calculated by different definitions for the NE2571 chamber at depths near d_{ref} for (a) a 6 MeV electron beam, and (b) an 18 MeV electron beam. From paper VII.

4.1.4 P_{repl} and P_{fl} vs depth

Figure 4.3 shows P_{repl} values calculated by the two direct methods, HDA (Equation 2.5) and LDW (Equation 2.6), for the Farmer chamber as a function of depth in both the 6 MeV and 18 MeV electron beams. The LDW method gives a higher value at all depths as expected from Equation 4.3. The very large P_{repl} values at deeper depths are due to the steep dose gradient near R_{50} for electron beams. Since in both the AAPM and IAEA dosimetry protocols the gradient effects have been separated out, only the values of P_{fl} are needed and they are calculated by Equations 4.7 and 4.8. The depth dependence of P_{fl} values is illustrated in Figure 4.4 for two different shifts of the point of measurement, $s = 0.8\ r$ and $s = 0.5\ r$, in electron beams of energy (a) 6 MeV and (b) 18 MeV. In this figure, the chamber cavity is located at the specified depth but the phantom dose is calculated at a depth shifted upstream by s. For an $s = 0.8\ r$ shift, P_{fl} is the 'true' fluence correction factor, $P_{fl,0}$, since the electron fluence spectra are similar as discussed in Appendix A.1.2. The variation of P_{fl} vs depth (from d_{ref} to R_{50}) can be as large as 15% for the 6 MeV beam and 5% for the 18 MeV beam, even though it is relatively constant from the surface to d_{ref}. The very large values of P_{fl} at depths close to R_{50} mean that the scattered electrons are becoming dominant over the primary electrons, and the actual shift needed should be shorter than $0.8\ r$ or $0.5\ r$. For an $s = 0.5\ r$ shift, which is currently used by dosimetry protocols, the variation of P_{fl} values vs depth is greatly reduced. This is reasonable since the shift value of $0.5\ r$ was obtained by matching the depth-dose curves (see Appendix A.1.1), which effectively makes the averaged variation in the P_{fl} value a minimum. For $s = 0.8\ r$, P_{fl} remains almost constant from surface to d_{ref} for the 18 MeV beam. For $s = 0.5\ r$, P_{fl} is not a 'true' fluence correction factor, because it partly contains the contribution from the gradient effect, which accounts for the variation of P_{fl} by 1% from the surface to a depth beyond d_{ref} for the 18 MeV beam. Since a good match of the electron fluence spectrum is reached at $s = 0.8\ r$, a $0.5\ r$ shift will result in a small mis-match of the electron fluence spectrum as discussed in the

previous section. This will inevitably lead to a discrepancy in values of P_{fl} calculated by different methods. It can be seen from Figure 4.4 that the difference in the calculated P_{fl} values from the HDA vs LDW methods is more observable when the shift is $s = 0.5\ r$.

4.1.5 Beam quality dependence of P_{repl}

Figure 4.5 shows the beam quality dependence of the calculated P_{repl} values for a Farmer chamber at both d_{max} and d_{ref} in a water phantom for either real linac electron beams[40] or mono-energetic electron beams (with energies 6, 12, 18 and 24 MeV). In Figure 4.5(a), the abscissa is the mean electron energy at depth z, $\overline{E}_z$, determined from Harder's relation (Equation 1.15). The apparent large discrepancies in Figure 4.5(b) between values for realistic vs mono-energetic electron beams suggest that R_{50} is not a good beam quality specifier for the values of P_{repl}. Although the mean electron energy at depth makes agreement look better as shown in Figure 4.5(a) for different beams, the discrepancy is still large especially for low-energy beams. This is most likely because the gradient effect at the reference depth varies for different beams having the same R_{50}. This is why the gradient correction is generally explicitly accounted for in dosimetry protocols.

4.1.6 Beam quality dependence of P_{fl} and comparison with measurements

Figure 4.6 shows the calculated P_{fl} values for a Farmer chamber at both d_{max} and d_{ref} in a water phantom irradiated by a realistic linac spectrum source[40] (nominal energy from 6 MeV to 22 MeV) and/or mono-energetic electron beams (6, 12, 18 and 24 MeV).

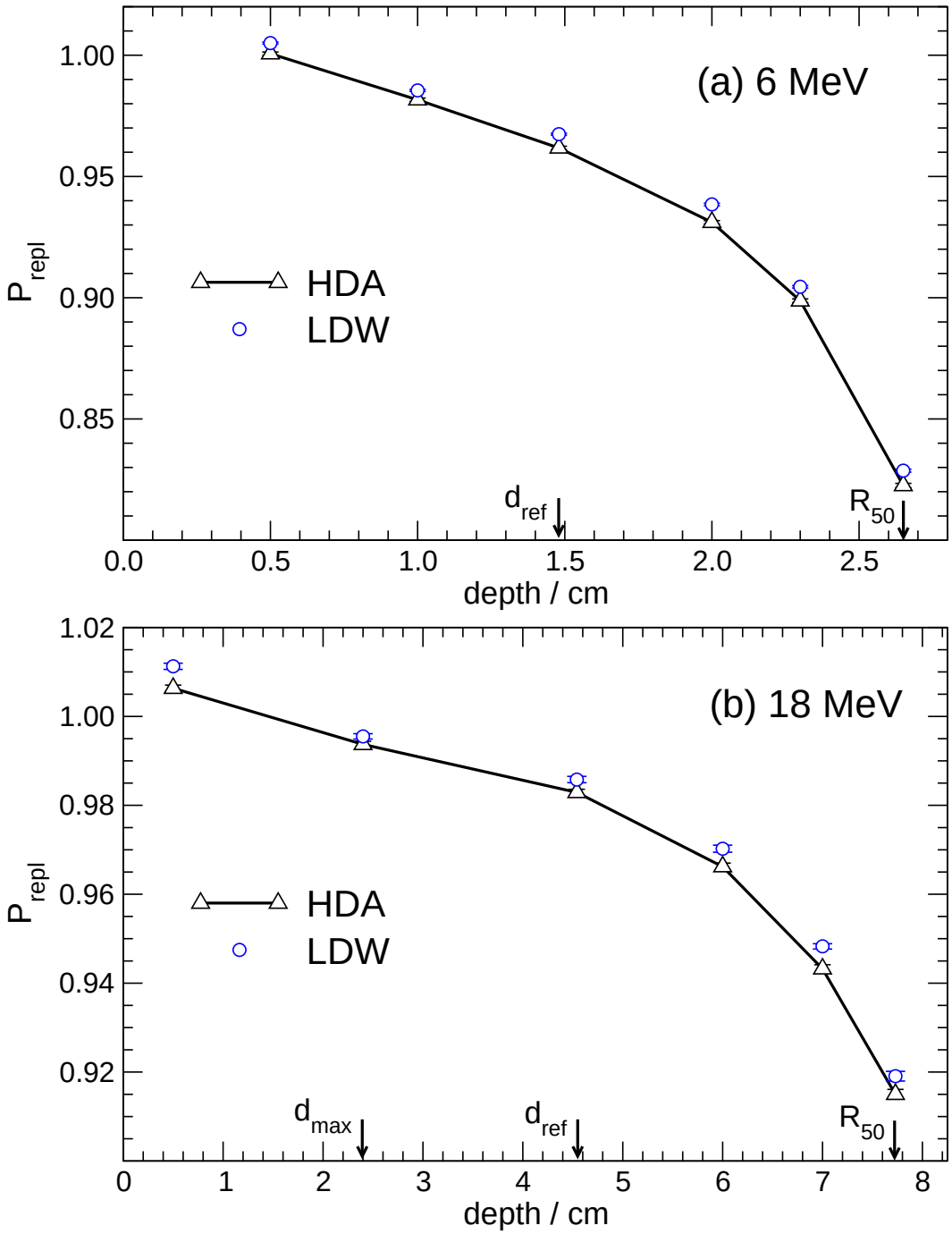

Figure 4.3: P_{repl} values calculated by the two direct methods (Equations 2.6 and 2.5) for the cavity of a Farmer chamber as a function of depth in (a) a 6 MeV beam and (b) an 18 MeV electron beam. The depth is specified by the location of the center of the chamber cavity. The differences between the two methods are predicted by Equation 4.3. From paper VII.

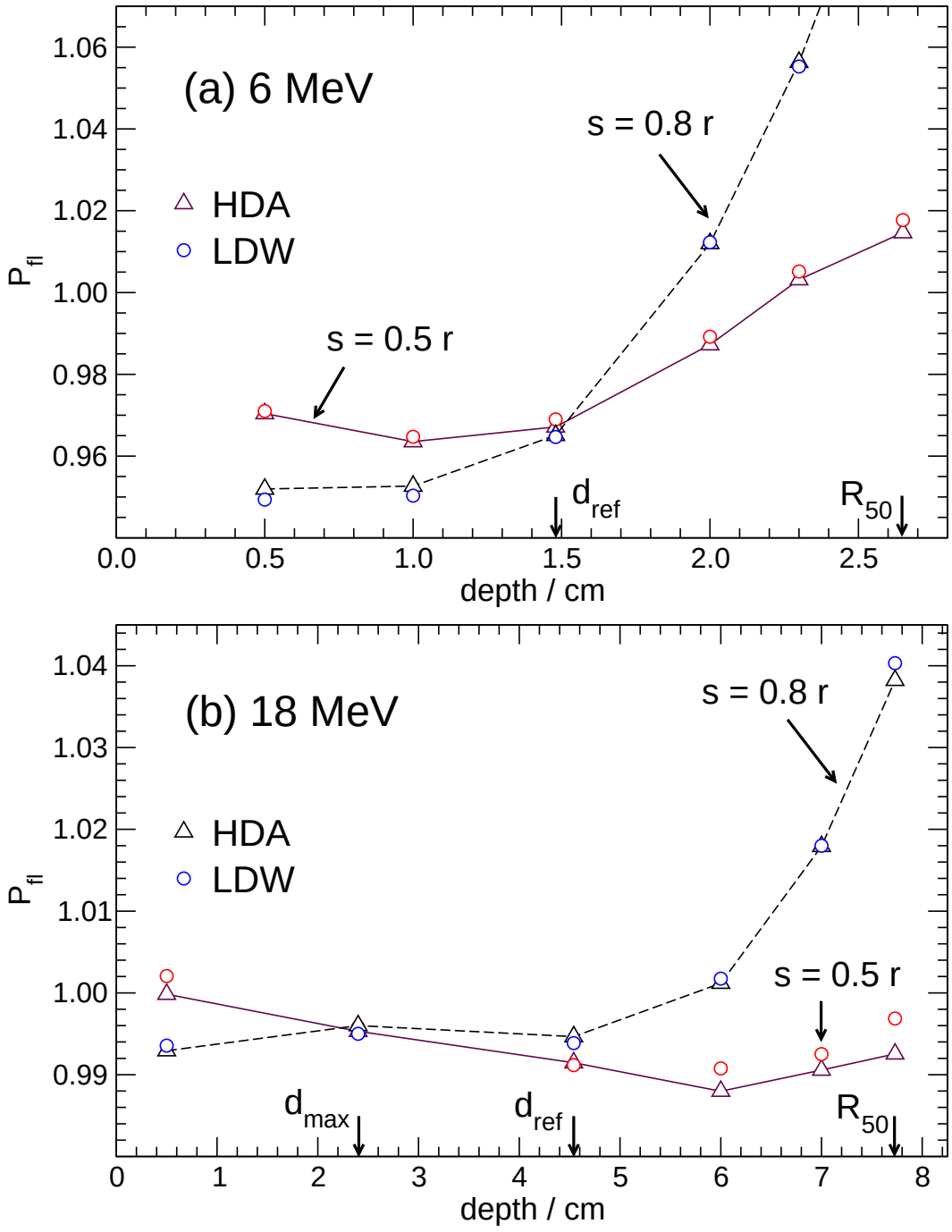

Figure 4.4: The values of fluence correction (P_{fl}) calculated by the two direct methods (Equations 4.7 and 4.8) for the cavity of a Farmer chamber as a function of depth in (a) 6 MeV and (b) 18 MeV electron beams. The depth is specified by the location of the center of the chamber cavity. For the phantom dose calculation, the depth is shifted upstream by either $s = 0.5\ r$ or $s = 0.8\ r$ (see Section 4.1.2 for details on P_{fl} calculations). From paper VII.

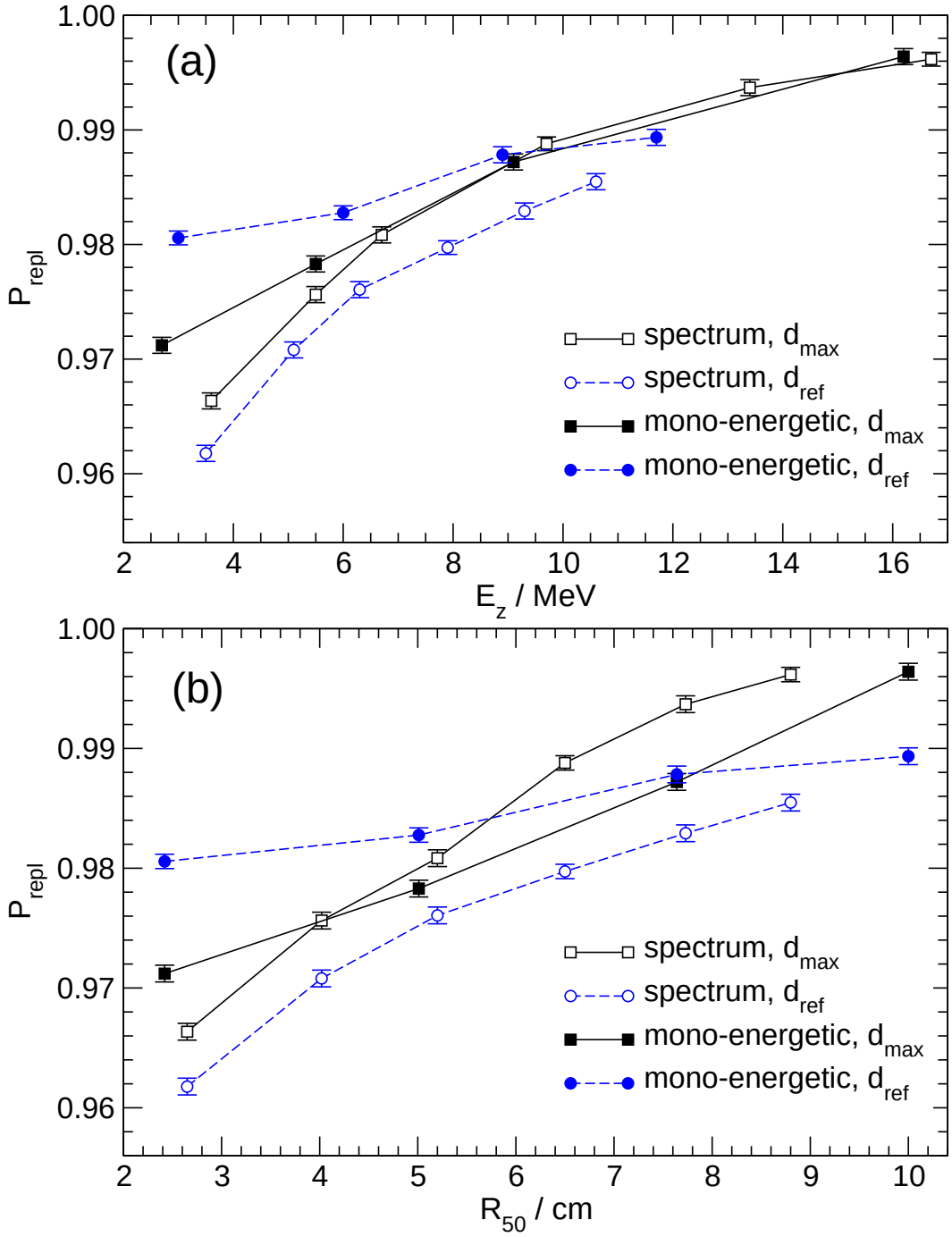

Figure 4.5: Comparison of the calculated P_{repl} values for a Farmer chamber at either d_{max} or d_{ref} in a water phantom for both real linac electron beams (open symbols, with nominal energy ranging from 6 to 22 MeV) and mono-energetic incident electron beams (corresponding solid symbols, with energies 6, 12, 18 and 24 MeV) as a function of (a) the mean electron energy at depth calculated from Harder's relation (Equation 1.15), and (b) R_{50}. From paper VII.

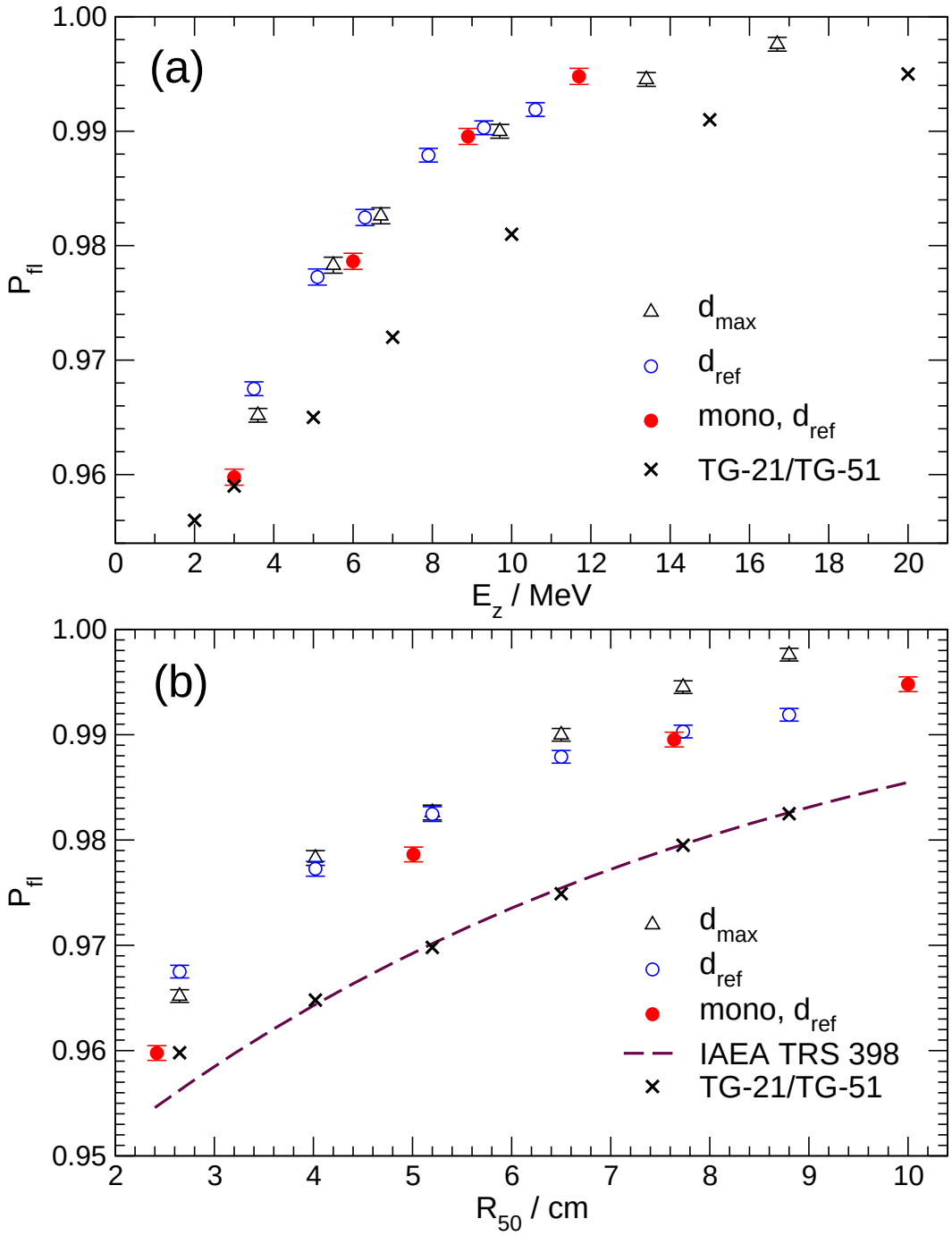

Figure 4.6: (a) The calculated P_{fl} values for a Farmer chamber in electron beams as a function of the mean electron energy at depth calculated from Harder's relation. P_{fl} values at d_{max} and/or at d_{ref} for both real linac beams (open symbols) and mono-energetic beams (solid symbols) are shown. The HDA method is used in the calculation with $s = 0.5\ r$. The cross symbols are the TG-21/TG-51 values which are based on Johansson et al's measurement[13] at d_{max}. (b) Same data sets as in (a) but with R_{50} as the beam quality specifier. The dashed line is the P_{fl} values used in IAEA's TRS-398.[11] From paper VII.

In Figure 4.6(a), the results are plotted as a function of the mean electron energy at depth and are compared to the TG-21/51 values[7] which were based on the experimental work of Johansson et al.[13] The same sets of data are plotted in Figure 4.6(b) where R_{50} is used as the beam quality specifier and the results are compared to the P_{fl} values used in TG-51 and TRS-398, which were re-cast from the experimental measurements of P_{fl} at d_{max}. The HDA method is used in the calculation since in the experiments the water/air stopping-power ratio was evaluated at the center of the cavity which is the point of measurement. The values of P_{fl} are calculated by Equation 4.8 where a shift of $0.5\,r$ is used to correspond to the value adopted in dosimetry protocols. In Figure 4.6(a), the calculated values of P_{fl} for the spectrum source at d_{ref} lie on the same curve as those at d_{max}, as well as the P_{fl} values at d_{ref} for the mono-energetic beams. This means that the mean electron energy at depth, $\overline{E}_z$, is a good beam quality specifier for P_{fl}. These results demonstrate that, consistent with experimental findings,[67] TG-51's adoption of P_{fl} values at d_{max} with the same mean electron energy for use at d_{ref} is reasonable, although there is a clear discrepancy in the values actually used. In Figure 4.6(b), R_{50} may be a good beam quality specifier if we are only interested in the P_{fl} values at d_{ref}. Figure 4.6 also shows that the calculated P_{fl} values are systematically higher by 0.5-1% than the TG-21/51 or the IAEA TRS-398 values. The values in the dosimetry protocols are based on measurements in a PMMA phantom, while P_{fl} values in this study are calculated in a water phantom. To see if this difference accounts at least partly for the discrepancy, the $P_{\rm repl}$ values for PMMA are calculated by the SPR method at d_{max} in a PMMA phantom for a few electron beams and the values are only 0.1% lower than those for water. This demonstrates that TG-21's recommendation of $P_{\rm repl}$ values at d_{max} for PMMA being used for water is reasonable.

The $0.5\% \sim 1\%$ systematic difference can be explained as follows. The experimental values were based on the assumption that the plane-parallel chamber used in the comparison with the cylindrical chamber was perturbation free, specifically, the wall

correction factor P_{wall} is 1. However, recent studies[28] have shown that P_{wall} for most plane-parallel chambers in a water phantom in electron beams is in the range of 1.005 to 1.015 for electron energies of 20 to 6 MeV. Although there is no detailed information about the plane-parallel chamber used in Johansson et al's experiments, it is highly probable that it had a similar wall effect. For example, the wall corrections for the NACP02 chamber in a PMMA phantom irradiated by a 6 MeV or a 12 MeV electron beam are calculated and the values of P_{wall} are 1.005 and 1.004 with 0.1% statistics. On the other hand, the values of P_{repl} for well-guarded plane-parallel chambers have shown to be very close to unity (within 0.4%) at d_{max} in electron beams (Table 2.4); and no wall correction was needed for the cylindrical chambers as the wall material (PMMA) was the same as the phantom. Therefore, the actual measured values by Johansson et al (i.e. TG-21/51 or TRS-398 values) should be roughly 0.5-1.5% larger than those shown in Figure 4.6, in which case the agreement with the calculated values would be better.

4.1.7 Cavity size dependence and an empirical formula for P_{fl}

Figure 4.7 shows the beam quality dependence of the P_{fl} values calculated at d_{ref} for realistic electron beam spectra[40] ranging from 6 MeV to 22 MeV, for cylindrical chambers of three different cavity radii, when R_{50} is used as the beam quality specifier. The solid lines are the values calculated by the following empirical formula expressing P_{fl} values as a function of R_{50} (in cm) and the radius of the chamber cavity r (in mm):

$$\begin{aligned} P_{fl}(d_{ref}) &= 0.9902 - 0.016\ r + 0.01218\ ln\ R_{50} + 0.000083\ r^2 \\ &\quad - 0.0035\ (ln\ R_{50})^2 + 0.00593\ r\ (ln\ R_{50}). \end{aligned} \tag{4.10}$$

With this formula, the maximum deviation from the Monte Carlo calculated values is less than 0.2% for all the data points. Equation 4.10 is applicable to situations where the center of the chamber's cavity is defined as the point of measurement and is placed at d_{ref}, i.e. the P_{fl} values calculated by the formula are only applicable to the AAPM

TG-51 dosimetry protocol but not IAEA's TRS-398 in which case the P_{fl} values at depth $d_{ref} + 0.5\ r$ are needed. However, the P_{fl} values from Equation 4.10 may still be used in IAEA's Code of Practice if the difference between perturbation factors at the two depths is ignored. According to Figure 4.4, the difference between the P_{fl} value at d_{ref} and that at $d_{ref} + 0.5r$ is negligible for high-energy electron beams.

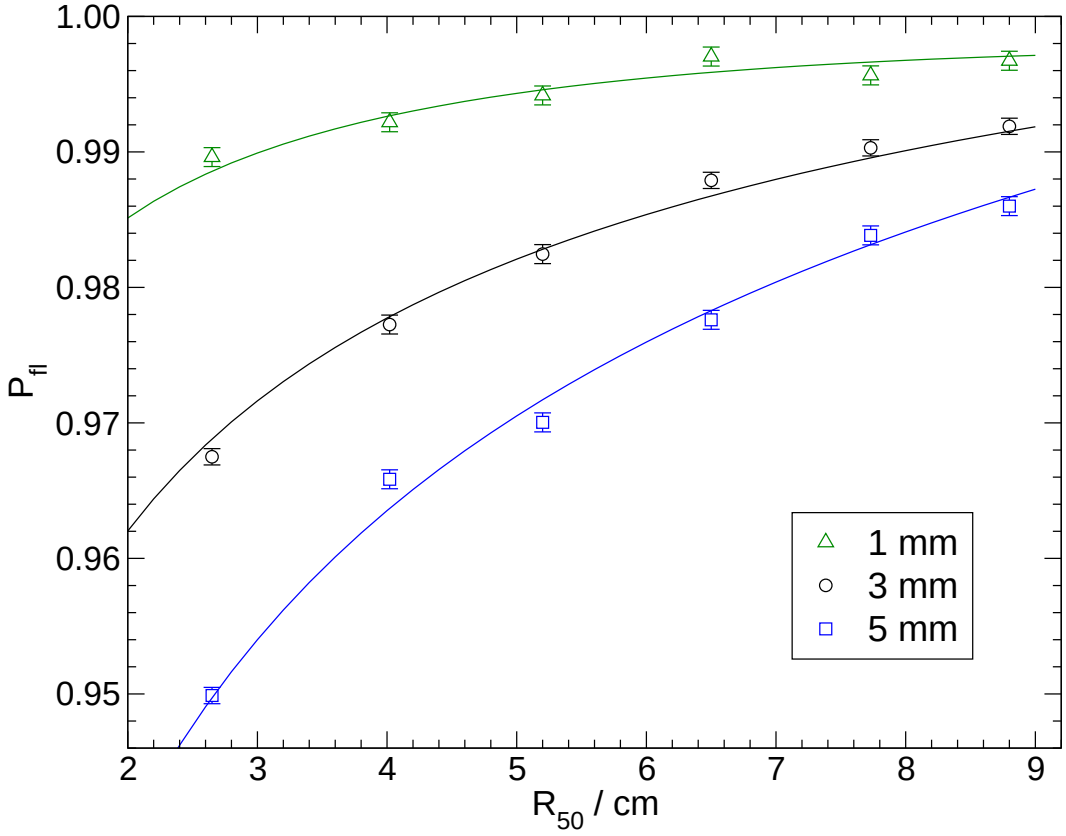

Figure 4.7: The beam quality dependence of the calculated P_{fl} values at d_{ref} for cylindrical chambers of length 2 cm for three cavity radii (1, 3, and 5 mm) in realistic electron beams[40] ranging from 6 MeV to 22 MeV. R_{50} is used as the beam quality specifier. The chamber cavity center is defined as the point of measurement or the reference point. The HDA method is used in the calculations with a shift of 0.5 r. The solid lines are the values calculated for the three cavity radii from Equation 4.10. From paper VII.

Figure 4.8 shows the calculated P_{fl} values at d_{ref} in electron beams for different cavity lengths for cylindrical chambers of a diameter 6 mm. For a low-energy beam

(6 MeV), the variation of P_{fl} values over cavity lengths from 0.5 cm to 3 cm can be as large as 0.5-0.6%. For high-energy electron beams, the variation is at most 0.3%.

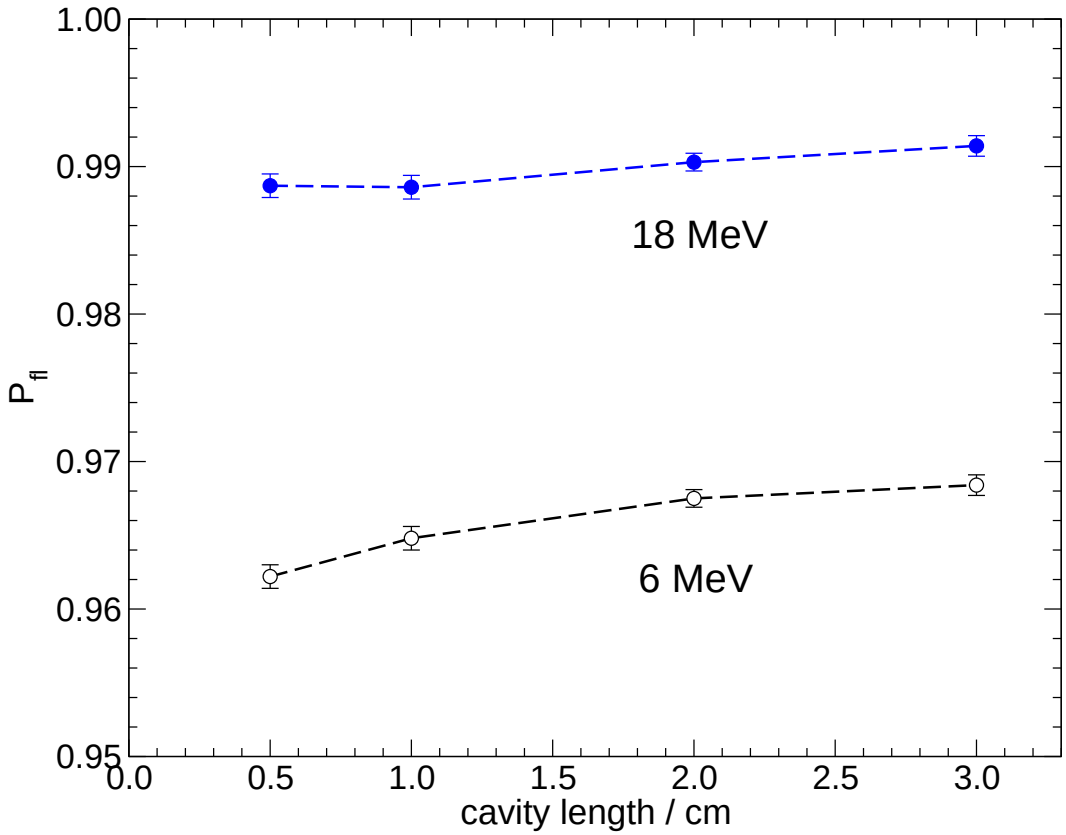

Figure 4.8: Calculated P_{fl} values versus the length of the cavity for cylindrical chambers of diameter 6 mm at d_{ref} in a 6 MeV (opened symbols) and in an 18 MeV (filled symbols) electron beam. The center of the chamber cavity is the point of measurement. The HDA method is used in the calculations with a shift of 0.5 r. From paper VII.

4.2 P_{repl} values in photon beams

In photon beams, since the fluence correction P_{fl} is taken as unity due to the transient charged particle equilibrium, P_{repl} is just the gradient correction P_{gr}. According to the IAEA, for cylindrical chambers in high-energy photon beams, the value of P_{gr} "is one of the major contributions to the final uncertainty in k_Q".[11] The estimated uncertainty

of the P_{gr} ratio entering into the k_Q value is 0.5%.[11] The values of P_{repl} used in the two major current dosimetry protocols are also significantly different as mentioned in Section 1.4. Andreo et al[68] tried to resolve this discrepancy between the AAPM and the IAEA protocols by using the ACCEPT/ITS[69] Monte Carlo codes to calculate the response of cylindrical chambers in a ^{60}Co beam, but did not reach a definite conclusion, partly because the calculation's statistical uncertainty was too large. In this section, the EGSnrc codes are used to simulate both Cunningham and Sontag's[15] experiments and Johansson et al's[13] experiments to determine the values of P_{repl}. The simulation results are compared to the measurements. The values of P_{repl} for cylindrical chambers of different radii in various high-energy photon beams are calculated and an empirical formula is given.

4.2.1 Simulation of Cunningham and Sontag's experiments

In Cunningham and Sontag's experiments to measure P_{repl}, which was called the displacement correction, a Farmer chamber was put at about 5 cm depth in the center of a hole of diameter 3.2 cm and length 2.5 cm in a PMMA phantom. Response was measured as a series of PMMA sleeves was added until the hole was completely filled. The relative response of the chamber in a ^{60}Co beam was recorded and the results were plotted as a function of the water equivalent outer radius of the sleeves. The water equivalent radius is scaled by the relative mass density and the electron density. Then, a linear regression was done to extrapolate the curve to zero radius, where the chamber response was normalized to one. Their experimental results are shown in Figure 4.9. The figure also shows the cavity radius dependence of P_{repl} calculated by the LDW method for a cylindrical cavity of length 2 cm. Note that P_{repl} approaches 1 as the cavity radius decreases to 0, as is expected. There is, however, an apparent discrepancy between the calculated P_{repl} and the experimental results. Even the slopes in the linear part of the curve are different.

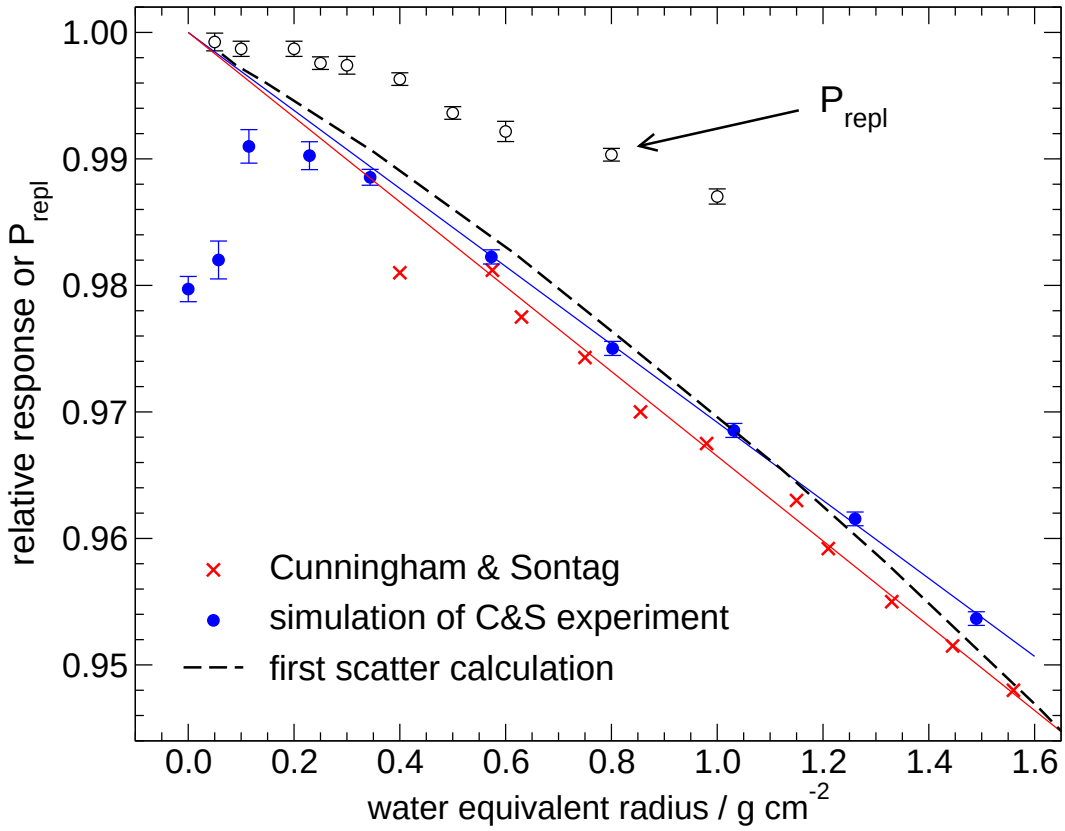

Figure 4.9: Experimental measurements used by Cunningham and Sontag (×) to determine the displacement correction in a ^{60}Co beam. The Monte Carlo simulation of their measurements are shown as filled circles. Dashed line is the first scatter calculation of air-kerma made by Cunningham and Sontag. Open circles are the values of P_{repl} for a cylindrical cavity of length 2 cm as a function of the cavity radius, calculated by the LDW method. Solid lines are the linear regressions for measured and Monte Carlo simulated responses for radii larger than 0.6 g/cm^2. From paper II.

To investigate this further, the actual experiment is simulated by the Cavity code: an ion chamber with an air cavity of diameter 6 mm and length 2.5 cm with variable wall thickness is put in a hole (filled with air) of diameter 3.2 cm and length 2.5 cm, which is located at 5 cm depth in a PMMA phantom irradiated by a ^{60}Co beam. The wall material is also PMMA and the dose in the air cavity, which is proportional to the chamber response, is scored while the wall thickness is gradually increased to fill the entire hole. A linear regression is done for data points where the wall thickness is greater than 0.4 g/cm^2 and the data points are normalized at the extrapolated zero wall

thickness. These simulation results are also represented in Figure 4.9. The agreement of the simulation results with the measurement is excellent. The distinction between our P_{repl} calculation and the simulation of the experiments demonstrates that the original interpretation of the experimental results in terms of P_{repl} is incorrect. Cunningham and Sontag[15] conceded that their interpretation was part of an on-going controversy. In retrospect it was inappropriate for both the TG-21[7] and TG-51[10] protocols to interpret these measurements and calculations which were about kerma as being related to P_{repl} which concerns the change in the electron fluence spectrum.

4.2.2 Simulation of Johansson's experiments

Johansson et al[13] measured the depth-ionization curves in a PMMA phantom by using cylindrical chambers of different diameters (3, 5 and 7 mm) for photon beams ranging from ^{60}Co to 42 MV. The wall material for these chambers was also PMMA with a 50 μm graphite internal coating. These depth-ionization curves were normalized at the depth of maximum ionization, d_{max}. Then the ratios of the relative ionizations in different chambers were determined for depths larger than d_{max}. The displacement factor (DF) was obtained by [1]

$$DF(\% \cdot mm^{-1}) = \frac{1 - (J'_{air,1}/J'_{air,2})}{r_2 - r_1} \tag{4.11}$$

where $J'_{air,1}/J'_{air,2}$ is the ratio of the relative ionization per unit mass of air for chamber 1 and 2 (hereafter referred to as the mass ionization), r_1 (r_2) is the radius of chamber 1 (chamber 2), assuming $r_2 > r_1$. Since they did not know the absolute mass ionization for these cylindrical chambers, Johansson et al measured the relative ionization J'_{air} for the 5 and 7 mm diameter chambers normalized to the 3 mm chamber in a variety of photon beams of different energies. They found that the ratios of the two ionizations (i.e. 5 mm to 3 mm, or 7 mm to 3 mm) at d_{max} was independent of the photon beam

[1] Karl-Axel Johansson, private communication, 2008.

quality. They then assumed that the fluence perturbation was negligible near d_{max} where there was an approximate charged particle equilibrium. In addition the gradient correction was also negligible near d_{max}. They concluded that the measured relative ionization represented the relation of the effective air mass between chambers and the mass ionization at d_{max} for different chambers must be the same. That means the mass ionizations in Equation 4.11, $J'_{air,1}$ and $J'_{air,2}$, were actually normalized to the respective mass ionization at d_{max}.

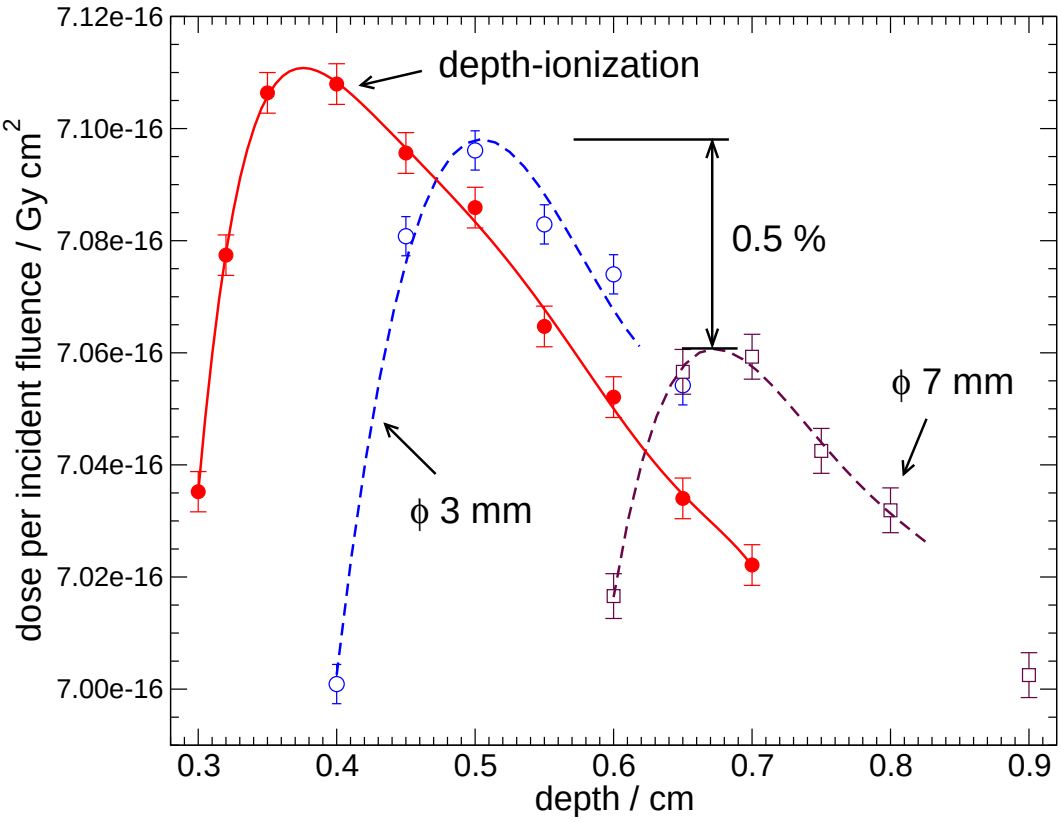

Figure 4.10: Calculated chamber cavity dose (open symbols), which is proportional to the mass-ionization or chamber response, near depth of maximum dose in a PMMA phantom irradiated by a ^{60}Co beam. Two chambers of diameter 3 mm and 7 mm are modeled. The solid circles are the calculated depth-ionization curve based on a depth-dose curve corrected by the PMMA/air stopping power ratio with $\Delta = 10$ keV. Lines are the polynomial fits to the symbols, respectively. From paper IV.

The experiments are simulated with the Cavity code by modeling two cylindrical

cavities of diameters 3 and 7 mm at various depths in a PMMA phantom irradiated by a ^{60}Co beam and linac photon beams of energies from 4 MV to 18 MV. Since the W/e factor is believed to be constant, the chamber cavity dose is proportional to the mass-ionization of the chamber, i.e. $D_{air,1}/D_{air,2} = J_{air,1}/J_{air,2}$, where $D_{air,i}$ and $J_{air,i}$ are the absolute dose and the absolute mass-ionization in the cavity of chamber i, respectively. For this reason, the terms 'cavity dose' and 'mass-ionization' or 'chamber response' will be used interchangeably here. Figure 4.10 shows the calculated cavity dose near d_{max} for the two modeled chambers in the ^{60}Co beam, together with the calculated depth-ionization curve calculated from the depth-dose curve corrected for the PMMA/air stopping power ratio (with $\Delta = 10$ keV). The calculated cavity dose is the absolute dose in the cavity per unit incident photon fluence and the depth-ionization curve is the absolute dose to air in a perturbation-free cavity per unit incident photon fluence. The only purpose of the polynomial fitting for the calculated points is to find d_{max} and the maximum cavity dose (or maximum mass-ionization or response). Contrary to Johansson et al's belief, the mass ionization at d_{max} for the 7 mm chamber is not the same as that of the 3 mm chamber, and they both are lower than the maximum value on the ideal depth-ionization curve. The maximum mass ionizations obtained this way are subsequently used in the normalization of the relative mass ionizations at all depths, as was done in the experiments. The same procedure (i.e. calculating the depth-ionization curve, finding the maximum mass ionization, and normalizing at d_{max}) is repeated for the 4 MV and 18 MV photon beams. Using Equation 4.11, the displacement factors are calculated for the three photon beams at a variety of depths in the phantom.

The calculated displacement factors from the simulation of Johansson et al's experiments are compared to the measurements in Figure 4.11 as a function of depth in phantom. There is excellent agreement for the ^{60}Co beam; and good agreement is also obtained for the 4 MV and the 18 MV beams, although they are compared to the

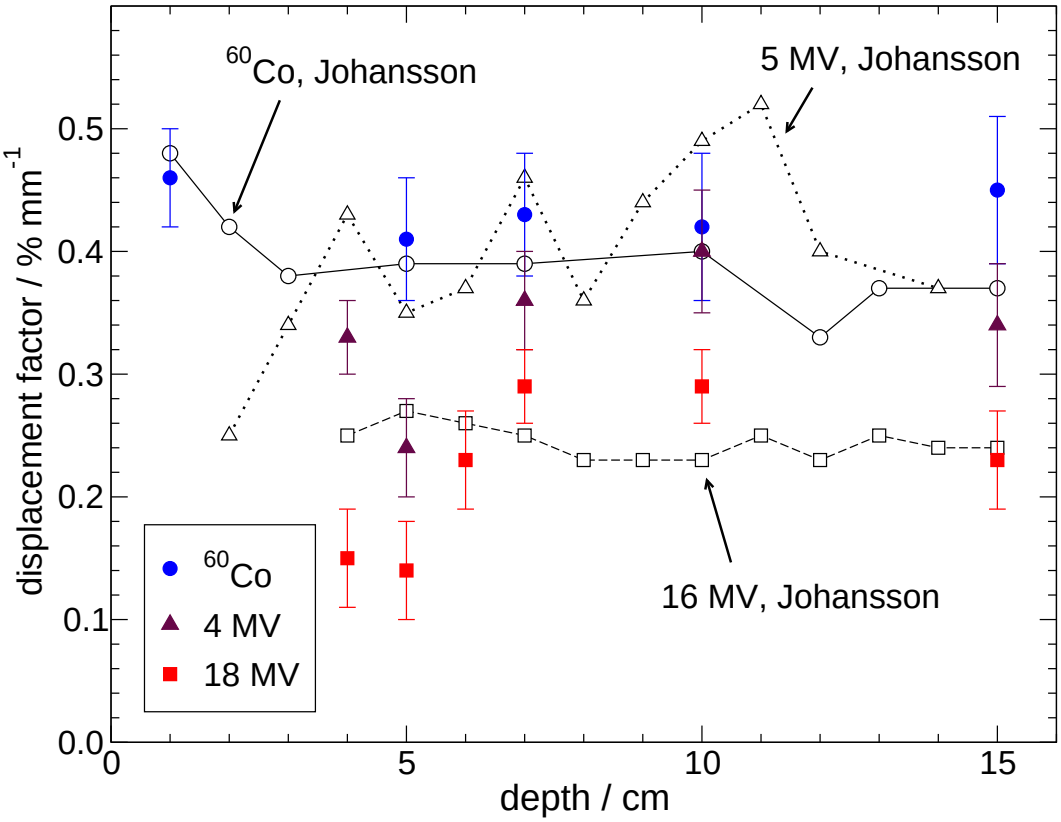

Figure 4.11: Measured displacement factors (open symbols) for a ^{60}Co, a 5 MV and a 16 MV photon beam (data from Johansson et al[13]) as compared to the calculated values (solid symbols) for a ^{60}Co, a 4 MV and an 18 MV photon beam as a function of depth in a PMMA phantom. The calculated values are from the simulation of the two chambers of diameter 3 mm and 7 mm. From paper IV.

measured values for a 5 MV and a 16 MV beam, respectively, since no photon spectral data were available in this study for a 5 MV or a 16 MV beam; and, more importantly, those linacs were manufactured about 30 years ago; thus, even with the same accelerating voltage, the actual photon beam quality may not be the same as those from a modern linac. For the 4 MV beam, the lower value of the displacement factor at 5 cm is likely due to the statistics. For the 18 MV beam, the lower values of the displacement factor at 4 and 5 cm are because of the lack of charged particle equilibrium at these depths for this high-energy beam. Note that the experimental values for the ^{60}Co beam vary significantly from 0.33 to 0.48; and the measured values of the displacement factor for the 5 MV beam are even more dispersed as a function of depth. This indicates that the method itself is not reliable in determining the displacement factor. If one takes the variation of the displacement factor DF versus the variation of the mass ionization ratio $R = J'_{air,1}/J'_{air,2}$ in Equation 4.11, one obtains

$$\frac{\delta DF}{DF} = \frac{-R}{1-R}\frac{\delta R}{R}. \tag{4.12}$$

As R is very close to 1, Equation 4.12 suggests that the relative uncertainty of the displacement factor could be very large. In fact, for the two chambers of diameter 3 mm and 7 mm, the ratio R is about 0.99 at all depths for a ^{60}Co beam, and even closer to unity for higher energy beams. This gives a relative uncertainty for the displacement factor which is at least 100 times larger than the relative uncertainty of the ionization ratio R. For example, if the experimental uncertainty on R in the ^{60}Co beam is 0.2%, then the uncertainty on DF will be at least 20%. Aside from the fluctuations of the DF values, it is expected that the values should not depend on depth since transient charged particle equilibrium exists in photon beams and the electron fluence spectra change little versus depth.

For a ^{60}Co beam, the measured displacement factor DF is 0.4 % mm^{-1} (see Figure 4.11). Based on this result, the IAEA's TRS-398[11] Code of Practice uses the following equation to calculate P_{repl} values in ^{60}Co beam for cylindrical chambers of

inner radius r_{cyl}:

$$P_{\text{repl}} = 1 - DF \times r_{cyl}, \tag{4.13}$$

where $DF = 0.004\ mm^{-1}$. For a Farmer chamber with $r_{cyl} = 3$ mm, Equation 4.13 gives a P_{repl} value of 0.988 in a ^{60}Co beam. This value is significantly different from that given in Table 2.3.

In the simulations of the experiments, in order to reproduce the experimental results, the calculated depth-ionization curves are normalized at d_{max}. However, it turns out this normalization procedure is unreasonable. When measuring the phantom dose with two chambers of different radii, r_1 and r_2, from the definition of P_{repl} and since P_{wall} and the stopping-power ratio are the same for both chambers, the following equation must hold:

$$J_{air,1} P_{\text{repl},1} = J_{air,2} P_{\text{repl},2}, \tag{4.14}$$

where $J_{air,i}$ is the absolute mass ionization reading from chamber i with radius r_i, and $P_{\text{repl,i}}$ is the replacement correction factor for chamber i which includes both the displacement effect and fluence perturbation. If there is no fluence perturbation at d_{max}, where no displacement effect exists as well, one has $P_{\text{repl},1} = P_{\text{repl},2} = 1$, which leads to $J_{air,1} = J_{air,2}$ at d_{max}; this is what Johansson et al used. For a cylindrical chamber of inner radius r, it is assumed that the value of P_{repl} can be expressed as:[11,70]

$$P_{\text{repl}}(r) = 1 - kr, \tag{4.15}$$

where k only depends on the radiation beam quality. For the two chambers of radii r_1 and r_2, if one uses P_{repl} values in Equation 4.15, substitutes them in Equation 4.14 and solves for k, one obtains:

$$k = \frac{1 - (J_{air,1}/J_{air,2})}{r_2 - (J_{air,1}/J_{air,2}) r_1}. \tag{4.16}$$

Since the ionization ratio $J_{air,1}/J_{air,2}$ is very close to 1, it is a good approximation to replace it by 1 in the denominator of Equation 4.16. Then one arrives at Equation 4.11 and k is just the displacement factor. Therefore Equation 4.11 is derived based on

Equations 4.14 and 4.15. Note that no normalization is done in the procedure. This suggests that the normalization at d_{max} of the measured depth-ionization curves in the experiments, which came from the assumption that the mass ionizations for different chambers are the same at d_{max}, is the cause of the difference between the measured and the Monte Carlo calculated P_{repl} values. To verify this, the P_{repl} values for a Farmer chamber calculated directly in a water phantom (see next section) are compared in Table 4.2 to those obtained from the simulation of Johansson et al's experiments with the displacement factors calculated from both the normalized (at d_{max}) and the un-normalized chamber responses. It is seen that the P_{repl} value for ^{60}Co beam calculated from the normalized chamber response (0.987) is very close to the value calculated by using Equation 4.13 above (0.988), that is, the simulation results "agree" with the measurements if the chamber responses are normalized at d_{max}. However, if the chamber responses are not normalized, the simulation results agree with P_{repl} values calculated directly using the Monte Carlo method in a water phantom. Although the experiments were done in a PMMA phantom, the difference between P_{repl} values in water and in PMMA for a Farmer chamber is less than 0.1%.

Figure 4.10 shows a 0.5% difference in the maximum mass ionization at d_{max} between the 3 mm chamber and the 7 mm chamber. The d_{max} value for these two chambers is also different: one at 0.50 cm and the other at 0.67 cm. The P_{repl} values for the 3 mm and 7 mm chambers at the corresponding d_{max} can be estimated from the figure as the ratio between the depth-ionization value and the cavity ionization data. This is actually the SPR method for calculating the values of P_{repl}. The values thus found are 0.998 and 0.996, respectively, and they are very close to the directly calculated P_{repl} values for the cylindrical cavity of the same size at 10 cm depth in a water phantom (see Figure 4.12 later). In Figure 4.10, the ionization value on the depth-ionization curve decreases by about 0.7% from 0.50 cm depth to 0.67 cm depth. This accounts for the

Table 4.2: Comparison of P_{repl} values for a Farmer chamber calculated directly in a water phantom to those obtained from the simulation of Johansson et al's experiments. For each beam, the displacement factors, DF, which are calculated from both the normalized and the un-normalized chamber responses, are calculated at different depths in a PMMA phantom and the average DF value is used to obtain the P_{repl} values in the PMMA phantom (1st and 2nd columns). The number in bracket represents one standard deviation statistical uncertainty in the last digit(s). From paper IV.

	P_{repl} from simulation of experiments		P_{repl} calculated in water
	with normalization	without normalization	
Co	0.9872(12)	0.9957(12)	0.9961(5)
4 MV	0.9902(11)	0.9955(11)	0.9966(6)
6 MV	0.9921(9)	0.9956(9)	0.9971(4)
18 MV	0.9934(8)	0.9976(8)	0.9971(4)

0.5% difference in the mass ionizations at d_{max} between the 3 mm chamber and the 7 mm chamber. The residual 0.2% is the difference in P_{repl} values for the two chambers. Thus the 0.5% difference in the maximum mass ionizations between the 3 mm and the 7 mm chambers comes from the attenuation of the depth-dose curve.

The results given above demonstrate that the normalization procedure for the depth-ionization curves measured by Johansson et al is not correct and it gives incorrect results in determining the displacement factors. Thus the interpretation of the measured values as P_{repl} for cylindrical chambers in photon beams is not correct in IAEA's TRS-398 Code of Practice, just as the values in TG-21 based on Cunningham and Sontag's values were based on an incorrect interpretation (see the previous section). It should be mentioned that Johansson et al also determined P_{repl} in a different approach by comparing depth-ionization curves measured by cylindrical chambers to that by a plane-parallel chamber whose front wall was used as the point of measurement. This resulted in an offset of the effective point of measurement (or radial displacement as called by Johansson et al[13]) ranging from 0.5 r to 0.9 r which was the basis of the 0.6 r offset

used by current dosimetry protocols for measuring depth-dose curves in photon beams. It is likely that these depth-ionization curves were also normalized at d_{max} when making the comparisons, so it was susceptible to the same problem. In addition, it was shown earlier that the effective point of measurement for plane-parallel chambers in photon beams is at the cavity center instead of the inner face of the front wall. This means that the offsets of the effective point of measurement are smaller than measured using this comparison technique. In other words, the $P_{\rm repl}$ values should be larger, closer to unity.

4.2.3 Calculated $P_{\rm repl}$ values

The cavity radius variation of $P_{\rm repl}$ values are calculated for cylindrical chambers of length 2 cm at a depth of 10 cm in a water phantom irradiated by both a ^{60}Co beam and an 18 MV photon beam. The beam quality dependences of $P_{\rm repl}$ for a Farmer chamber and for a larger cylindrical chamber (radius 5 mm) are also calculated for photon beams of energy ranging from ^{60}Co to 18 MV. Fano's theorem states that in a uniform field the electron fluence spectrum remains unchanged irrespective of the material density. In other words, under Fano conditions, the value of $P_{\rm repl}$ calculated by the LDW method should be unity. As a check, the $P_{\rm repl}$ values are calculated for cavities of 0.5, 3 and 5 mm radius at 10 cm depth in a ^{60}Co beam of 10×10 cm^2 at 100 cm SSD under Fano conditions, i.e. with primary photons regenerated after each interaction and scattered photons being discarded, and the results are tabulated in Table 4.3. The $P_{\rm repl}$ values are very close to unity under Fano conditions as expected.

The calculated radial dependence of $P_{\rm repl}$ values for the ^{60}Co beam and the 18 MV photon beams are shown in Figure 4.12. The solid lines are the fitted curves for the data points (see later). As expected from Equation 4.15, there is a linear relation between the

Table 4.3: Calculated P_{repl} values for different cavity radii in a ^{60}Co beam with and without Fano conditions (i.e. no attenuation, no scatter). Calculations are done with the LDW method for cylindrical cavities at a depth of 10 cm in a water phantom. The number in bracket represents one standard deviation statistical uncertainty in the last digit. From paper IV.

cavity radius	0.5 mm	3 mm	5 mm
P_{repl} (normal)	0.9979(7)	0.9961(5)	0.9939(4)
P_{repl} (Fano)	0.9991(7)	0.9993(6)	0.9997(6)

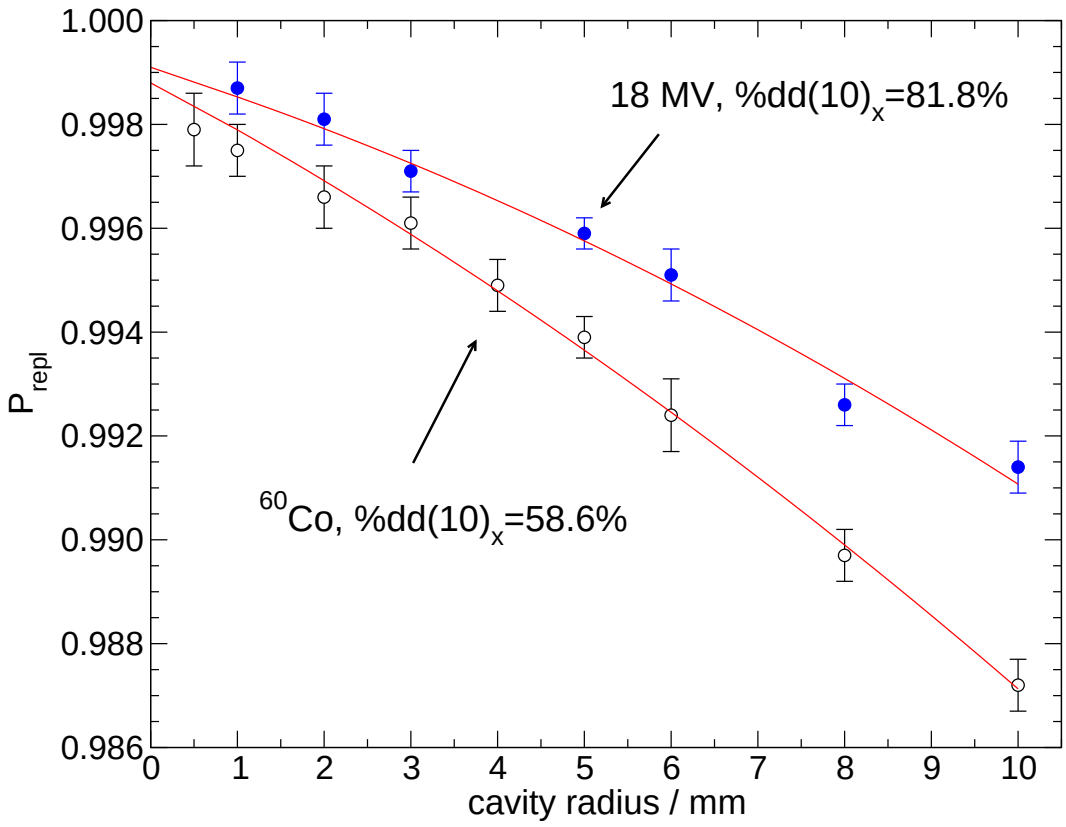

Figure 4.12: The P_{repl} values for cylindrical chambers (length 2 cm) at depth 10 cm in a water phantom as a function of chamber radius in a ^{60}Co beam and in an 18 MV linac beam. The solid lines are the values calculated by using Equation 4.17. From paper IV.

value of P_{repl} and the cavity radius r, with the possible exception of very small radius (< 1 mm). It is expected that $P_{\text{repl}} = 1$ for $r = 0$, although the fitted curves give values of 0.9988 and 0.9991 for the ^{60}Co beam and the 18 MV linac beam, respectively. However this is only a 0.1% difference which is about the level of uncertainty of the EGSnrc code system in calculating ion chamber responses[20] or about the systematic uncertainty in calculating P_{repl} values.

The results for the beam quality dependence of the P_{repl} values are shown in Figure 4.13 and compared to the TG-21 values. It is seen that there is essentially no beam quality dependence of the calculated P_{repl} values for the Farmer chamber; and it is notable that there is a significant difference between the calculated P_{repl} values and the TG-21 values which came from Cunningham and Sontag's experiment. For a Farmer chamber in a ^{60}Co beam, the TG-21 value is 0.4% lower than it should be. Practically, this means that a patient treated in the ^{60}Co beam calibrated with TG-21 using a Farmer chamber would be overdosed by 0.4%. For a high-energy photon beam (e.g. 18 MV), the discrepancy is still 0.2-0.3%. The difference is even larger for a larger chamber: as shown in Figure 4.13(a), the calculated P_{repl} values for the 5 mm radius chamber are at least 0.5% higher than the TG-21 values for all beam qualities. Since TG-21 used the individual P_{repl} values directly, it is more susceptible to the changes of these values.

On the other hand, one major benefit of the TG-51 dosimetry protocol (also the IAEA TRS-398 Code of Practice) is that only the ratios of various correction factors are concerned (Equation 1.11). Figure 4.14 shows the ratio of the value of P_{repl} for a beam of quality Q to that for a ^{60}Co beam as a function of the beam quality $\%\text{dd}(10)_x$. For a ^{60}Co beam calibrated with TG-51, the calibration result is always the same whichever value of P_{repl} is used. For both the Farmer chamber and the 5 mm radius chamber, the discrepancy between the ratio in this study and that used in TG-51 is at most 0.2% and this largest discrepancy is only for high-energy linac beams; in contrast for TG-21, the difference of the P_{repl} values for the 5 mm radius chamber is at least 0.5% for all

beam qualities. Also shown in Figure 4.14 are the values of the ratios used in the IAEA TRS-398 Code of Practice, based on the $P_{\rm repl}$ values used in TRS-398 [2]. For the Farmer chamber, the discrepancy between the ratio in this study and that used in TRS-398 can be as large as 0.5%; and it is even larger for a larger chamber. The original photon beam quality specifier for the TRS-398 data is TPR^{20}_{10}, and it has been converted to %dd(10)$_x$ by an empirical formula introduced for 'clinic-like' beams by Kalach and Rogers.[71]

Using the data in Figure 4.12 and Figure 4.13(b), one may derive an empirical formula for the values of $P_{\rm repl}$ for cylindrical chambers in photon beams as (with 0.1% uncertainty):

$$\begin{aligned} P_{\rm repl} &= 0.9974 - 0.00183\ r + 3.36\times10^{-5}\ \%dd(10)_x - 2.7\times10^{-5}\ r^2 \\ &\quad - 1.6\times10^{-7}\ (\%dd(10)_x)^2 + 1.58\times10^{-5}\ r\ \%dd(10)_x, \end{aligned} \tag{4.17}$$

where r is the cavity radius of the chamber in mm, and $\%dd(10)_x$ is the photon beam quality specifier, i.e. percent depth-dose at 10 cm depth, excluding electron contamination. The values of $P_{\rm repl}$ calculated from Equation 4.17 are shown in Figure 4.12 and Figure 4.13(b) as solid lines. If TPR^{20}_{10} is used as the photon beam quality specifier, a similar equation for heavily filtered 'clinic-like' beams is

$$\begin{aligned} P_{\rm repl} &= 1.0021 - 0.00188\ r - 0.0108\ TPR^{20}_{10} - 2.5\times10^{-5}\ r^2 \\ &\quad + 0.009\ (TPR^{20}_{10})^2 + 0.00169\ r\ TPR^{20}_{10}, \end{aligned} \tag{4.18}$$

where the values of TPR^{20}_{10} are obtained from $\%dd(10)_x$ by the empirical formula by Kalach and Rogers.[71] Equation 4.17 (4.18) is valid for cavities with a length of 2 cm, radii from 1 mm to 10 mm, and for %dd(10)$_x$ (TPR^{20}_{10}) values from 58% (0.57) to 82% (0.80).

Dosimetry protocols also assume $P_{\rm repl}$ does not depend upon the cavity length of cylindrical chambers in photon beams. To verify this assumption, the $P_{\rm repl}$ values

[2] Pedro Andreo, private communication, 2008

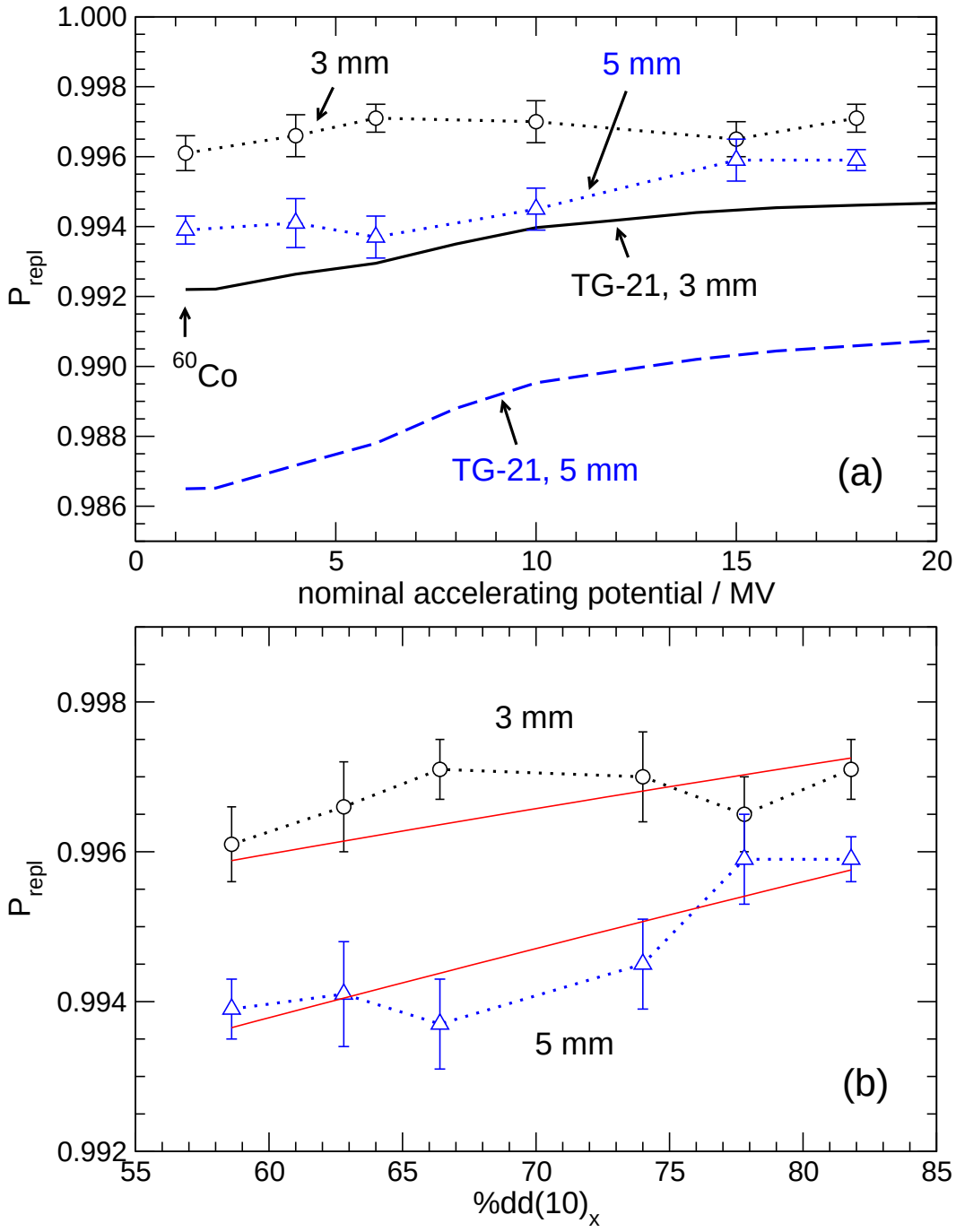

Figure 4.13: The calculated beam quality dependence of the replacement correction factor for a Farmer chamber and a larger cylindrical chamber (5 mm radius) in photon beams. In panel (a), nominal accelerating potential is used as beam quality specifier so as to compare to the values in TG-21. In panel (b), the photon component of the percent depth-dose at 10 cm ($\%dd(10)_x$) is the beam quality specifier. The solid lines in panel (b) are the values calculated by using Equation 4.17. From paper IV.

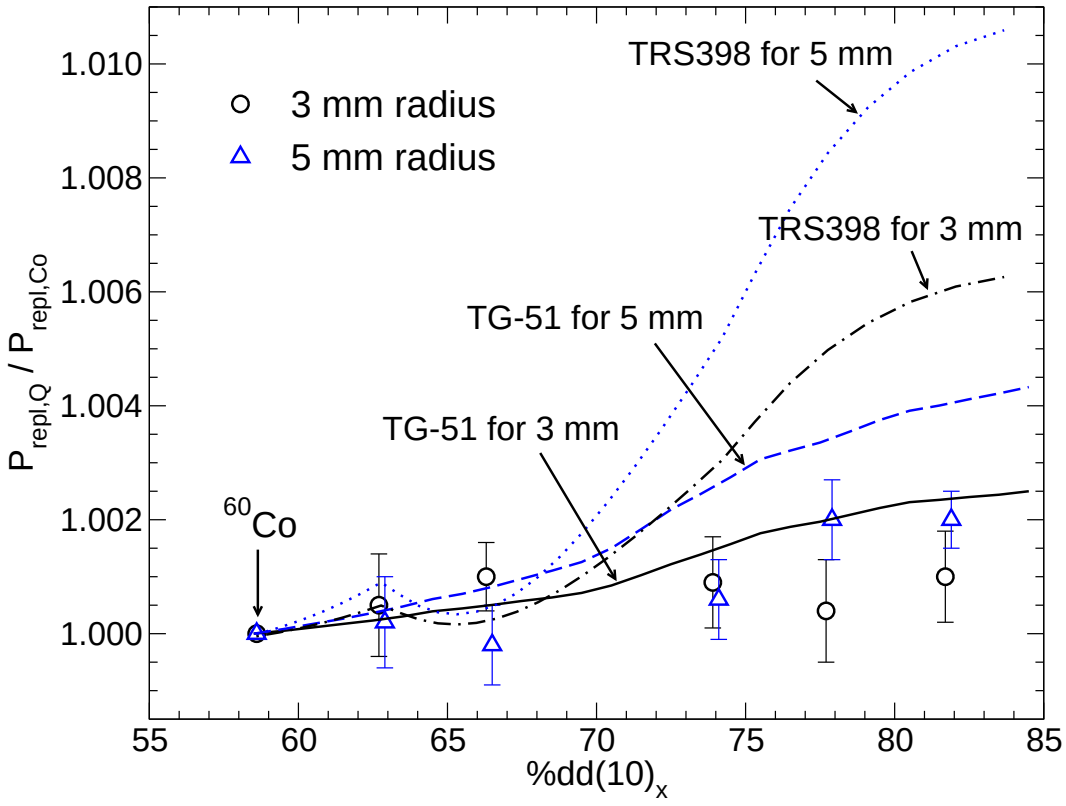

Figure 4.14: The beam quality dependence of the ratio of P_{repl} values for a beam of quality Q to that of ^{60}Co for both a Farmer-type chamber and a larger cylindrical chamber (5 mm radius). The symbols are calculated in this study and the lines are the values used in either TG-51(TG-21) or IAEA's TRS-398. From paper IV.

Table 4.4: Calculated P_{repl} values (LDW method) for different cavity lengths for an ion chamber with radius 3 mm at 5 cm depth in a ^{60}Co beam. From paper II.

cavity length (mm)	5	10	20
P_{repl}	0.9953±0.06%	0.9963±0.06%	0.9974±0.07%

are calculated in a ^{60}Co beam for a cylindrical cavity with a radius of 3 mm and cavity lengths of 0.5 cm, 1 cm, and 2 cm. The results in Table 4.4 indicate a 0.2% effect as the length varies from 0.5 cm to 2 cm. In contrast, for the case of the cylindrical chambers in low-energy (6 MeV) electron beams, the variation can be 0.5% (see Figure 4.8).

Chapter 5

Conclusions

In this study, four different methods of calculating the replacement correction factors, P_{repl}, by Monte Carlo simulation have been discussed. The challenge is to separate out the stopping-power ratio from the correction factors. Two of the methods are designated as 'direct' methods in the sense that the evaluation of the stopping-power ratio is not necessary. The study has shown that the systematic uncertainty of the 'direct' methods in calculating P_{repl} values is around 0.1-0.2% which comes from the ambiguous definition of the energy cutoff Δ used in the Spencer-Attix cavity theory. One of the direct methods, the low-density-water (LDW) method, is found most efficient in calculating P_{repl}; and the method is used extensively in this work to calculate P_{repl} values for all ion chambers in photon beams and for plane-parallel chambers in electron beams. The other direct method, the high-density-air (HDA) method, is found appropriate to calculate P_{repl} values for cylindrical thimble chambers in electron beams.

5.1 Electron beams

5.1.1 The effective point of measurement for ion chambers

The issue of the effective point of measurement for both plane-parallel chambers and cylindrical thimble chambers in electron beams is investigated. The effective point of measurement is one way of accounting for the gradient correction factor P_{gr}. It is found that there are two ways of determining the location of the effective point of measurement: one is to match the calculated depth-ionization curve obtained from a modeled chamber or a wall-less chamber cavity to a calculated depth-dose curve; the other is to match the primary electron fluence spectrum in the wall-less chamber cavity to that in phantom. For plane-parallel chambers, the effective point of measurement determined by the first method is generally not at the front-face of the chamber cavity which is obtained by matching the primary electron fluence spectrum, but shifted downstream towards the cavity center by 0.2 to 0.4 mm even for the wall-less cavities. The shift could be more than half a millimeter for a fully modeled plane-parallel chamber. This should not be ignored when measuring the depth-dose curves in electron beams using plane-parallel chambers. For cylindrical chambers, these two methods also give different positions of the effective point of measurement: the first gives a shift of 0.5 r which is in agreement with measurements for high-energy electron beams and is the same as the value currently used in major dosimetry protocols; the latter gives a shift of 0.8 r which is closer to the value predicted by a theoretical calculation which assumes no-scatter conditions. The results show that the shift of 0.8 r is more appropriate if the cylindrical chamber is to be considered as a Spencer-Attix cavity. As the water/air stopping power ratio changes with depth in a water phantom in electron beams, the difference of the two shifts (0.3 r) for cylindrical chambers leads to an incorrect evaluation of the water/air stopping power ratio at the point of measurement, thus resulting in a systematic error in determining the absorbed dose at the point.

5.1.2 P_{repl} values for cylindrical thimble chambers

P_{repl} can be separated into two non-unity factors: gradient correction P_{gr} and fluence correction P_{fl}. P_{gr} may also be accounted for by the effective point of measurement method. The gradient correction factor P_{gr} for a Farmer-type chamber as defined in the TG-51 dosimetry protocol may have an uncertainty of 0.3% for high-energy electron beams and more than 1% for low-energy electron beams. The values of P_{fl} are calculated and compared to measurements. Good agreement is obtained when the wall correction factors for plane-parallel chambers are taken into account. The results also show that the mean electron energy at depth is a good beam quality specifier for P_{fl}; and it is demonstrated that TG-51's adoption of the fluence correction factors for cylindrical chambers as a function of mean electron energy at depths is reasonably accurate. The dependences of the calculated P_{fl} values on the chamber radius and on the electron beam quality are investigated. An empirical formula is given for the P_{fl} values for 2 cm long cylindrical chambers when the cavity center is at the reference point in the phantom and the water/air stopping-power ratio is evaluated at the same point. The variation of the calculated P_{fl} on the cavity length is studied. For 6 mm diameter cavities the results show that there is a 0.6% change from 0.5 cm to 3.0 cm cavity length in a 6 MeV electron beams.

5.1.3 P_{repl} values for plane-parallel chambers

The P_{repl} value for the well-guarded NACP02 chamber at the reference depth in a 6 MeV electron beam is found to be 0.996. In an 18 MeV electron beam, P_{repl} is found to be very close to unity (within 0.1%) at both the reference depth and the depth of the maximum dose for this chamber. For the Roos chamber, the P_{repl} values at the reference depth are very close to unity (within 0.2%) in all electron beams. For the Markus chamber, the calculated P_{repl} values agree excellently with experiments when the most recent values

of the wall correction factors P_{wall} for plane-parallel chambers are taken into account.

5.2 Photon beams

5.2.1 P_{repl} values for cylindrical thimble chambers

Both Cunningham and Sontag's experiments and Johansson et al's experiments to determine the values of P_{repl} for cylindrical chambers in high-energy photon beams were simulated by the Monte Carlo method. The simulation results agree well with both sets of measurements if the experimental procedures of determining P_{repl} are followed. However, the values obtained this way differ from the values calculated by the direct Monte Carlo methods of calculating P_{repl}. Cunningham and Sontag interpreted their experiments as air kerma measurements instead of dose. Johansson et al normalized their depth-ionization curves at the depth of maximum ionization because they assumed there was a negligible perturbation effect at that depth which turns out not to be correct. Thus the interpretations of both Cunningham and Sontag's experimental values as P_{repl} in AAPM's dosimetry protocols and Johansson et al's experimental values as P_{repl} in IAEA's TRS-398 Code of Practice are not correct. Hence the most siginificant difference in photon beam dosimetry between the AAPM and the IAEA dosimetry protocols has been resolved. The values of P_{repl} for cylindrical chambers of different radii in various high-energy photon beams are calculated and an empirical formula is given. For Farmer chambers, there is essentially no beam quality dependence for P_{repl} values.

5.2.2 P_{repl} values for plane-parallel chambers

For an NACP02 chamber in a ^{60}Co photon beam, the value of P_{repl} is found to be 0.6% higher than unity, indicating the point of measurement might need to be at the center

of the cavity for the plane-parallel chamber as opposed to the assumptions in present dosimetry protocols.

For the BIPM graphite flat cavity ion chamber, it is found that the values of P_{repl} used in the past are not correct. The values used previously are smaller than they should be by about 1%. As this chamber was used to determine the value of W/e, this 1% discrepancy in the perturbation factor leads to a 1% over-estimation of the W/e value determined by using this chamber. The newly determined value is 33.61±0.3% J/C, if the stopping powers in ICRU Report 37 are used to evaluate the graphite/air stopping-power ratio. If the value of 86.8 eV for the mean excitation energy for graphite is used to evaluate the graphite stopping power, then the value obtained for W/e is 34.15±0.23% J/C. Direct measurements of W/e values for low-energy electrons have shown that W/e values approach a constant value very close to 34 J/C. It is reasonable to believe that the value of W/e remains constant for higher energies. This suggests that a higher I-value may be more appropriate than that used in ICRU Report 37. A change in the W/e value would also imply a change of the primary standards for the determination of air-kerma rate in ^{60}Co beams and low-energy X-ray beams.

5.3 Future work

For the replacement correction factor P_{repl}, now that accurate methods for calculating P_{repl} have been established, and given the previous work on P_{wall} factors, there is an opportunity to reassess many of the values used in routine clinical dosimetry. It is also very useful to verify these Monte Carlo calculations of P_{repl} values by experimental studies. These new sets of values, both P_{repl} and P_{wall}, may be used as the basis to develop more accurate dosimetry protocols in the future.

For the W/e value, although only the values determined by using the BIPM

graphite flat cavity ion chamber need to be changed by 1.2% according to this study, the current standard value of W/e must also be re-evaluated since this chamber's determination contributes a significant weight in the final adopted value of W/e; and many of the contributions of experimental determinations of W/e values are in fact correlated.

Appendix A

Effective point of measurement for chambers in electron beams

In Equation 1.16, the replacement correction factor P_{repl} is separated into two factors, one is the gradient correction P_{gr} and the other is the fluence correction P_{fl}. For cylindrical chamber in electron beams, because both P_{gr} and P_{fl} are non-unity the perturbation effect becomes much more complicated. In fact, the shape of the electron fluence spectrum is continuously changing with depth in electron beams. This may not be a significant issue for plane-parallel chambers as the front-face of the cavity is taken as the point of measurement (POM), i.e. the shape of the electron fluence spectrum in the cavity is very similar to that in phantom at the POM (Figure 2.8, page 32). For cylindrical chambers with the central axis as the POM, it does present a problem: the electron fluence spectrum in the cavity has a higher average energy than that in the phantom at the POM since the electrons lose less energy in the cavity's air. This difference in the electron fluence spectrum results in large values of P_{repl} even at d_{max} for low-energy beams (e.g. $\sim$0.96 for Farmer chambers in a 6 MeV beam) and huge correction factors in the dose fall-off region where the dose gradient is very large. Instead of using a depth-dependent value of P_{gr}, use of an effective point of measurement (EPOM) is

recommended for cylindrical chambers in electron beams in IAEA's TRS-398 dosimetry protocol. Current dosimetry protocols[10,11] shift the EPOM upstream by 0.5 r from the chamber center for a cylindrical chamber having a cavity radius r. This value of the shift originates mainly from the experimental work of Johansson et al.[13] Although AAPM's TG-51 protocol[10] uses P_{gr} explicitly (Equation 1.12, page 10), it is equivalent to the approach of a shift of EPOM as done in IAEA's Code of Practice,[11] if one ignores the difference of the other correction factors at these two depths. Experimentally, the EPOM of a cylindrical thimble chamber is determined by comparison of the percent depth-dose (PDD) measurements made by both a cylindrical chamber and a plane-parallel chamber with its front-face of the cavity as the measuring point. The PDD curve measured by the cylindrical chamber is shifted upstream in order to match the curve obtained by the plane-parallel chamber on the assumption that the plane-parallel chamber has no shift. The distance required is considered to be the shift s.

A.1 Effective point of measurement (EPOM)

A.1.1 Determining the EPOM from depth-ionization curves

Computationally, as the depth-dose curve can be calculated by the Monte Carlo simulation, one may find the EPOM not only for cylindrical chambers but also for plane-parallel chambers. The calculated depth-dose curves are converted to the fractional depth-ionization (FDI) curves (referred to as the standard FDI) by dividing by the water/air stopping-power ratio at each depth, in order to compare to the FDI curves obtained by the modeled chamber calculation at depths (referred to as the chamber FDI). Both the FDI curves are normalized to 1.0 at their respective maximum ionizations. The standard FDI has a spatial resolution of 0.5 mm (1 mm) for the 6 MeV (22 MeV) electron beam and the chamber FDI has a resolution of 1 mm (5 mm) for

the respective electron beams. To determine the distance of shift needed to match the chamber FDI to the standard FDI, the following procedure is followed: (1) a series of shift values, defined as negative if the shift is upstream towards the source, is applied to all the depths of the chamber FDI curve; (2) for each shift s, the values on the chamber FDI curve are multiplied by a scaling factor α, which can be obtained by minimizing the root-mean-square (RMS) difference between the two FDI curves. The RMS difference is calculated as

$$d_{RMS}(s) = \sqrt{\frac{\sum_i [p_s(z_i) - \alpha p_c(z_{0,i})]^2}{N}}, \tag{A.1}$$

where $p_s(z_i)$ and $p_c(z_{0,i})$ are the FDI values from the standard and chamber FDI curves, respectively; $z_i = z_{0,i} + s$ is the shifted depth and $z_{0,i}$ is the original chamber depth at which p_c is calculated. The values of $p_s(z_i)$ are generally calculated by linear interpolation of two neighboring dose grid points. Only values of both $p_s(z_i)$ and $p_c(z_{0,i})$ greater than 0.05 are used in the calculation. The total number of points on the curves used in the calculation is N (> 20 in this study). The value of d_{RMS} can be thought of as the average fractional difference (normalized to the maximum ionization) between the two FDI curves. The EPOM is obtained by finding the shift s that minimizes d_{RMS}.

The chambers simulated in this study are an NACP02 chamber, a Markus chamber with or without a protective cap, and an NE2571 Farmer chamber (3.14 mm radius). The modeled chamber is put at various depths in a water phantom irradiated by phase-space sources of either a 6 MeV or a 22 MeV electron beam. The phase-space files were generated from a BEAMnrc model for a 6 MeV Varian Clinac 2100C linac and a 22 MeV Elekta SL25 linac, both having a 100 cm source-surface-distance and a 10×10 cm^2 field size. For the NACP02 chamber, a calculation is also done for a thicker front window (50% increase for both the mylar and the graphite layer) since it is found experimentally that the front window of NACP02 chamber may be thicker than the manufacturer's specification.[72] In addition to the full chamber models, the wall-less air cavities (with guard ring) of the NACP02 and the Markus chambers are also studied; and wall-less

cylindrical air cavities of radii 1, 3.14, and 5 mm are investigated.

Plane-parallel chambers

Figure A.1 shows the minimized RMS difference as a function of the relative shift for an NACP02 chamber, an NACP02 chamber with a thicker front window, and a wall-less NACP02 chamber cavity. The minimum RMS difference occurs at a non-zero positive shift for both the real chamber and the wall-less cavity. For the wall-less cavity, the shift is about 0.2 mm for the two electron beams. The positive values of the shift suggest that there is significant number of electrons scattered from the cavity's distal face into the well-guarded cavity, shifting the effective measuring point from the front-face towards the center of the cavity. For the real chamber model, the shift is about 0.5 to 0.7 mm. The larger shift for the real model is because the chamber's front-wall is mainly made of a layer of graphite of thickness 0.5 mm, and, as the graphite density is 1.70 g/cm^3, it will make an extra 0.35 mm water equivalent material before the chamber cavity, compared to the wall-less cavity. The minimum RMS difference (in percentage) for the NACP02 chamber for the 22 MeV (6 MeV) beam is below 0.2% (0.3%) if the correct EPOM is taken into account, but it could be as large as 0.7% (2%) if the front-face is taken as the EPOM (i.e. no shift is used). For the chamber with the 50% thicker front window, the shift is a bit larger as expected. If no shift is used for the NACP02 chamber as is done in dosimetry protocols, the value of d_{RMS} for a NACP02 chamber with a thicker front window is 2.5% for the 6 MeV beam, which is 25% larger than that (2%) for a NACP02 chamber with the specified front-window thickness.

A similar study was performed for the Markus chamber and results are shown in Figure A.2. As the entrance window of the Markus chamber is very thin, there is not much difference in the shift between the real chamber and the wall-less cavity (only

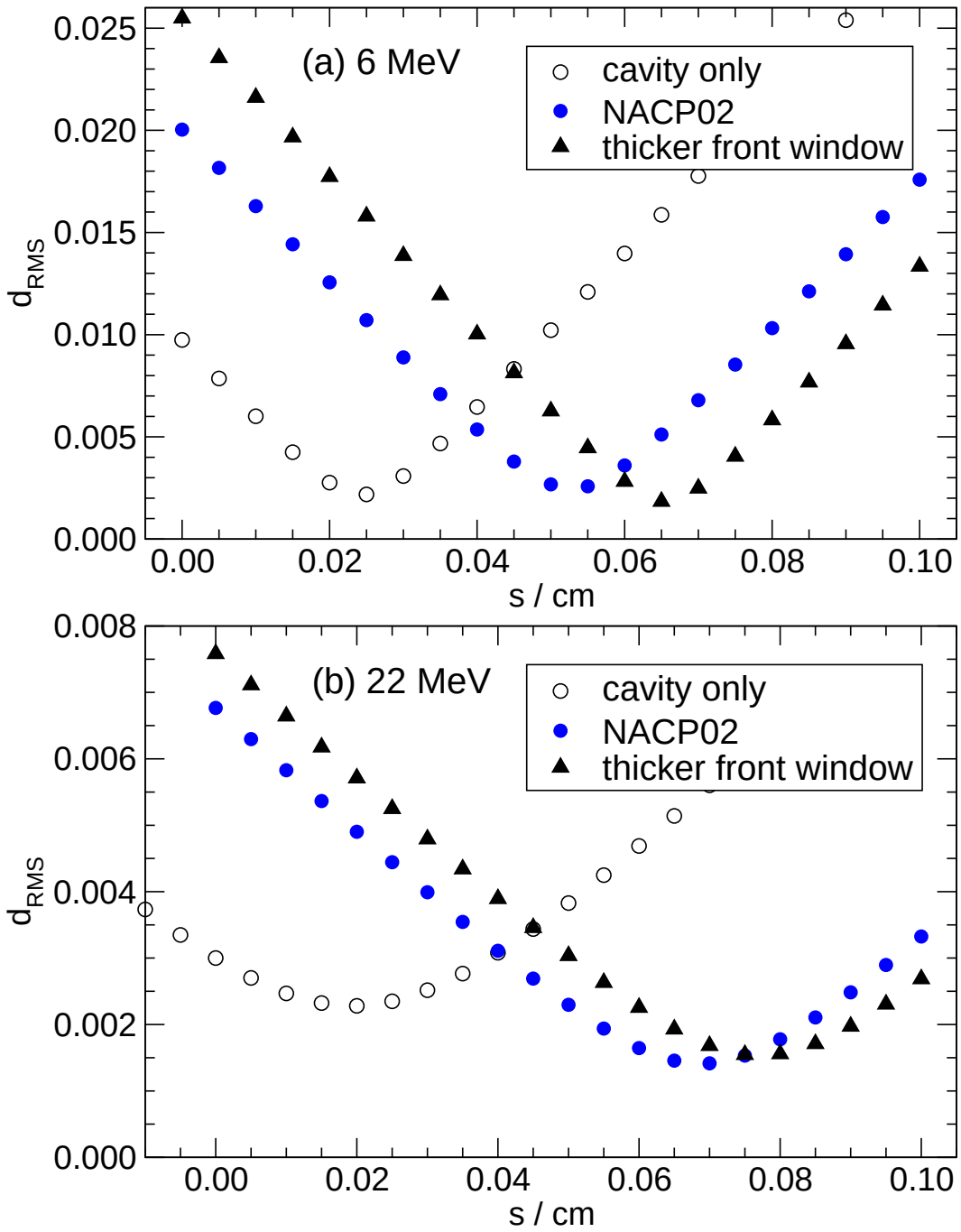

Figure A.1: Root-mean-square differences, d_{RMS}, between two FDI curves (calculated by equation A.1) as a function of relative shift, s, between the two curves in (a) a 6 MeV and (b) a 22 MeV electron beam. A full NACP02 chamber (solid circles), an NACP02 chamber with 50% thicker front window (solid triangles), and a wall-less chamber (i.e. guarded air cavity only, open circles) are modeled. From paper VI.

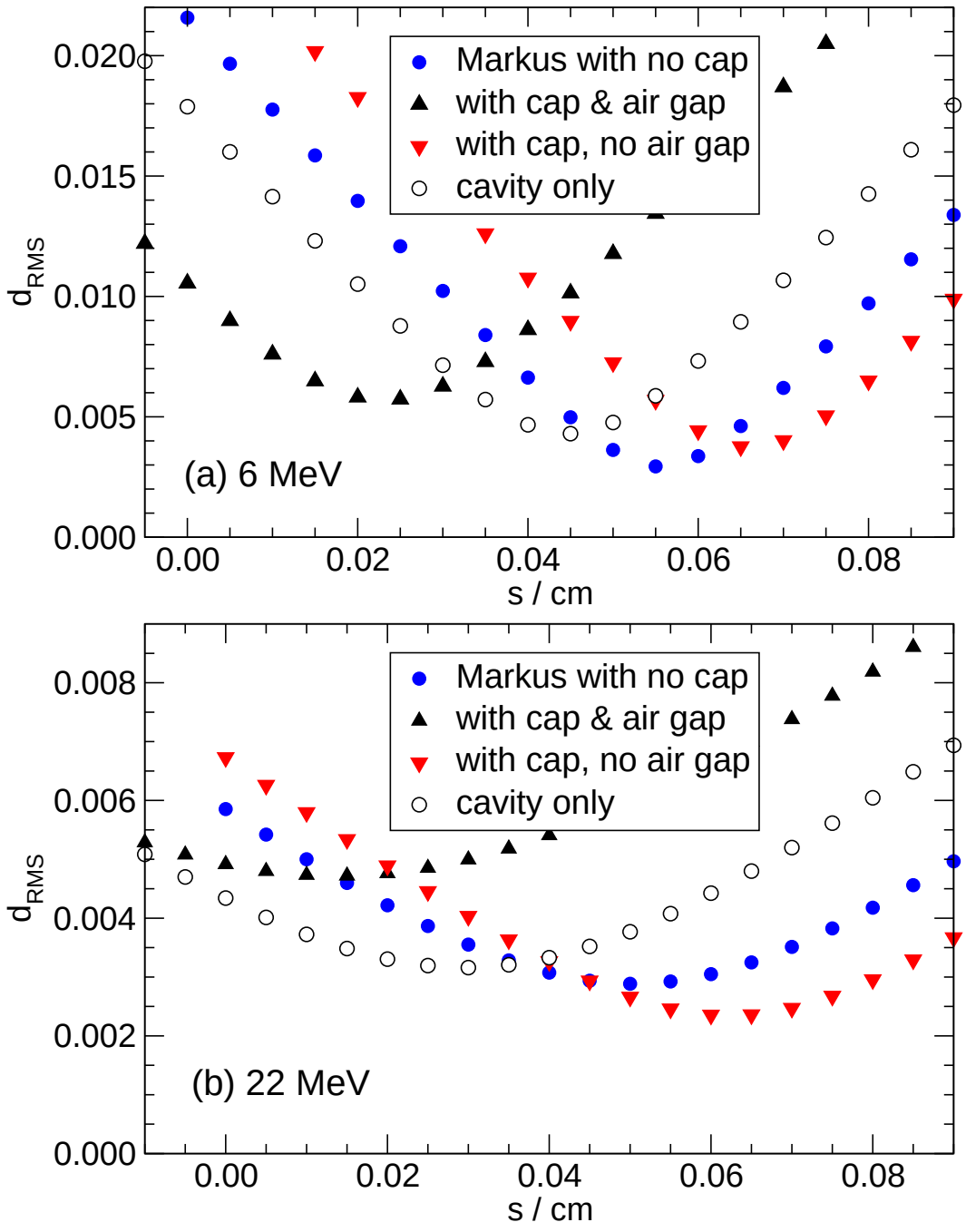

Figure A.2: Root-mean-square differences, d_{RMS}, between two FDI curves (calculated by equation A.1) as a function of relative shift, s, between the two curves in (a) a 6 MeV and (b) a 22 MeV electron beam. A Markus chamber (solid circles), the air cavity of the chamber (open circles), the Markus chamber with a protective cap and an air gap (up triangles), and the chamber with a protective cap but no air gap (down triangles) are modeled. From paper VI.

0.1-0.2 mm). For the wall-less cavity, the minimum RMS difference also occurs at a non-zero positive shift: 0.3 mm for the 22 MeV beam and 0.45 mm for the 6 MeV beam. The shifts are larger than those of the NACP02 chamber, especially for the low-energy beam. This is because the Markus chamber has a very narrow guard ring so that more electrons are coming from the side wall. When the Markus chamber is used in a water phantom, a water-proof protective cap made of PMMA is needed. The protective cap has a thickness of 0.87 mm and there is an air gap of 0.4 mm between the cap and the chamber. Figure A.2 also shows the influence of the protective cap, with or without the air gap, on the effective measuring point. When the protective cap is used, the entrance window thickness is dominated by the cap thickness. Since the PMMA density is 1.19 g/cm^3, when the cap is present but no air gap, one would expect the shift to be 0.19×0.87 mm = 0.16 mm larger than when no cap is present. This is exactly what Figure A.2 shows. If the air gap is present, it moves the effective measuring point back towards the front-face of the cavity since there is a lack of material before the cavity. Similar to the case of the NACP02 chamber, the Markus chamber would be less accurate if no shift is used. However, when a protective cap is used with the presence of an air gap, the accuracy would be improved if no shift is used ($s = 0$), although the minimum achieveable RMS difference becomes worse than when the EPOM is shifted appropriately (i.e. $s > 0$).

Another way to study the difference of the two FDI curves is to calculate the χ^2 values, similar to the method used by Kawrakow[73] in studying the EPOM for cylindrical chambers in photon beams. The minimum χ^2 per degree of freedom for the NACP02 chamber in water in both the 6 MeV and the 22 MeV beams is found to be 2.4 and 0.8, respectively, when the calculation uncertainty for the NACP02 FDI curves is about 0.2% (∼0.8% at depths close to the practical range).

IAEA's TRS-398 recognizes the importance of the front-window issue, as it says "the water equivalent thickness (in g cm^{-2}) of the chamber wall and any waterproofing

material should be taken into account when positioning the chamber at the point of interest. However, this is a very small effect and may be ignored in practice". So actually the front-face of the cavity for plane-parallel chambers is still used as the EPOM in the protocol. This presents a problem when comparing depth-dose curve measured by a plane-parallel chamber to that by a cylindrical chamber as the EPOM of plane-parallel chamber may need to be shifted by roughly half a millimeter.

Cylindrical chambers

Figure A.3 shows the minimized RMS difference as a function of the shift for the NE2571 chamber and for the cylindrical air cavities, for both the 6 MeV and the 22 MeV beams. The shift is given as a fraction of the cavity radius r of the respective chambers. The negative value of the shift means it is upstream towards the radiation source, i.e. the ion chamber measures a dose closer to the radiation source. The difference between the results for the NE2571 chamber and the air cavity of radius 3.14 mm is due to the chamber wall effect and it is small for high-energy electron beams. For the 22 MeV beam, the RMS difference has a minimum value around a shift of 0.46 r for the NE2571 chamber and a shift of 0.51 r for all the air cavities. This is almost the same as the value of 0.5 r recommended by dosimetry protocols.[10,11] For the 6 MeV beam, the RMS difference reaches a minimum at a shift of about 0.33 r and 0.41 r for the chamber and all the air cavities, respectively. The values are less than the recommendation of dosimetry protocols. This difference is reasonable as the scattering effect is stronger for lower-energy beams so the EPOM is closer to the center of the chamber. One more point from Figure A.3 is that the minimum RMS difference for the high-energy beam ($\sim$0.4%) is smaller than in the low-energy beam ($\sim$1%), i.e. the cylindrical chamber is less appropriate for use in low-energy electron beams except for very small radius cavity. If the 0.5 r shift is also used for low-energy beams (e.g. 6 MeV), then the RMS difference

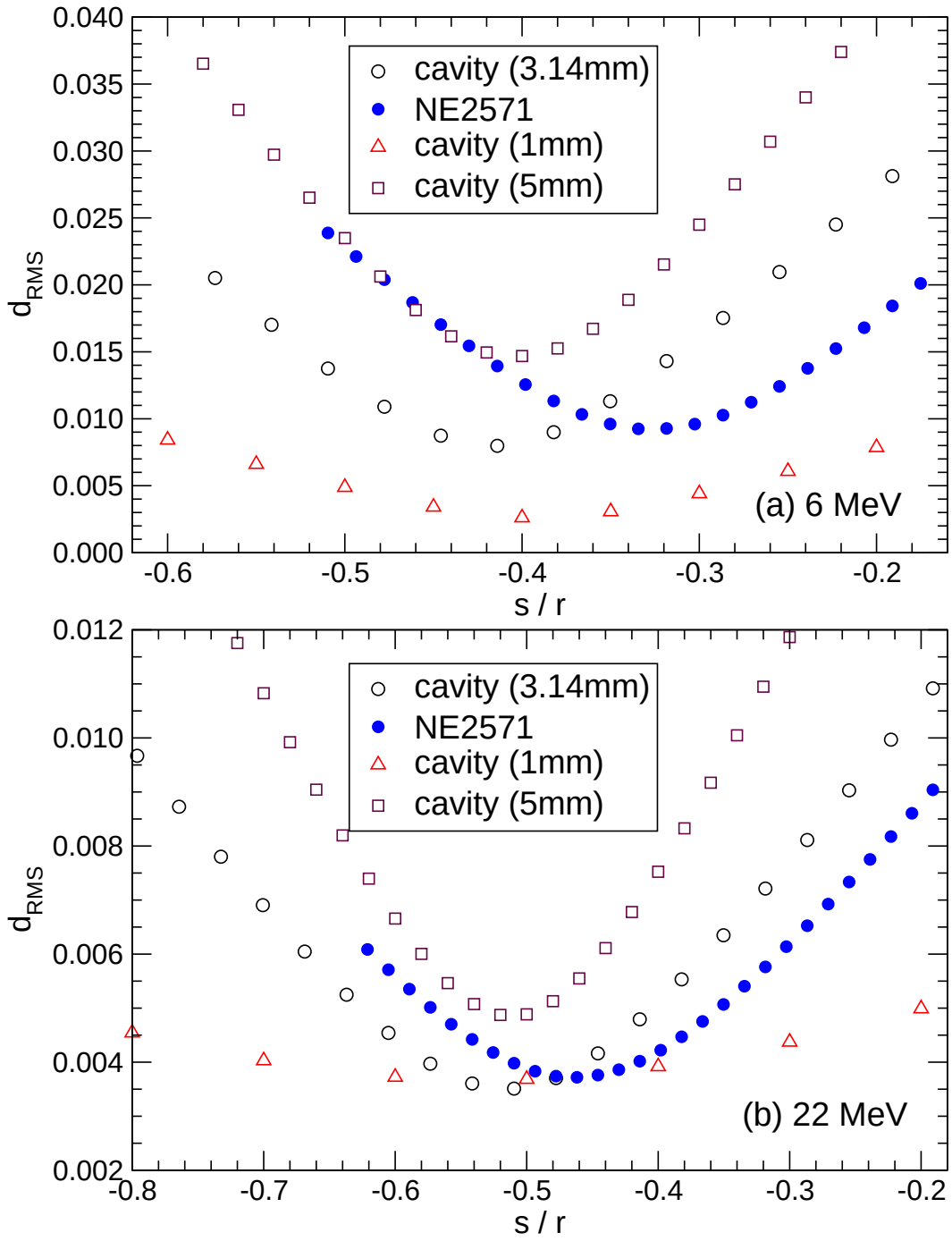

Figure A.3: Root-mean-square differences, d_{RMS}, between two FDI curves (calculated by equation A.1) as a function of relative shift, s, between the two curves in (a) a 6 MeV and (b) a 22 MeV electron beam. An NE2571 chamber (solid circles) and three cylindrical air cavities of different radii (1, 3.14, and 5 mm) and length 2 cm are modeled. The shift is in units of the air cavity radius. From paper VI.

could be at least 2% for the NE2571 chamber, even though the minimum RMS is 1%. The minimum χ^2 per degree of freedom for the NE2571 chamber in water in both the 6 MeV and the 22 MeV beams is found to be 67 and 7, respectively, when the calculation uncertainty for the NE2571 FDI curves is about 0.15% (∼0.5% at depths close to the practical range). The very large χ^2 value for 6 MeV electron beam indicates again that with cylindrical chambers, a simple EPOM correction is not enough to produce a reliable dosimeter, especially for low-energy electron beams.

A.1.2 Determining the EPOM from electron fluence spectra

For cylindrical thimble chambers with the central axis at depth z, the point of measurement (POM), there is a lack of phantom material upstream from the central axis of the chamber. It is expected that the electron fluence spectrum in the chamber cavity is different from that at depth z in the phantom without the presence of the chamber. Figure A.4 shows the calculated spectra at d_{ref} and R_{50} in a water phantom and in a

Farmer-type chamber cavity for both (a) a 6 MeV and (b) an 18 MeV electron beam. As expected, the peak in the spectrum in the cavity is shifted to higher energy relative to that in the phantom. The energy shift is about 0.5 MeV and is not very sensitive to the depth or the electron beam energy. It is reasonable to believe that at a certain point in the phantom upstream from the POM (z) in the phantom, the peak in the spectrum should match that in the cavity at the depth z. To find that point, i.e. the shift s, the spectrum in the phantom is calculated for a variety of depths upstream from the depth z and compared to the spectrum in the cavity at the depth z. The shift is found by matching the primary electron peaks in the spectrum and its value found in this way for both a 3 mm radius (Farmer-type) chamber and a 5 mm radius chamber is 0.8 r, where r is the radius of the cylindrical cavity. This shift is different from the value obtained in the previous section or from the shift of 0.5 r recommended by

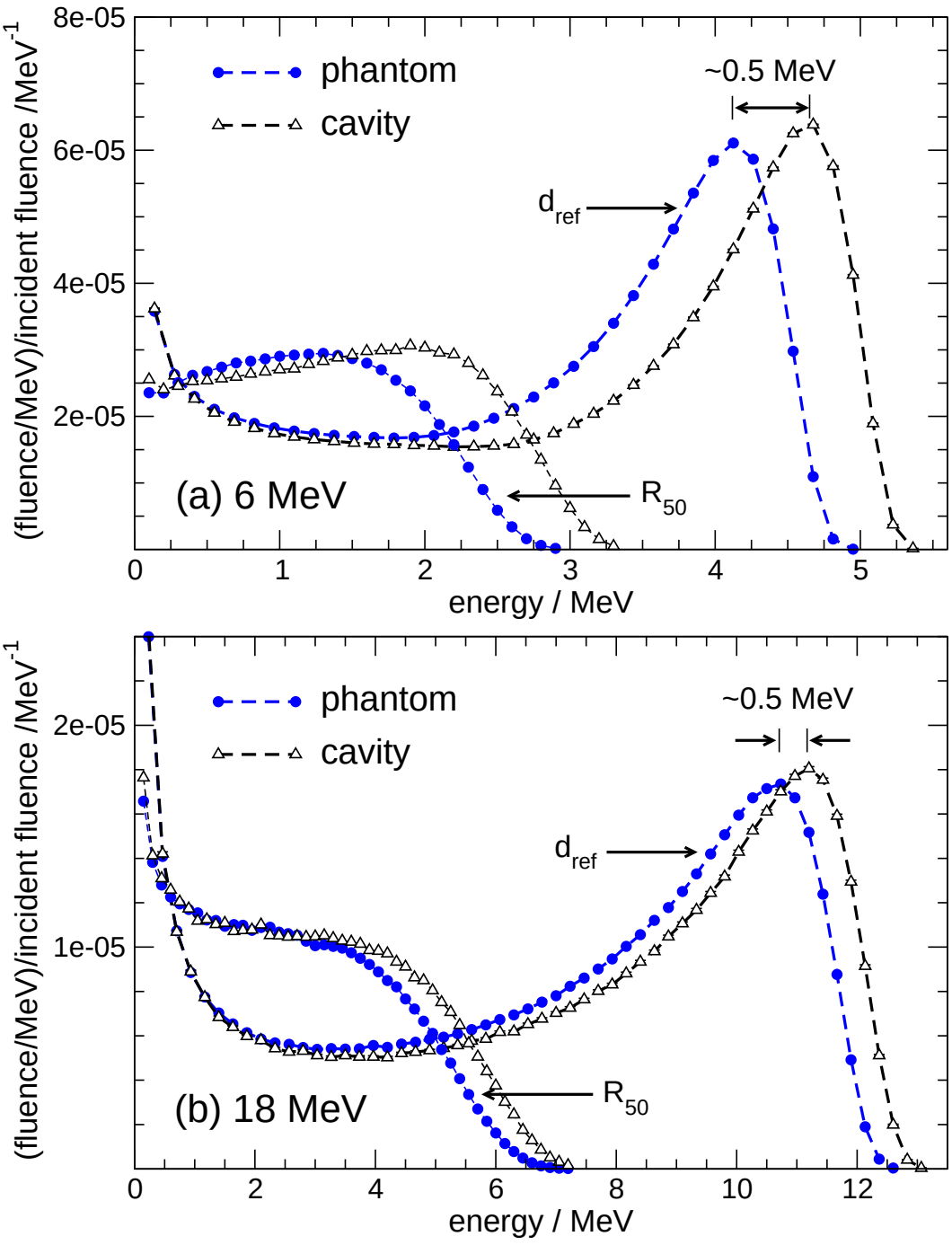

Figure A.4: Electron fluence spectra in a Farmer chamber cavity (open triangles) and in a water phantom (filled circles) at both d_{ref} and R_{50} in (a) a 6 MeV and, (b) an 18 MeV electron beams. From paper VI.

dosimetry protocols, since the mechanism of obtaining it is quite different: the current method only considers the primary electron fluence while the previous method takes into account the whole depth-ionization curve. However, it is very close to the theoretical value of $8\ r/3\pi = 0.85\ r$ calculated for cylindrical chambers in electron beams under the condition of no scattering as originally derived by Skaggs[74] and quoted by Nahum.[32]

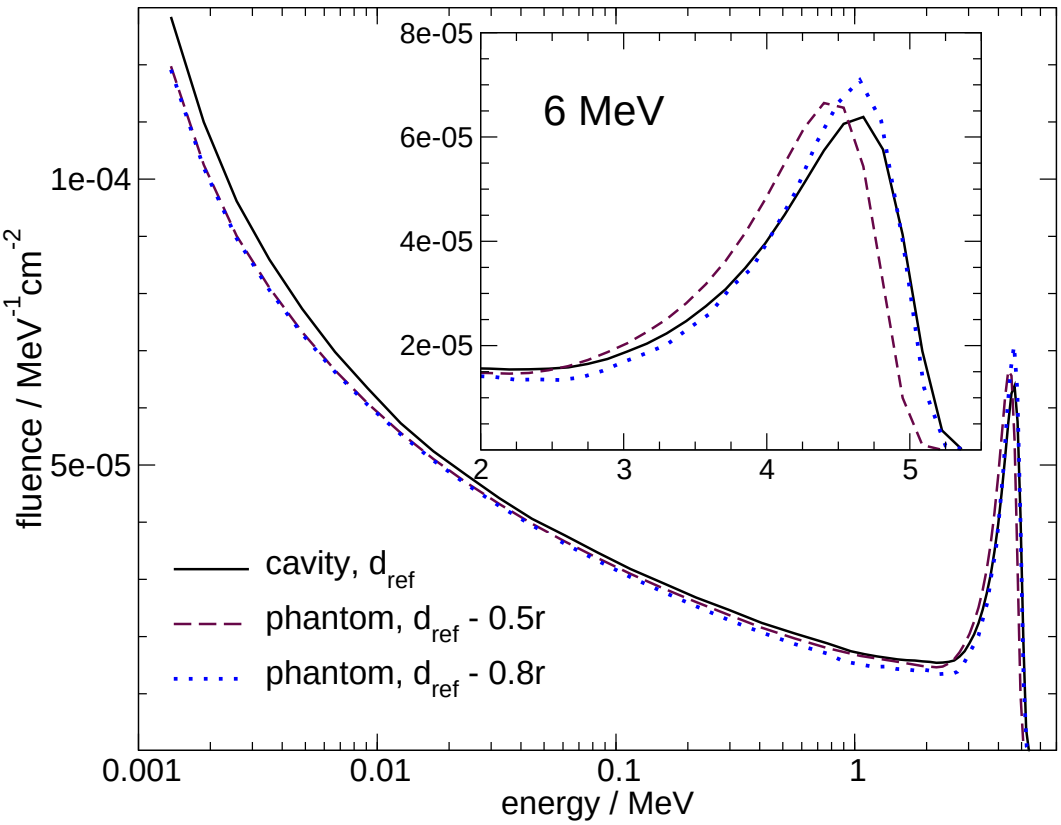

Figure A.5: Electron fluence spectra in the Farmer chamber cavity at d_{ref} and in the phantom at $d_{ref} - 0.5\ r$ and $d_{ref} - 0.8\ r$ in a 6 MeV electron beam. The inset shows, on a linear scale, the energy range near the peak of the primary electrons. From paper VI.

Figure A.5 and Figure A.6 show the spectrum in the Farmer chamber cavity at d_{ref} compared to those at depths $d_{ref} - 0.5\ r$ and $d_{ref} - 0.8\ r$ in the phantom for the 6 MeV and the 18 MeV electron beams, respectively. For the high-energy electron beam, the peak in the spectrum at $d_{ref} - 0.8\ r$ in the phantom matches that in the cavity at

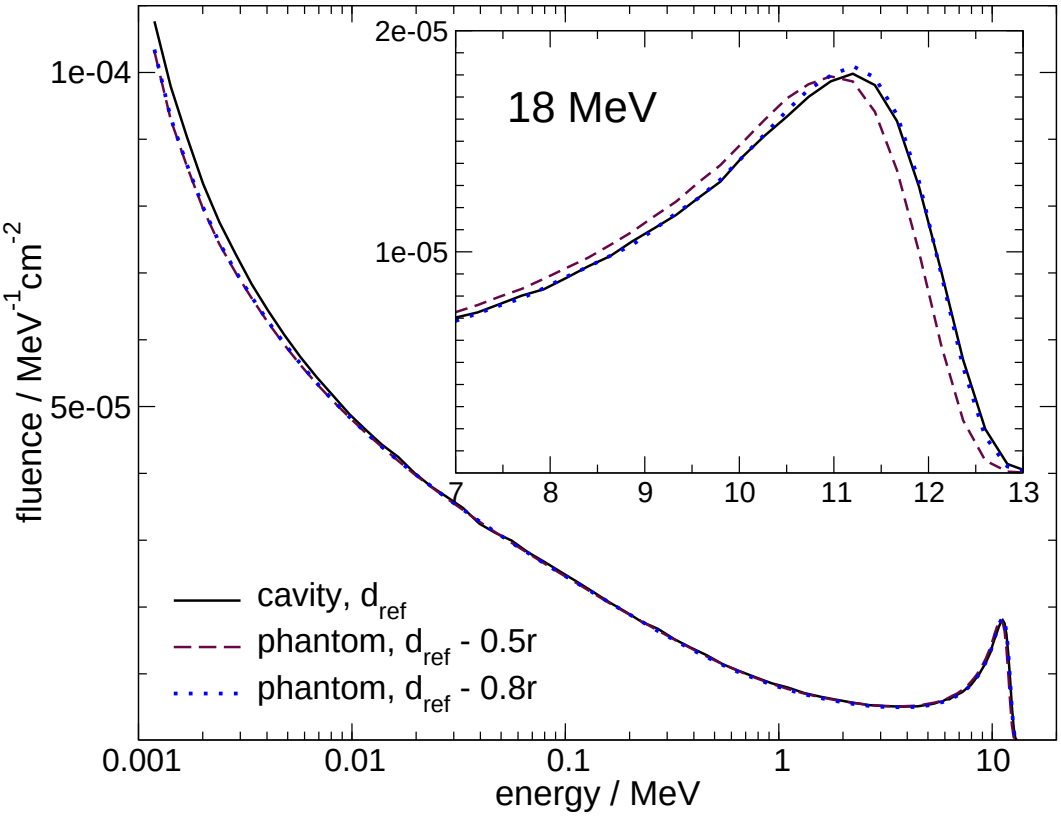

Figure A.6: Electron fluence spectra in the Farmer chamber cavity at d_{ref} and in the phantom at $d_{ref} - 0.5\ r$ and $d_{ref} - 0.8\ r$ in an 18 MeV electron beam. The inset shows, on a linear scale, the energy range near the peak of primary electrons. From paper VI.

d_{ref} excellently (Figure A.6 and the inset). For the low-energy electron beam the same shift also gives a match of the peaks in the spectrum, although the shape is not ideally matched (Figure A.5 and the inset). There is a clear mismatch if the shift is 0.5 r for both electron beams. The same results are obtained for the 5 mm radius cylindrical chamber. It is interesting to note that the combination of the energy shift (0.5 MeV for Farmer chamber) and the distance shift (0.8×0.3 cm = 0.24 cm for Farmer chamber) studied above implies an electron stopping power of 0.5 MeV/0.24 cm = 2.1 MeV/cm, which is consistent with the rule-of-thumb stopping power of 2 MeV/cm for high-energy electrons in water.

For plane-parallel chambers, as the front-face of the cavity is the EPOM, the match of the primary electron fluence spectra is mainly determined by the thickness of the chamber's front-window. For a wall-less pancake shaped air cavity, one would expect the spectrum to be the same as that in the phantom. Figure A.7 shows the comparison of the spectra in the phantom, in the NACP02 chamber, and in the wall-less NACP02 chamber cavity. The peak of the primary spectrum in the NACP02 chamber is shifted to a lower energy compared to that in the phantom due to the extra 0.35 mm water-equivalent material before the cavity as estimated in the previous subsection. In determining the EPOM for plane-parallel chambers by matching the electron fluence spectra, the wall effect should be separated out, i.e. the spectrum in the phantom should be matched to that in the wall-less cavity as done for cylindrical chambers. This leads to 0 shift according to Figure A.7, and it is what is currently used in dosimetry protocols.

Hence there are actually two ways of determining the EPOM for ion chambers in electron beams: either matching the primary electron fluence spectra or matching the depth-dose curves. Unfortunately, these two methods give different shifts for the effective point of measurement. If matching the depth-dose curves, for cylindrical chambers, the

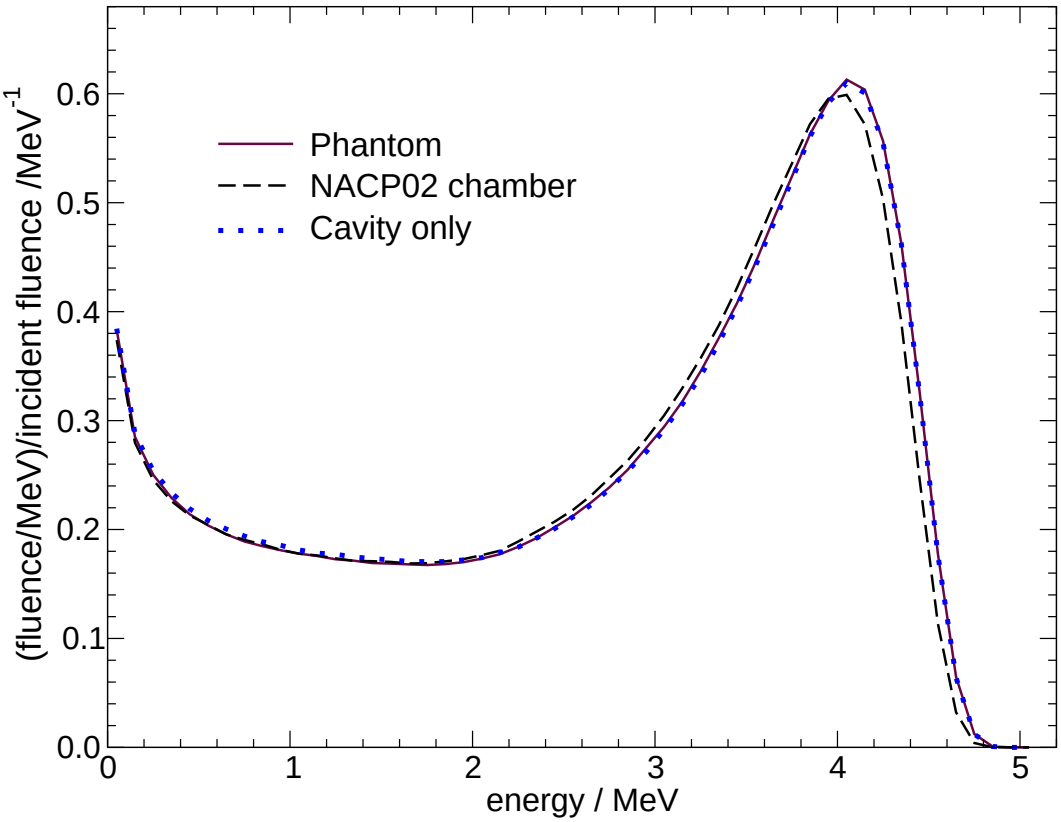

Figure A.7: Electron fluence spectrum in the phantom at d_{ref} in a 6 MeV electron beam, compared to those in the NACP02 chamber and the wall-less chamber cavity with the front-face of the cavity located at d_{ref}. From paper VI.

shift is in the range 0.4 r to 0.5 r upstream from the cavity center depending on the radiation quality but not on cavity radius; for plane-parallel chambers, the shift is in the range 0.2 to 0.4 mm downstream from the cavity's front-face depending on the radiation quality and the cavity geometry. If matching the primary electron fluence spectra, for cylindrical chambers, the shift is 0.8 r upstream from the cavity center; for plane-parallel chambers, no shift is necessary.

A.2 Selecting the stopping-power ratio

From the results in the previous section, for cylindrical chambers, since the electron fluence spectrum in the cavity at depth z is very different from that in phantom at the same depth, the water/air stopping-power ratio cannot be simply evaluated at depth z in phantom. Rather, the electron fluence spectrum in a cylindrical chamber cavity of radius r is similar to that in the phantom at a point 0.8 r upstream from the chamber's central axis. Hence it is a reasonable approximation to assume the water/air stopping-power ratio calculated for the electron fluence spectrum in the cavity is the same as that evaluated in phantom at depth $z - 0.8\,r$. Figure A.8 shows the water/air stopping-power ratio as a function of depth for a 6 MeV and an 18 MeV electron beams. The gradients of the two lines are about 0.30%/mm and 0.16%/mm, respectively; this means for a shift of 0.8 $r = 2.4$ mm (i.e. for a Farmer chamber), the changes in the water/air stopping-power ratio are 0.72% and 0.38% for the 6 and 18 MeV beams, respectively.

As a way of verifying the applicability of the Spencer-Attix cavity theory as done in Section 2.5.2, the air in a Farmer chamber cavity is replaced by the LDW material. Since the density of the LDW is the same as air, and since water and air have similar effective atomic number, the electron fluence spectrum in the LDW-filled cavity will be very close to that in the air-filled cavity. If the Farmer chamber cavity behaves like an

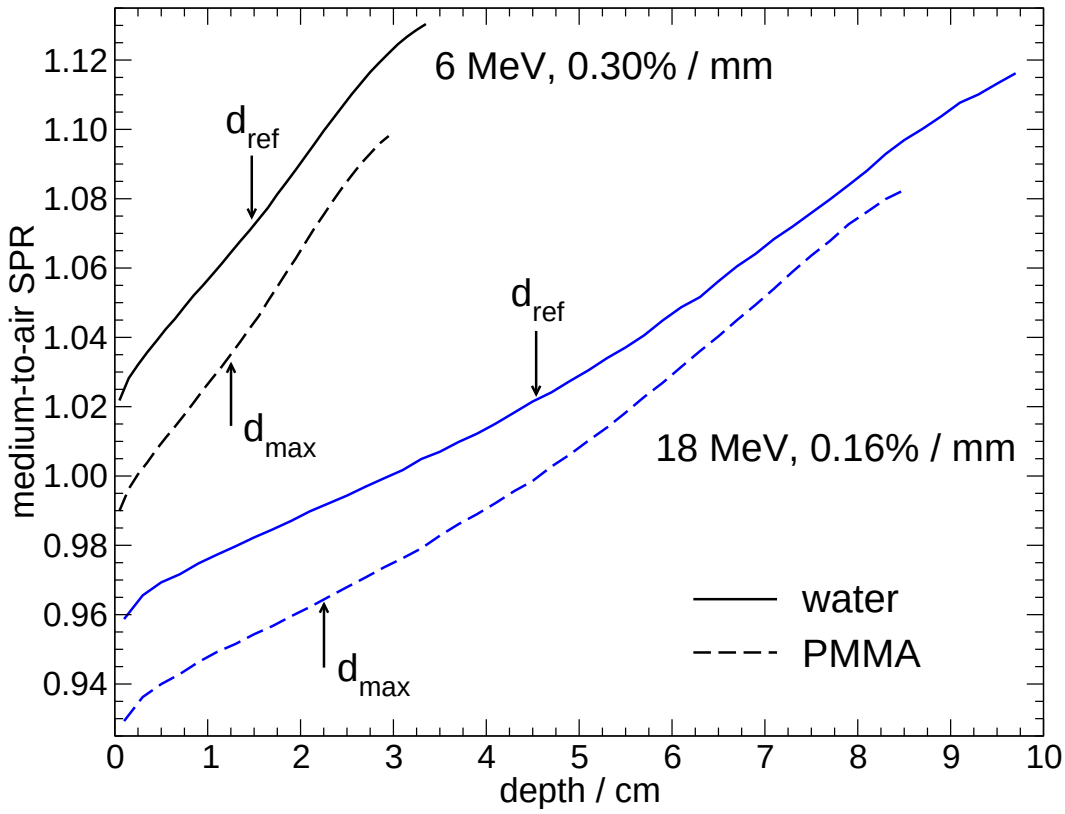

Figure A.8: The medium-to-air stopping-power ratio vs depth for the 6 MeV and the 18 MeV electron beams. The medium is either water (solid line) or PMMA (dashed line). From paper VI.

ideal Spencer-Attix cavity (i.e. with no gradient or fluence corrections needed), then the ratio of the dose in the cavity filled with LDW to that in the cavity filled with air must be the same as the water/air stopping-power ratio evaluated at the point of measurement in the phantom. To investigate this, this dose ratio is calculated at various depths in both the 6 MeV and the 18 MeV electron beams and the results are divided by the water/air stopping-power ratio (with $\Delta = 10$ keV) at the corresponding depths and at the depths shifted upstream by 0.5 r and 0.8 r. The results are shown in Figure A.9. It is seen that, without the shift, the cavity dose ratio at d_{ref} deviates from the water/air stopping-power ratio by about 0.7% and 0.3% for the 6 MeV and 18 MeV electron beams, respectively. This means the cylindrical cavity deviates significantly from an ideal Spencer-Attix cavity. However, the cavity dose ratio is very close to the water/air stopping-power ratio evaluated at $z' = z - 0.8\,r$ for both the electron beams especially at d_{ref} which is consistent with the spectra looking similar (Figure A.5 and A.6). A shift of 0.5 r, which is the dosimetry protocol recommendation, is much better than no shift but not as good as a shift of 0.8 r obtained by matching the primary electron fluence spectrum; there still remains a discrepancy of at least 0.2% at d_{ref} for a 0.5 r shift in the 6 MeV beam.

In the AAPM's dosimetry protocols,[7,10] the point of measurement z is at the center of cylindrical chamber cavities and the water/air SPR is also evaluated at this point. In TG-51,[10] a correction factor is explicitly used to account for the gradient effect. In the IAEA's TRS-398,[11] the point of measurement is at the reference point at which the water/air SPR is evaluated and at which the dose is measured by shifting the cylindrical chamber downstream by an amount $s = 0.5\,r$, i.e. at a depth $z + 0.5\,r$. Thus the gradient effect is accounted for by the chamber shift. In both situations, the size of the shift, $s = 0.5\,r$, is different from that determined by matching the shapes of the primary electron fluence spectra, $s = 0.8\,r$. According to Figure A.9, this leads

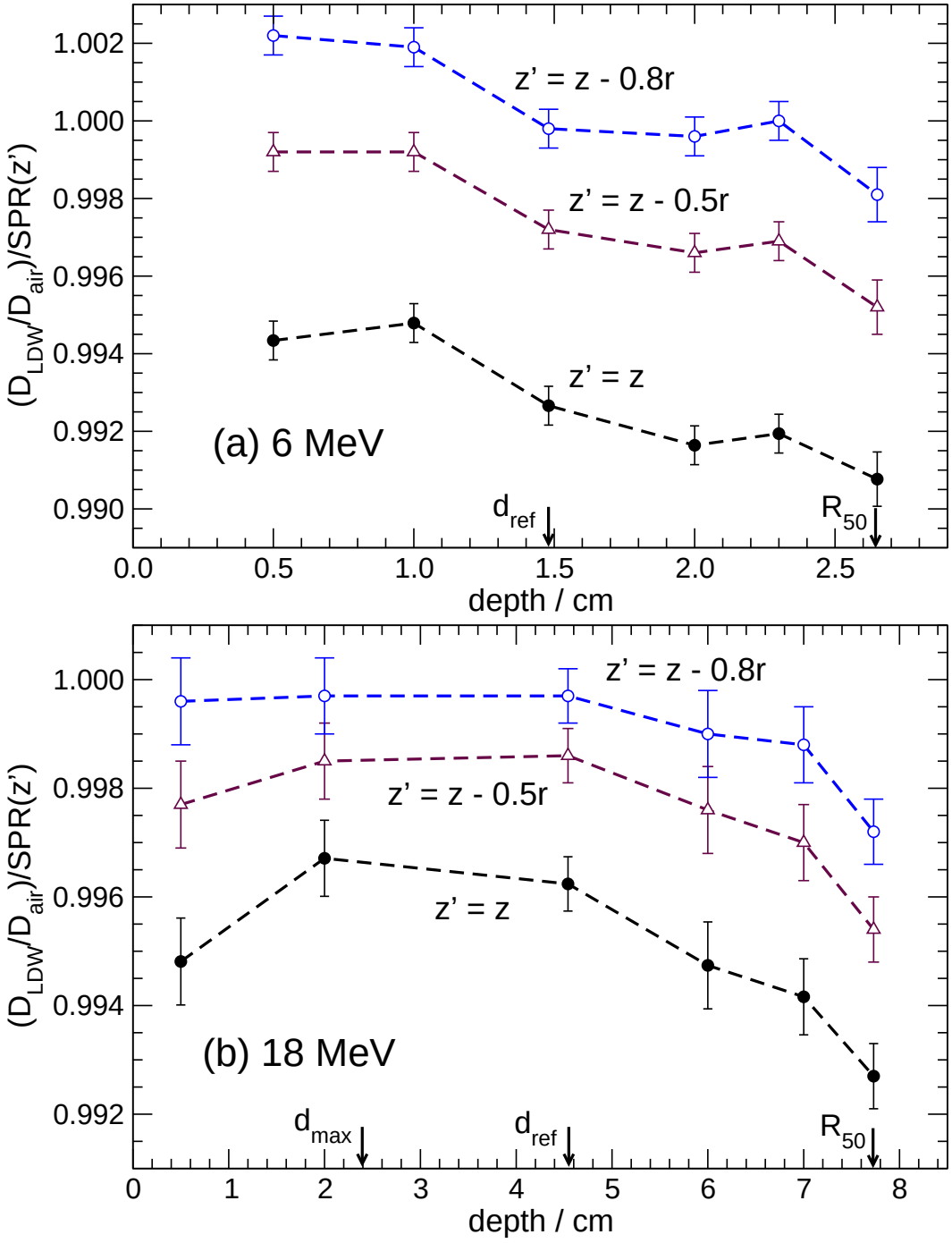

Figure A.9: The quotient of the dose ratio of the LDW cavity to air cavity for a Farmer chamber's cavity centered at z to the water/air stopping-power ratio (Δ=10 keV) evaluated at depths $z' = z$, $z - 0.5\ r$ or $z - 0.8\ r$, as a function of depth, z, in (a) a 6 MeV and (b) an 18 MeV electron beam. From paper VI.

to a systematic error in determining the dose at the reference depth z if the chamber is considered as a Spencer-Attix cavity. For plane-parallel chambers, there is no such a problem of selecting the correct stopping-power ratio, since the shift is determined to be $s = 0$ by matching the primary electron fluence spectra.

Appendix B

Response of an electron diode detector

[1] Silicon semiconductor diodes have much smaller sizes than ion chambers with the same sensitivities due to the high density of silicon (compared to air) and the low energy (∼3.6 eV) needed to produce an ion pair. They have been widely employed in clinical radiotherapy practice for years: either as depth-dose and dose-profile measuring devices or as quality assurance tools for in-vivo dosimetry.[75,76] It is well known that dosimetry diodes measure almost the same depth-dose distributions in both photon and electron beams as ion chambers.[77–85] It is empirically assumed that the diode response is independent of depth in a phantom. In this study, the EGSnrc user-code CSnrc is used to model a silicon diode and to study its response, i.e. dose to silicon per unit dose to water at the same point, with respect to depth in a water phantom in electron beams. In addition, the beam quality and the field-size dependences of the response of the diode model are investigated.

[1] This appendix summarizes a separate investigation done at the start of my PhD.

B.1 Simulation of a Si diode detector

The electric charge generated by a silicon diode detector is assumed to be proportional to the energy deposited in the sensitive volume or active region of the Si crystal of the diode. The model of the Si diode detector studied in this work is shown in Figure B.1 and is meant to correspond to the Scanditronix-Wellhöfer EFD electron field detector. The geometrical and material data are mainly based on the information in the paper by Rikner and Grusell.[86] During this work, more detailed data were obtained from the diode manufacturer and they lead to a model shown in Figure B.2 which represents more accurately what is being sold today. The active region size is the same for both the models. The major differences between the two models are: (1) the overall Si chip size is larger for Model 2 and the sensitive region is surrounded by a ring of Si material as the diameter of the chip size is 2.5 mm as opposed to 2.0 mm in Model 1; (2) in Model 2 the total Si chip thickness is 0.5 mm while in Model 1 the thickness of Si behind the active region is 0.5 mm; (3) the thickness of the aluminum contact is so small (<1 μm) that it is removed in Model 2. The diode is cylindrically shaped with the Si chip enclosed by epoxy resin. The active region of the Si chip is the first 0.06 mm layer of the silicon crystal. Before the Si chip there is a thin layer (0.02 mm) of aluminum in Model 1. Between the aluminum and the active region, there is a dead layer of silicon material. The thickness of the dead layer for diffused junction detectors is up to about 2 μm and for other types of diode detectors it is even thinner.[87] According to the manufacturer, the thickness of the dead layer for the Scanditronix p-type EFD detector is about 3 μm. This is completely negligible in the model. The modeled diode is put on the central axis of a cylindrically symmetric water phantom of radius 20 cm and depth 30 cm. The depth of the diode is determined by the depth of the center of the active region. The front face of the diode is always perpendicular to the incident direction of a parallel circular electron beam with a radius of 5.6 cm (10×10 cm^2 equivalent).

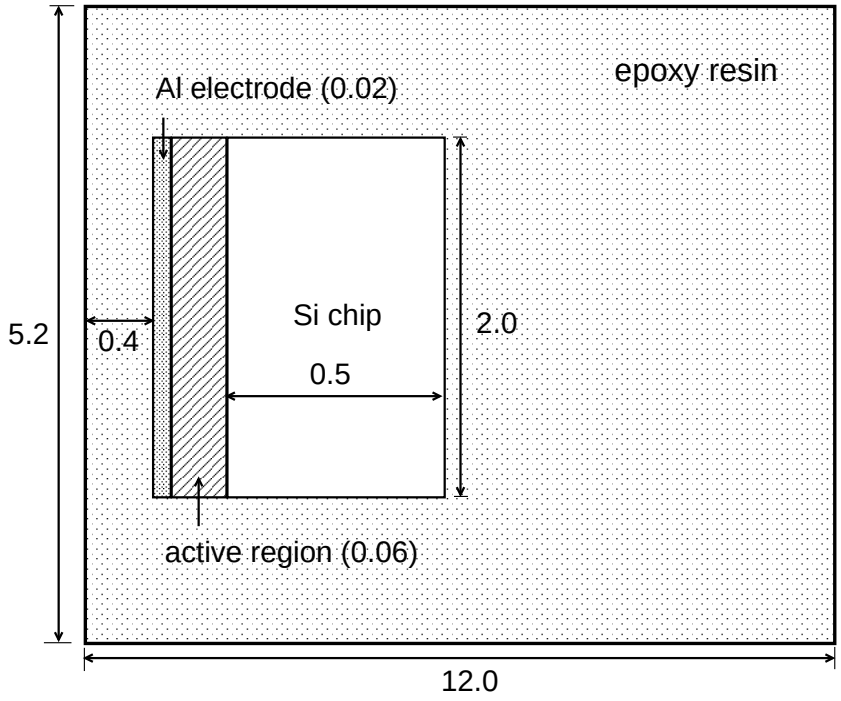

Figure B.1: Computational Model 1 of a Si electron detector (dimensions in mm). Density of each material: Al, 2.70 g/cm^3; Si, 2.33 g/cm^3; epoxy resin, 1.20 g/cm^3. The constituents of epoxy resin are 76% C, 15% O, and 9% H. From paper I.

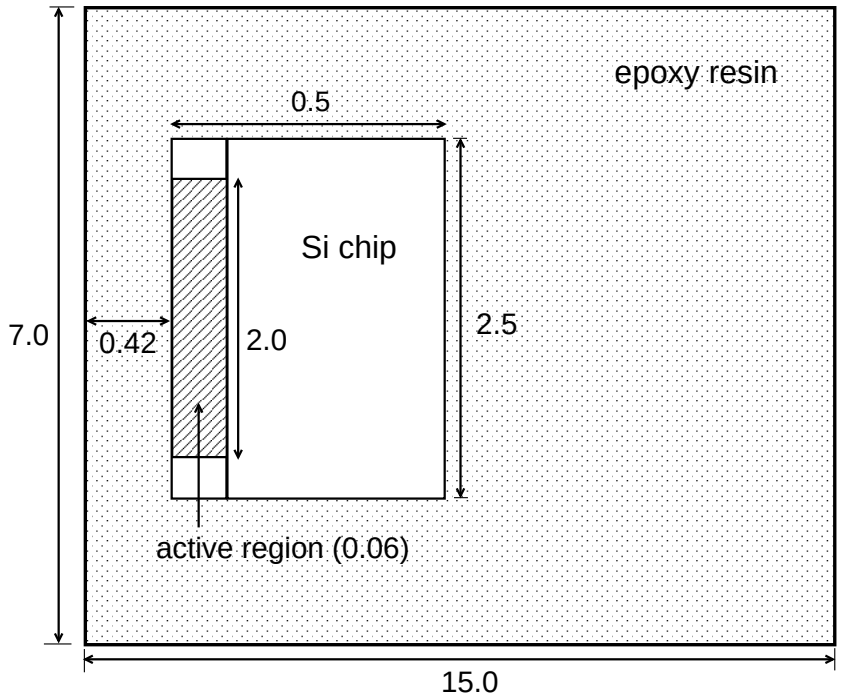

Figure B.2: Computational Model 2 of the Si electron detector with the same material densities as given in Figure B.1. From paper I.

B.2 Results and discussion

B.2.1 Diode response vs depth

The diode response is calculated as the water/silicon dose ratio for the full diode model. The calculated results for diode response versus depth for the 6 MeV and 18 MeV electron beams are shown in Figure B.3. It is seen that, up to a depth between d_{ref} and R_{50}, there is essentially no difference in the diode response between the two models. From R_{50} to R_p, there is a significant difference: the dose ratio for Model 2 is lower by 1% to 3%. The removal of the aluminum contact does not account for this discrepancy since when the cases with and without the 20 μm aluminum electrode are compared for the Model 2 diode, the two dose ratios at R_{50} agree within 0.2%. The thinner total Si chip thickness for Model 2 should increase the dose ratio at R_{50} by half a percent. The only possible cause of this 1-3% difference between the two models beyond R_{50} is the rim of Si material around active region in Model 2; it provides excess low-energy, side-scattered electrons into the active region thus lowering the water/silicon dose ratio. In summary, the depth-dose characteristics for the Model 2 diode are worse than those of Model 1: they vary by 4% from the surface to R_p. In reality, however, this 4% difference is hard to observe since the absolute dose level near R_p is very low.

Experimentally, there was a lot of work done to compare depth-dose curves for electron beams measured by Si diodes and by ionization chambers.[77,79–83,85] The diode used in the majority of these measurements is the one modeled in this work.

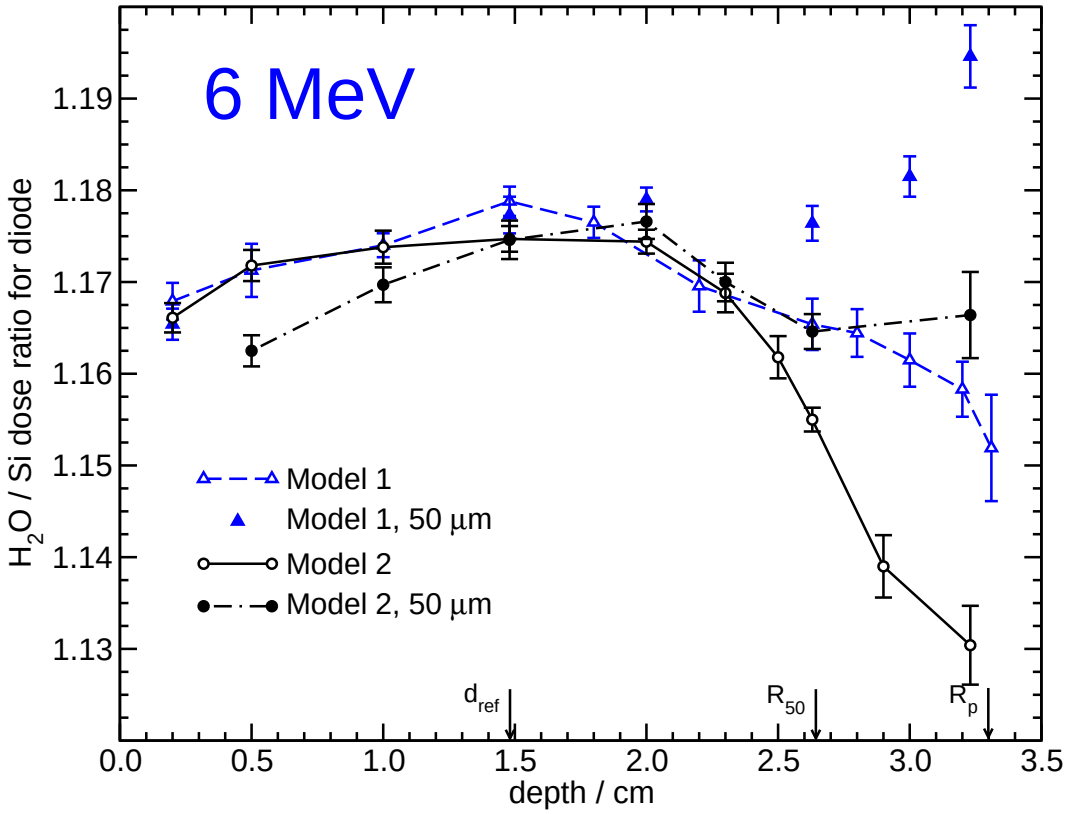

Figure B.3: Comparison of calculated water/silicon dose ratio vs depth for Model 1 (open triangle) and Model 2 (open circle) diodes and the corresponding diodes with the active region displaced 50 μm below the front face of the Si chip, i.e. with a dead layer of 50 μm (solid symbol). The calculation is done in a 6 MeV electron beam. From paper I.

B.2.2 Beam quality and field-size dependence of the diode response

Figure B.4 shows the calculated beam quality dependence of the response of both Model 1 and Model 2 diodes placed at d_{ref} in electron beams. The electron beam quality is specified by R_{50}. There is no significant difference between the two models. Although the variation of the response in the range of electron energies from 6 MeV to 18 MeV is about 1 to 1.5% for measurements at d_{ref}, the discrepancies may be slightly greater at d_{max} (see the differences in the broad beam results in Figure B.5) and overall it appears that the variation in response with energy is somewhat less than 2%.

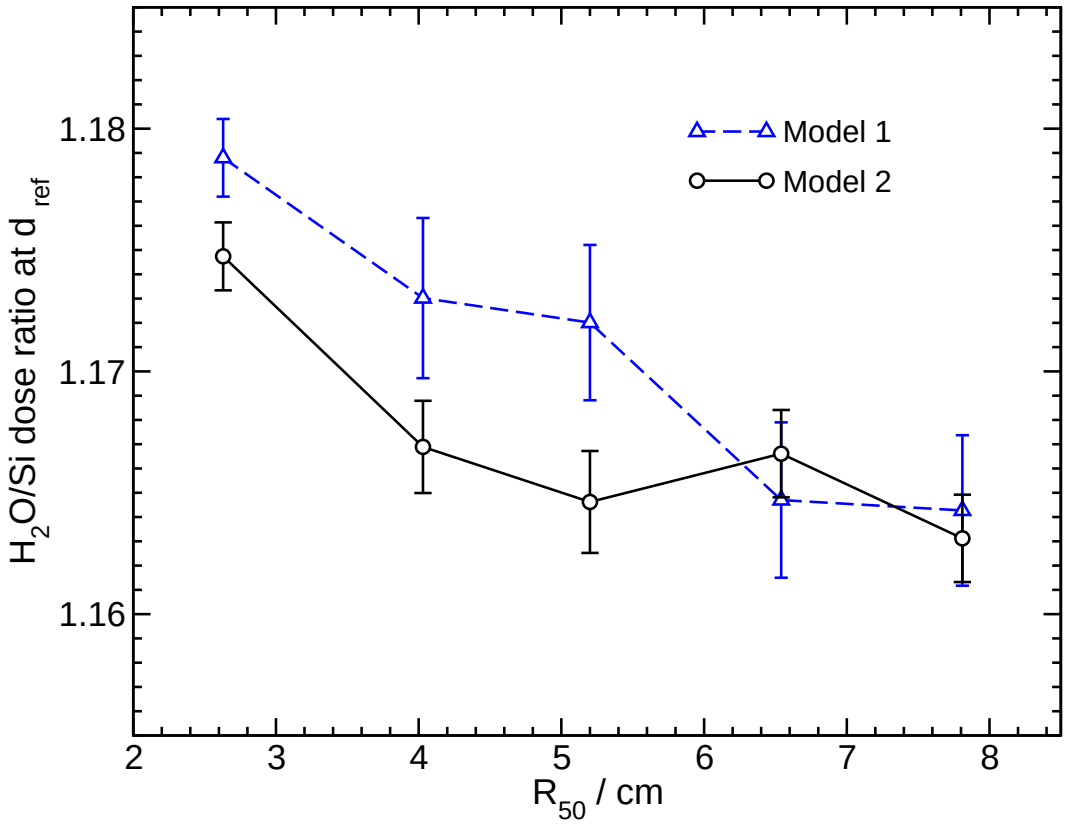

Figure B.4: Beam quality dependence of the diode's response (i.e. the dose ratio) for the two models. R_{50} is used as the beam quality specifier. The diode is placed at the reference depth d_{ref}. From paper I.

The field-size dependence of the response of the diode model (Model 1) is shown in Figure B.5. Here the field size is specified by the radius of the circularly shaped electron beam. The diode is located at the depth of maximum dose for each electron beam. For the field sizes normally used clinically (greater than 4×4 cm^2, or in an equivalent circular beam, radius greater than 2.2 cm), the response is almost constant within the calculation uncertainty of 0.2% in both 6 MeV and 18 MeV beams. When the field size is decreased to a radius of 0.6 cm, or 1×1 cm^2, the calculated dose ratio drops about 2% from that of the large field size in the 6 MeV beam and about 0.5% in the 18 MeV beam. For a Model 2 diode, only the response for an extreme case was calculated, i.e. 6 MeV beam of radius 0.5 cm; the results for the two models agree within 0.2%.

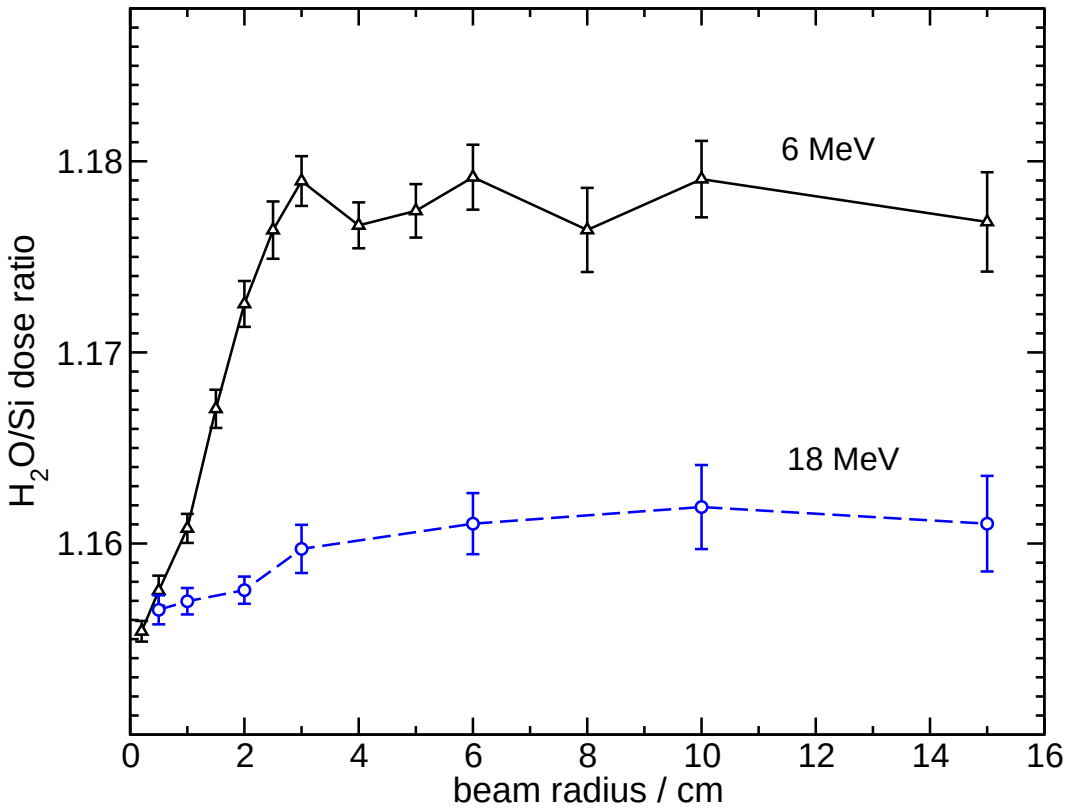

Figure B.5: Field-size dependence of the diode response in 6 MeV and 18 MeV electron beams for the full diode Model 1. The diode is placed at the respective d_{max} for each beam. From paper I.

B.3 Summary

Monte Carlo calculations of the dosimetric properties of a model of a Si diode detector in electron beams show that the diode response is nearly flat with respect to depth in a water phantom, with only 2% variation up to R_{50} and about 4% variation up to R_p, in a 6 MeV beam. The portion of Si crystal behind the active region of the diode detector is the most significant factor affecting the dosimetric properties of a Si diode detector. The energy independence or quality independence of the diode detector in electron beams is excellent, with less than 2% variation at d_{ref} for electron beam energies from 6 MeV to 18 MeV. The diode response is almost independent of the field size within the calculation uncertainty of 0.2% for routinely used clinical electron beams. It decreases by 2% for very small field sizes (1×1 cm^2) in low-energy (6 MeV) electron beams; and the variation is partly due to the intrinsic property of the active region of the Si diode.

References

[1] ICRU, Determination of absorbed dose in a patient irradiated by beams of x or gamma rays in radiotherapy procedures, ICRU Report 24, ICRU, Washington D.C., 1976.

[2] F. H. Attix, *Introduction to Radiological Physics and Radiation Dosimetry*, Wiley, New York, 1986.

[3] L. H. Gray, An ionization method for the absolute measurement of γ-ray energy, Proc. Roy. Soc. **A156**, 578 – 596 (1936).

[4] L. V. Spencer and F. H. Attix, A theory of cavity ionization, Radiat. Res. **3**, 239 – 254 (1955).

[5] IAEA, *The Use of Plane Parallel Ionization Chambers in High Energy Electron and Photon Beams: An International Code of Practice for Dosimetry*, volume 381 of *Technical Report Series*, IAEA, Vienna, 1997.

[6] M. Boutillon and A. M. Perroche-Roux, Re-evaluation of the W value for electrons in dry air, Phys. Med. Biol. **32**, 213 – 219 (1987).

[7] AAPM TG–21, A protocol for the determination of absorbed dose from high-energy photon and electron beams, Med. Phys. **10**, 741 – 771 (1983).

[8] IAEA, *Absorbed Dose Determination in Photon and Electron Beams; An International Code of Practice*, volume 277 of *Technical Report Series*, IAEA, Vienna, 1987.

[9] D. W. O. Rogers and C. K. Ross, The Role of Humidity and Other Correction Factors in the AAPM TG–21 Dosimetry Protocol, Med. Phys. **15**, 40 – 48 (1988).

[10] P. R. Almond, P. J. Biggs, B. M. Coursey, W. F. Hanson, M. S. Huq, R. Nath, and D. W. O. Rogers, AAPM's TG–51 Protocol for Clinical Reference Dosimetry of High-Energy Photon and Electron Beams, Med. Phys. **26**, 1847 – 1870 (1999).

[11] IAEA, *Absorbed Dose Determination in External Beam Radiotherapy: An International Code of Practice for Dosimetry Based on Standards of Absorbed Dose to Water*, volume 398 of *Technical Report Series*, IAEA, Vienna, 2001.

[12] P. R. Almond, F. H. Attix, S. Goetsch, L. J. Humphries, H. Kubo, R. Nath, and D. W. O. Rogers, The calibration and use of plane-parallel ionization chambers for dosimetry of electron beams: An extension of the 1983 AAPM protocol, Report of AAPM Radiation Therapy Committee Task Group 39, Med. Phys. **21**, 1251 – 1260 (1994).

[13] K. A. Johansson, L. O. Mattsson, L. Lindborg, and H. Svensson, Absorbed-dose determination with ionization chambers in electron and photon beams having energies between 1 and 50 MeV, in *IAEA Symposium Proceedings*, pages 243 – 270, IAEA–SM–222/35, IAEA, Vienna, 1977.

[14] D. W. O. Rogers, Fundamentals of Dosimetry Based on Absorbed-Dose Standards, in *Teletherapy Physics, Present and Future*, edited by J. R. Palta and T. R. Mackie, pages 319 – 356, AAPM, Washington DC, 1996.

[15] J. R. Cunningham and M. R. Sontag, Displacement Corrections Used in Absorbed Dose Determinations, Med. Phys. **7**, 672 – 676 (1980).

[16] I. Kawrakow and D. W. O. Rogers, The EGSnrc Code System: Monte Carlo simulation of electron and photon transport, Technical Report PIRS–701, National Research Council of Canada, Ottawa, Canada , (2000).
(see http://www.irs.inms.nrc.ca/inms/irs/EGSnrc/EGSnrc.html).

[17] R. L. Ford and W. R. Nelson, The EGS code system – Version 3, Report SLAC–210, Stanford Linear Accelerator Center, Stanford, California, 1978.

[18] W. R. Nelson, H. Hirayama, and D. W. O. Rogers, The EGS4 code system, Report SLAC–265, Stanford Linear Accelerator Center, Stanford, California, 1985.

[19] I. Kawrakow, Accurate condensed history Monte Carlo simulation of electron transport. I. EGSnrc, the new EGS4 version, Med. Phys. **27**, 485 – 498 (2000).

[20] I. Kawrakow, Accurate condensed history Monte Carlo simulation of electron transport. II. Application to ion chamber response simulations, Med. Phys. **27**, 499 – 513 (2000).

[21] D. W. O. Rogers, I. Kawrakow, J. P. Seuntjens, B. R. B. Walters, and E. Mainegra-Hing, NRC User Codes for EGSnrc, Technical Report PIRS–702(RevB), National Research Council of Canada, Ottawa, Canada, 2003.

[22] D. W. O. Rogers, B. A. Faddegon, G. X. Ding, C.-M. Ma, J. Wei, and T. R. Mackie, BEAM: A Monte Carlo code to simulate radiotherapy treatment units, Med. Phys. **22**, 503 – 524 (1995).

[23] D. W. O. Rogers, B. Walters, and I. Kawrakow, BEAMnrc Users Manual, NRC Report PIRS 509(a)revH (2004).

[24] I. Kawrakow, EGSnrc C++ class library, Technical Report PIRS–898, National Research Council of Canada, Ottawa, Canada. http://www.irs.inms.nrc.ca/EGSnrc/pirs898/, 2005.

[25] I. Kawrakow, egspp: the EGSnrc C++ class library, Technical Report PIRS–899, National Research Council of Canada, Ottawa, Canada, 2005.

[26] L. A. Buckley, I. Kawrakow, and D. W. O. Rogers, CSnrc: correlated sampling Monte Carlo calculations using EGSnrc, Med. Phys. **31**, 3425 – 3435 (2004).

[27] L. A. Buckley and D. W. O. Rogers, Wall correction factors, P_{wall}, for thimble ionization chambers, Med. Phys. **33**, 455 – 464 (2006).

[28] L. A. Buckley and D. W. O. Rogers, Wall correction factors, P_{wall}, for parallel-plate ionization chambers, Med. Phys. **33**, 1788 – 1796 (2006).

[29] P. N. Mobit, A. E. Nahum, and P. Mayles, The energy correction factor of LiF thermoluminescent dosemeters in megavoltage electron beams: Monte Carlo simulations and experiments, Phys. Med. Biol. **41**, 979 – 993 (1996).

[30] P. N. Mobit, P. Mayles, and A. E. Nahum, The quality dependence of LiF TLD in megavoltage photon beams: Monte Carlo simulation and experiments, Phys. Med. Biol. **41**, 387 – 398 (1996).

[31] A. F. Bielajew and D. W. O. Rogers, PRESTA: The Parameter Reduced Electron-Step Transport Algorithm for electron Monte Carlo transport, Nucl. Inst. Meth. B **18**, 165 – 181 (1987).

[32] A. E. Nahum, Perturbation effects in dosimetry: Part I. Kilovoltage x-rays and electrons, Phys. Med. Biol. **41**, 1531 – 1580 (1996).

[33] C.-M. Ma and A. E. Nahum, Plane-parallel chambers in electron beams: Monte Carlo findings on perturbation correction factor, In "Proceedings of the IAEA International Symposium on measurement assurance in dosimetry" (Vienna: IAEA) , 481 – 493 (1994).

[34] F. Verhaegen, R. Zakikhani, A. DuSautoy, H. Palmans, G. Bostock, D. Shipley, and J. Seuntjens, Perturbation correction factors for the NACP-02 plane-parallel ionization chamber in water in high-energy electron beams, Phys. Med. Biol. **51**, 1221 – 1235 (2006).

[35] K. Zink and J. Wulff, Monte Carlo calculations of beam quality correction factors k_Q for electron dosimetry with a parallel-plate Roos chamber, Phys. Med. Biol. **53**, 1595 – 1607 (2008).

[36] J. Wulff, J. T. Heverhagen, and K. Zink, Monte-Carlo-based perturbation and beam quality correction factors for thimble ionization chambers in high-energy photon beams, Phys. Med. Biol. **53**, 2823 – 2836 (2008).

[37] F. Araki, Monte Carlo calculations of correction factors for plane-parallel ionization chambers in clinical electron dosimetry, Med. Phys. **35**, 4033 – 4040 (2008).

[38] G. Mora, A. Maio, and D. W. O. Rogers, Monte Carlo simulation of a typical ^{60}Co therapy source, Med. Phys. **26**, 2494 – 2502 (1999).

[39] D. Sheikh-Bagheri and D. W. O. Rogers, Monte Carlo calculation of nine megavoltage photon beam spectra using the BEAM code, Med. Phys. **29**, 391 – 402 (2002).

[40] G. X. Ding and D. W. O. Rogers, Energy spectra, angular spread, and dose distributions of electron beams from various accelerators used in radiotherapy, NRC Report PIRS–0439, NRC, Ottawa, K1A 0R6, 1995.

[41] C.-M. Ma and A. E. Nahum, Calculations of ion chamber displacement effect corrections for medium-energy x-ray dosimetry, Phys. Med. Biol. **40**, 45 – 62 (1995).

[42] D. W. O. Rogers and I. Kawrakow, Monte Carlo calculated correction factors for primary standards of air-kerma, Med. Phys. **30**, 521 – 543 (2003).

[43] M. Boutillon, Perturbation correction for the ionometric determination of absorbed dose in a graphite phantom for ^{60}Co gamma rays, Phys. Med. Biol. **28**, 375 – 388 (1983).

[44] M. T. Niatel, A. M. Perroche-Roux, and M. Boutillon, Two determinations of W for electrons in dry air, Phys. Med. Biol. **30**, 67 – 75 (1985).

[45] I. Kawrakow and D. W. O. Rogers, The EGSnrc Code System: Monte Carlo simulation of electron and photon transport, Technical Report PIRS–701, National Research Council of Canada, Ottawa, Canada, 2000.

[46] C.-M. Ma, C. W. Coffey, L. A. DeWerd, R. Nath, C. Liu, S. M. Seltzer, and J. Seuntjens, AAPM protocol for 40 – 300 kV x-ray beam dosimetry in radiotherapy and radiobiology, Med. Phys. **28**, 868 – 893 (2001).

[47] H. Kubo, L. J. Kent, and G. Krithivas, Determination of N_{gas} and P_{repl} factors from commercially available parallel-plate chambers, Med. Phys. **13**, 908 – 912 (1986).

[48] F. W. Wittkämper, H. Thierens, A. Van der Plaetsen, C. de Wagter, and B. J. Mijnheer, Perturbation correction factors for some ionization chambers commonly applied in electron beams, Phys. Med. Biol. **36**, 1639 – 1652 (1991).

[49] F. T. Kuchnir and C. S. Reft, Experimental values for $P_{\mathrm{wall,x}}$ and $P_{\mathrm{repl,E}}$ for five parallel-plate, ion chambers- A new analysis of previously published data, Med. Phys. **19**, 367 – (1992).

[50] A. Van der Plaetsen, J. Seuntjens, H. Thierens, and S. Vynckier, Verification of absorbed doses determined with thimble and parallel-plate ionization chambers in clinical electron beams using ferrous sulphate dosimetry, Med. Phys. **21**, 37 – 44 (1994).

[51] G. X. Ding and J. Cygler, Measurement of $\mathrm{P_{repl}}$ $\mathrm{P_{wall}}$ factors in electron beams and in a ^{60}Co beam for plane-parallel chambers, Med. Phys. **25**, 1453 – 1457 (1998).

[52] C. S. Reft and F. T. Kuchnir, Measured overall perturbation factors at depths greater than $d_{\max}$ for ionization chambers in electron beams, Med. Phys. **26**, 208 – 213 (1999).

[53] L. Büermann, B. Grosswendt, H.-M. Kramer, H.-J. Selbach, M. Gerlach, M. Hoffmann, and M. Krumrey, Measurement of the x-ray mass energy-absorption coefficient of air using 3 keV to 10 keV synchrotron radiation, Phys. Med. Biol. **51**, 5125 – 5150 (2006).

[54] ICRU, Stopping powers for electrons and positrons, ICRU Report 37, ICRU, Bethesda, MD., 1984.

[55] M. Boutillon, Revision of the results of international comparisons of absorbed dose in graphite in a ^{60}Co beam, BIPM Report BIPM–90/4 (1990).

[56] M. Boutillon and A.-M. Perroche-Roux, Radial non-uniformity of the BIPM ^{60}Co beam, BIPM Report BIPM–89/2 , 9 pages (1989).

[57] M. Boutillon, Gap correction for the calorimetric measurement of absorbed dose in graphite with a ^{60}Co beam, Phys. Med. Biol. **34**, 1809 – 1821 (1989).

[58] H. Bichsel and T. Hiraoka, Energy loss of 70 MeV protons in elements, Nucl. Inst. Meth. **B66**, 345 – 351 (1992).

[59] I. H. Ferreira, A. Bridier, C. E. de Almeida, D. Marre, and J. Chavaudra, Perturbation corrections for flat and thimble-type cylindrical standard ionization chambers for ^{60}Co gamma rays: Monte Carlo calculations, Phys. Med. Biol. **43**, 2721 – 2727 (1998).

[60] M. T. Niatel, On the location of a flat ionization chamber for absorbed dose determination, Phys. Med. Biol. **28**, 407 – 410 (1983).

[61] A. F. Bielajew and D. W. O. Rogers, Implications of new correction factors on primary air kerma standards in ^{60}Co beams, Phys. Med. Biol. **37**, 1283 – 1291 (1992).

[62] D. T. Burns, A new approach to the determination of air kerma using primary-standard cavity ionization chambers, Phys. Med. Biol. **51**, 929 – 942 (2006).

[63] D. T. Burns, P. J. Allisy, and C. Kessler, Re-evaluation of the BIPM international standard for air kerma in ^{60}Co gamma radiation, Metrologia **44**, L53 – L56 (2007).

[64] D. W. O. Rogers, How accurately can EGS4/PRESTA calculate ion chamber response?, Med. Phys. **20**, 319 – 323 (1993).

[65] L. Büermann, E. Gargioni, G. Hilgers, and A. Krauss, Comparison of ionometric and calorimetric determination of absorbed dose to water for cobalt-60 gamma rays, Proceed. of Absorbed Dose and Air Kerma Primary Standards Workshop, LNHB, Paris , http://www.nucleide.org/ADAKPS_WS/Session H – IC Absorbed Dose/H3_Or–Buermann.pdf (May, 2007).

[66] L. Büermann and G. Hilgers, Significant discrepancies in air kerma rates measured with free-air and cavity ionization chambers, Nucl. Inst. Meth. A **580**, 477 – 480 (2007).

[67] M. S. Huq, N. Yue, and N. Suntharalingam, Experimental determination of fluence correction factors at depths beyond $d_{\max}$ for a Farmer type cylindrical ionization chamber in clinical electron beams, Med. Phys. **24**, 1609 – 1613 (1997).

[68] P. Andreo, L. Linborg, and J. Medin, On the calibration of plane-parallel ionisation chambers using ^{60}Co beams, Med. Phys. **18**, 326 – 327 (1991).

[69] J. Halbleib, Structure and Operation of the ITS code system, in *Monte Carlo Transport of Electrons and Photons*, edited by T. M. Jenkins, W. R. Nelson,

A. Rindi, A. E. Nahum, and D. W. O. Rogers, pages 249 – 262, Plenum Press, New York, 1988.

[70] A. E. Nahum, Perturbation Effects in Dosimetry, Technical Report ICR-PHYS-1/94, Joint Dept of Physics, The Royal Marsden Hospital, Sutton, Surrey, SM2 5PT, UK, 1994.

[71] N. I. Kalach and D. W. O. Rogers, Which accelerator photon beams are "clinic-like" for reference dosimetry purposes?, Med. Phys. **30**, 1546 – 1555 (2003).

[72] E. Chin, D. Shipley, M. Bailey, J. Seuntjens, H. Palmans, A. DuSautoy, and F. Verhaegen, Validation of a Monte Carlo model of a NACP-02 plane-parallel ionization chamber model using electron backscatter experiments, Phys. Med. Biol. **53**, N119 – N126 (2008).

[73] I. Kawrakow, On the effective point of measurement in megavoltage photon beams, Med. Phys. **33**, 1829 – 1839 (2006).

[74] L. S. Skaggs, Depth dose of electrons from the betatron, Radiology **53**, 868 – 873 (1949).

[75] AAPM Task Group 62, Diode in-vivo dosimetry for patients recieving external beam radiation therapy, Report 87, AAPM, Washington, DC, 2005.

[76] G. Leunens, J. V. Dam, A. Dutreix, and E. van der Schueren, Quality assurance in radiotherapy by in vivo dosimetry. 1. Entrance dose measurements, a reliable procedure, Radiother. Oncol. **17**, 141 – 151 (1990).

[77] M. A. Trump and A. P. Pinkerton, Application of PN Junction Diodes to the Measurement of Dose Distribution of High Energy Radiation, Phys. Med. Biol. **12**, 573 – 576 (1967).

[78] L. D. Gager, A. E. Wright, and P. R. Almond, Silicon diode detectors used in radiological physics measurements. Part I: Development of an energy compensating shield, Med. Phys. **4**, 494 – 498 (1977).

[79] G. Rikner, Characteristics of a p-Si detector in high energy electron fields, Acta Rad. Oncol. **24**, 71 – 74 (1985).

[80] K. R. Shortt, C. K. Ross, A. F. Bielajew, and D. W. O. Rogers, Electron Beam Dose Distributions Near Standard Inhomogeneities, Phys. Med. Biol. **31**, 235 – 249 (1986).

[81] R. K. Ten Haken, B. A. Fraass, and R. J. Jost, Practical methods of electron depth-dose measurement compared to use of the NACP design chamber in water, Med. Phys. **14**, 1060 – 1066 (1987).

[82] P. Bjork, T. Knoos, and P. Nilsson, Comparative dosimetry of diode and diamond detectors in electron beams for intraoperative radiation therapy, Med. Phys. **27**, 2580 – 2588 (2000).

[83] G. X. Ding and C. W. Yu, Determination of percentage depth-dose curves for electron beams using different types of detectors, Med. Phys. **28**, 298 – 302 (2001).

[84] M. Bucciolini, F. B. Buonamici, S. Mazzocchi, C. Angelis, S. Onori, and G. A. P. Cirrone, Diamond detector versus silicon diode and ion chamber in photon beams of different energy and field size, Med. Phys. **30**, 2149 – 2154 (2003).

[85] I. Griessbach, M. Lapp, J. Bohsung, G. Gademann, and D. Harder, Dosimetric characteristics of a new unshielded silicon diode and its application in clinical photon and electron beams, Med. Phys. **32**, 3750 – 3754 (2005).

[86] G. Rikner and E. Grusell, Selective shielding of a p-type detector for quality independence, Acta Radiol. Oncol. **24**, 65 (1985).

[87] G. F. Knoll, *Radiation Detection and Measurement*, Wiley, New York, 1989.